OBSERVATION AND PROCESSING OF

2.3 GHz RADIO ASTRONOMY SURVEY DATA

Thesis

Submitted in Fulfilment of the

Requirement for the Degree of

MASTER OF SCIENCE

of Rhodes University

by

JUSTIN LEONARD JONAS

December 1982

ACKNOWLEDGEMENTS
==========

I am grateful to many people for their guidance and assistance during the course of my work.

I should like to thank my supervisors, Prof. E. E. Baart and Prof. G. de Jager, for their useful criticism and continual encouragement.

I am grateful to my friends and colleagues in the University, especially Pete Mountfort, for their suggestions and help.

Special thanks must go to Dr. G. Nicolson, Director of the Radio Astronomy Observatory, for the use of the observatory facilities and his interest in my work.

I am indebted to Rhodes University for their financial assistance in 1980, and the Department of Physics and Electronics for the use of the word-processor used to produce this thesis.

Finally, I should like to thank my parents for their unfailing support and encouragement.

Justin Jonas

Table of Contents

Abstract

The results of the second part of the Rhodes University Southern Sky Survey at 2.3GHz are presented. The area surveyed extends from 12h00 to 22h00 right ascension between declinations -63^{o} and -24^{o}. The observation technique and data reduction processes are analyzed. Digital data processing techniques used to enhance and display the data are dicussed.

The results show that the Galactic emission extends as far as 40^{o} latitude. Filamentary and loop-like structures are found superimposed on this general emission. Many of these features are unidentified as yet. A large region of emission is found to coincide with the Sco-Cen stellar association. A lower limit for the ionizing flux from the stars in the association is derived.

All of the non-confused extragalactic sources with flux densities greater than 0.5Jy are listed. The flux densities of these sources have been measured and any possible extended features are noted.

CHAPTER 1 INTRODUCTION

Most of the first radio astronomy observations involved the mapping of the intensity of the large scale celestial radio emission. The relatively insensitive receivers and poor resolution available to the first astronomers allowed them to make large scale maps of the radio brightness distribution, but little detailed structure was evident in the data. With the rapid growth of interest in this field there was a corresponding improvement in the observing apparatus. The construction of large dish antennae with higher resolution and the development of sensitive receivers allowed more detailed maps to be produced. Radio maps with resolutions better than optical photographs are now possible with the advent of the various interferometric techniques.

Unfortunately this rapid trend towards higher resolution has meant that smaller and smaller areas of sky are being mapped. High resolution techniques are not suited to mapping large areas because the mapping would take too long. There is a great need for intermediate resolution maps of the entire sky in order to detect large scale radio emission features. These features are not detected when observing a small field because they are subtracted out as baselines. The radio brightness distribution of distant galaxies has been mapped using high resolution techniques, but few complete surveys of our galaxy exist. Recent sky surveys (Haslam et al 1982, Landecker and Wielebinski 1970, Nicolson 1965) have shown that the emission from our galaxy is very complex and worthy of investigation. The morphology of the Milky Way may be studied using these data, especially the nature of local features which have large angular extent. As an example, Haslam et al (1971) have shown large loop-like radio features in 408MHz sky survey data.

Large scale surveys do not only show up the structure of the emission from our own galaxy. Nearby extra-galactic objects such as the Magellanic Clouds require a large scale mapping technique to be observed effectively. The area observed must be larger than the optical size of the object so that the true extent of the radio emission may be determined.

Large area mapping places severe requirements on the observation equipment and method. The antenna must be manoeuverable in order to allow fast scans to be made. The receiver must have a stable baseline and low noise temperature. Sophisticated data processing is necessary in order to reduce and enhance the data.

The Rhodes astronomy group realized that the facilities of the Radio Astronomy Observatory (R.A.O.) at Hartebeesthoek met the requirements for survey work. The observatory is run by the National Institute for Telecommunications Research (N.I.T.R.) of the South African Council for Scientific and Industrial Research (C.S.I.R.). The 26m dish antenna used to be part of the N.A.S.A. deep space satellite tracking network, but is now used exclusively for radio astronomy. The observatory operates a 2.3GHz receiver which has properties which make it very suitable for large area mapping. No previous large scale surveys have been performed at this frequency. There are relatively few radio telescopes in the southern hemisphere. This meant that there was plenty of pioneering work to be done in surveying the southern sky at 2.3GHz.

Initial survey work was performed by driving the telescope manually and recording the radiometer output on paper tape. A mini-computer was used to reduce this data and the results were transmitted to a larger computer in order to obtain contour maps of the brightness distribution. The availability of an on line computer at the observatory and improved

computing ability at the university have resulted in the automation and improvement of the observing and data processing techniques. Mountfort (1981) developed the present automated observing technique and data reduction process. He used this new technique to survey a region of sky which contained the Magellanic Clouds. This thesis presents an analysis of this method and describes digital image processing software which has been developed to improve the raw data. The results of the second part of the 2.3GHz survey are presented, using the digital image processing to enhance the data.

Chapter 2 of this thesis describes the observing method and data reduction techniques developed by Mountfort (1981). In order to display and analyse the data effectively some form of signal conditioning must be applied to the raw data produced by the reduction process. Before this signal processing can be done it is necessary to understand the effects the observing technique and data reduction have on the observed data. The analysis in chapter 4 describes how the raw radio brightness data are related to the actual radio brighness distribution in the sky, using the mathematical theory described in chapter 3. Knowing the properties of the raw data it is possible to enhance this data using digital signal processing techniques. This enhanced data is suitable for display and analysis. The processing and display techniques developed are described in chapter 5.

Chapter 6 describes the observation of the second part of the Rhodes all sky survey at 2.3GHz. The results of the observation are presented in the form of contour maps and grey-scale images. The following two chapters describe preliminary analysis performed on these data. The results of these analyses show the importance of medium resolution, large scale surveys in the understanding of our galaxy and its neighbours.

CHAPTER 2 THE TELESCOPE AND OBSERVING METHOD

This chapter discusses the apparatus and experimental method used to produce the radio brightness distribution maps of the Rhodes University Southern Sky Survey. Since the apparatus has been developed and described by the Radio Astronomy Observatory (R.A.O) staff, it is discussed only briefly. Similarly the observing software and technique were developed by a previous Rhodes student (Mountfort 1981) and are only included for completeness.

A simplified diagram of the main components used for these observations is shown in figure 2.1. In addition to the equipment in the figure the observatory also has an auto-correlation spectral line receiver, a V.L.B.I. terminal and radiometers for other frequencies. These are not relevant to the mapping observations described.

Section 2.1 discusses the physical antenna and the system implemented to control it. This is followed by a description of the receiver used for the observations. The observing technique is introduced in section 2.3, followed by a section on programs written at the observatory for looking at semi-processed data. Section 2.5 gives a brief explanation of the initial processing of the data and the construction of a raw map.

2.1 The Antenna and its control

The antenna at the Hartebeesthoek Radio Astronomy Observatory is a 26m parabolic Cassegrain reflector on an equatorial mount, which is convenient for radio astronomy since the two axes represent right ascension and declination. The half-power beamwidth at 2.3 GHz is 20' of arc, which makes it very suitable for mapping large areas of sky. A scan spacing of 0.1 degrees is sufficient to ensure that the observed brightness distribution is over-sampled, thus enabling the resulting data to be filtered by Fourier

Figure 2.1

The hardware configuration used for the observations.

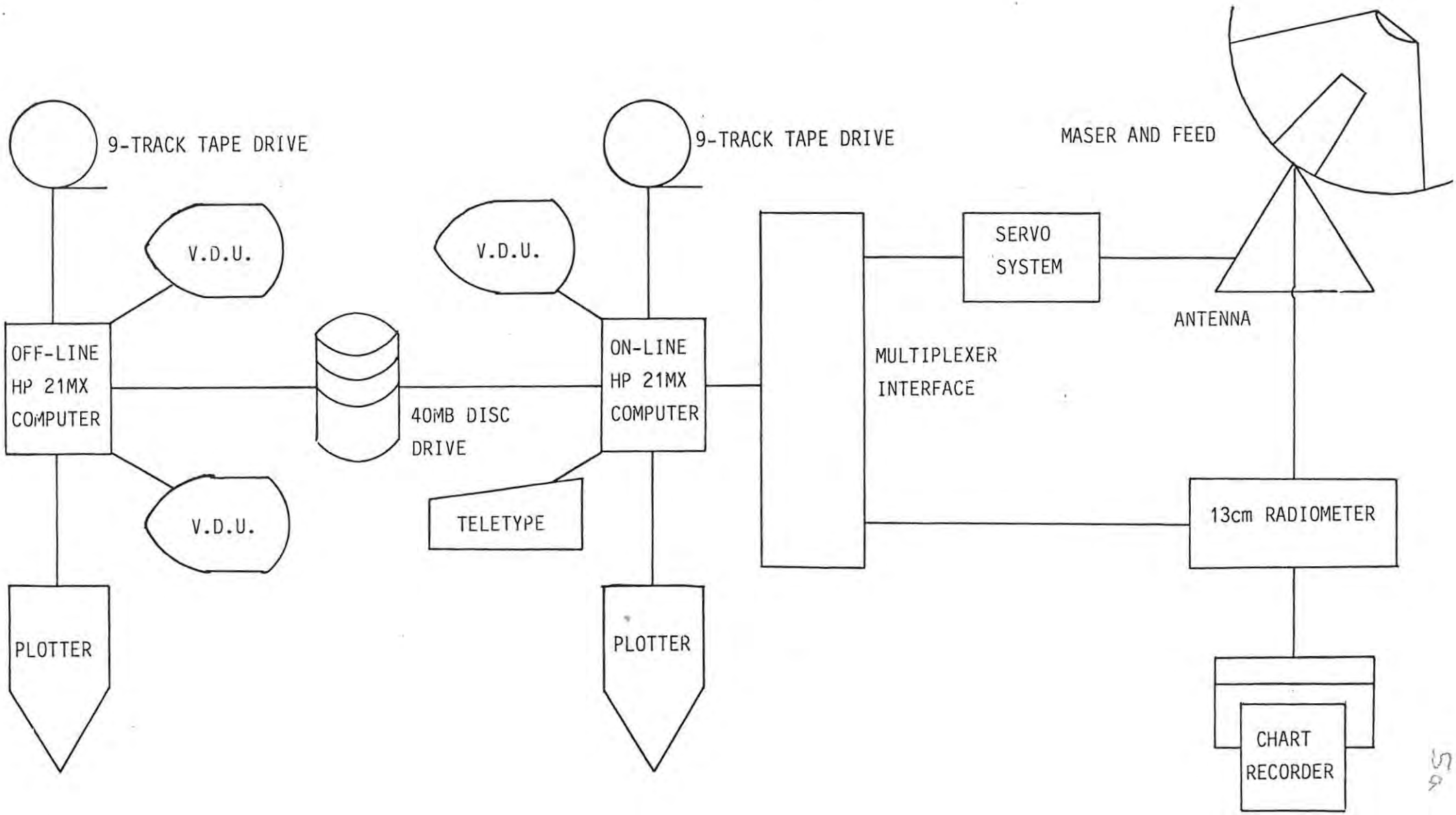
9-TRACK TAPE DRIVE
V.D.U.
OFF-LINE
HP 21MX
COMPUTER
V.D.U.
PLOTTER
40MB DISC
DRIVE
9-TRACK TAPE DRIVE
V.D.U.
ON-LINE
HP 21MX
COMPUTER
TELETYPE
PLOTTER
MULTIPLEXER
INTERFACE
SERVO
SYSTEM
MASER AND FEED
ANTENNA
13cm RADIOMETER
CHART
RECORDER

methods to improve the signal to noise ratio without degrading the resolution of the data. Using this scan spacing large areas may be mapped within reasonable periods of time. The small physical size of the antenna and its powerful servo system allow it to be very manoeuverable, and it may be driven at high speeds (0.5 deg/s in declination), thus enabling large areas of sky to be scanned quickly.

In order to automate the control of the antenna, the R.A.O. staff constructed a multiplexer interface which allows the servo systems to interface to a Hewlett-Packard 21MX minicomputer installed at the observatory. The multiplexer also allows the computer to communicate with the radiometers. This computer runs under the R.T.E. II operating system (Real Time Executive two), which supports multitasking for real-time applications. Assembly language drivers were written for the interface (Mountfort 1981) and incorporated into the operating system using the System Generation package. In order to facilitate communications between observing programs and these drivers, and simplify observing program implementation, R.T.E. Fortran-IV programs were developed which handle the low level driving of the telescope.

The two main programs involved in the telescope driving are STEER and COMND. STEER is a program which calculates the command error for each axis and updates the error voltage to the respective servos every 100 ms, and is thus part of the feedback loop. Since this program is active most of the time it remains in the physical core memory of the computer during an observation, i.e. it is memory resident. COMND is the program with which observing programs communicate. The observing program passes messages which define the trajectory of the telescope between two given command times to COMND. R.T.E. structures are used to pass these messages. For example a message might specify that the telescope is to move to a given hour-angle and

declination immediately and remain there indefinitely. COMND interpolates the position of each axis for times between the two command times. This interpolation takes pointing corrections and precession into account, if required. The parameters of these interpolation functions are passed on to STEER, from which it calculates command co-ordinates every 100 ms. COMND is only active for a short while when the observing program instructs it to change the motion of the telescope, and thus need not be permanently resident in core. It is only read from the disc into core memory when it is needed by an observing program, i.e. it is disc resident, and is removed on completion, leaving room in main memory for user programs. In order to ensure safe operation of the telescope STEER has a number of built in safety features. It compares the co-ordinates of the antenna against a limit map so that the telescope may not be driven to its physical limits, thus reducing the chance of structural damage. STEER also performs consistency checks on the servo systems. For example, if the antenna position encoders indicate a change in position with time, it checks whether the tachometers produce a signal showing movement.

A small memory resident program called MONI communicates with the driving programs to update a display on the video terminal, giving the desired antennna coordinates, the actual coordinates and the difference between these two.

2.2 The Maser and Radiometer

The 2.3 GHz front end receiver at Hartebeesthoek is a travelling-wave ruby maser, cryogenically cooled to 4.5K, the boiling point of liquid helium. Two inherent properties of the maser make it suitable for large area mapping, a low stable noise temperature and good gain stability. The low noise allows shorter integration periods to achieve a given signal to noise ratio, which

leads to a reduction in the observation time. The stable noise temperature and gain are required so that no unwanted variation in the radiometer output occurs during the night's observation. These long term stability factors are important because any slow unwanted variation would show up as a large-scale feature on the resulting map.

The radiometer used compensates for gain and bandwidth changes in the maser. Figure 2.2 is a block diagram of the gain-stabilized, noise-adding radiometer, and a short description of its operation follows (Nicolson 1970). Noise, modulated by a switching signal, is injected into the maser input via a directional coupler in the maser feed. A synchronous detector at the square-law detector output monitors the amplitude of the modulation after amplification and is thus a measure of the gain of the system. This amplitude is compared to a constant reference and the difference is used as an automatic gain control (A.G.C.) signal to the I.F. amplifier. This stabilizes the gain of the system and thus ensures that the absolute calibration of the receiver does not change with time, i.e. the flux density of radio sources may be measured accurately. Since the open loop gain of the system is finite, the closed loop gain will not be exactly constant. Variations in the closed loop gain will cause spurious changes in the output of the square law detector, because of the apparent change in the power of the noise diode signal. In order to remove this effect a fraction of the synchronous detector voltage is balanced against the square law detector output signal, the fraction being adjusted so that the radiometer output is zero with the antenna pointing towards 'cold' sky. The radiometer output is independent of variations in system gain and bandwidth, but will be proportional to a change in the noise temperature, due to a radio source for instance. T_e ,the system temperature referred to the maser input, is

Figure 2.2

Schematic diagram of the noise adding radiometer system.

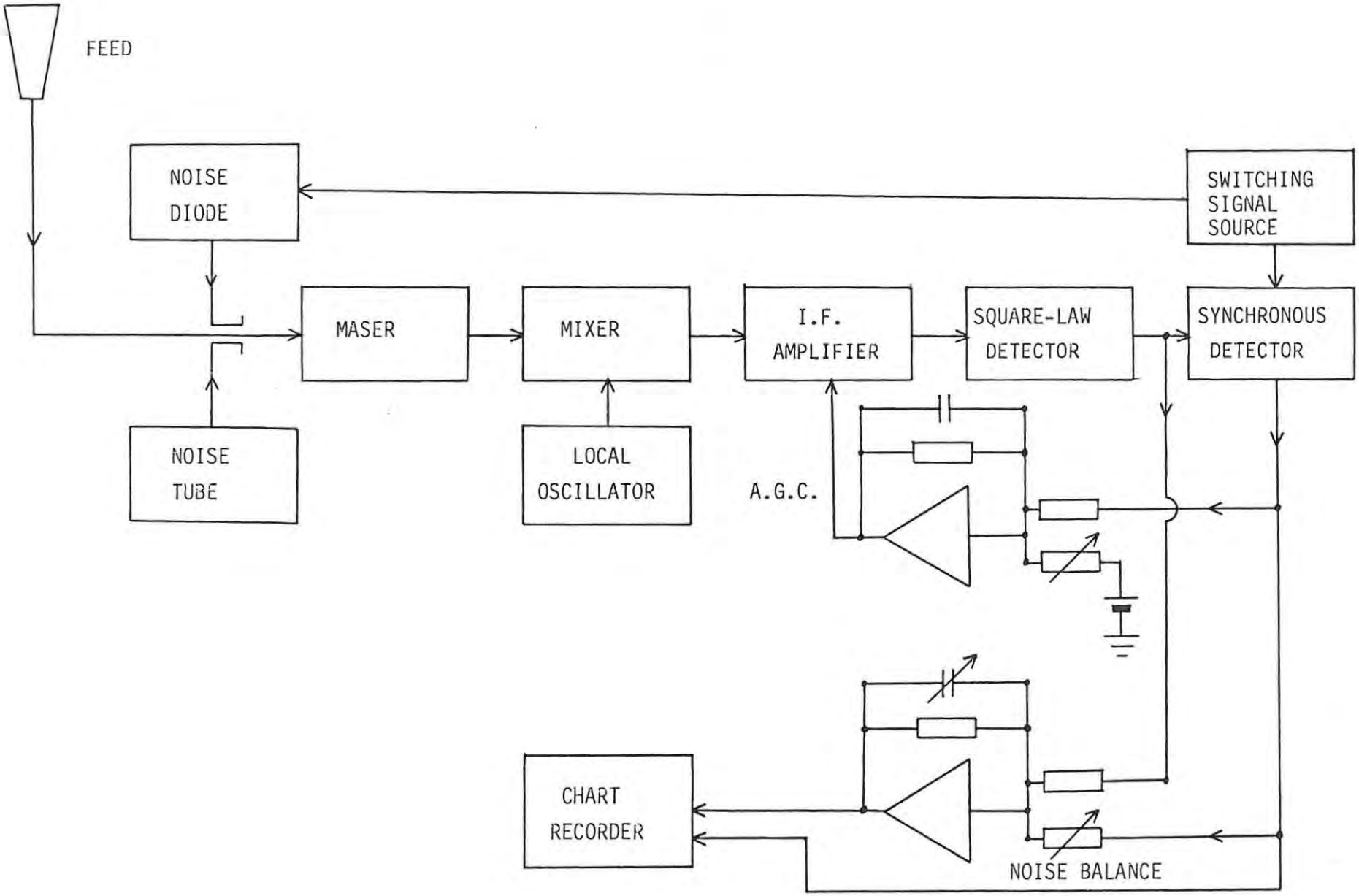
FEED
NOISE DIODE
SWITCHING SIGNAL SOURCE
MASER
MIXER
I.F. AMPLIFIER
SQUARE-LAW DETECTOR
SYNCHRONOUS DETECTOR
NOISE TUBE
LOCAL OSCILLATOR
A.G.C.
CHART RECORDER
NOISE BALANCE

made up of a number of contributions: the cosmic background, galactic and extra-galactic radio sources, terrestrial sources (atmosphere and antenna spillover), attenuation in the antenna and feeds, the noise temperature of the maser and the noise temperature of the other stages of the receiver, the major contribution being due to the mixer. Thus the expression for the system noise temperature is

$$T_e = T_{cosmic} + T_b + T_{terr} + T_{loss} + T_{maser} + T_{mix}/G_{maser} \qquad 2.2.1$$

If the output baseline is to be stable all of these component temperatures and the maser gain, G_{maser}, must remain stable. The terrestrial component obviously cannot be controlled, but observations done during cloudless nights have the best baselines. The temperature of the feed cone is kept constant to within two degrees Celsius, thus keeping the feed loss components reasonably constant. The noise temperature of the maser is dependent on its physical temperature. If the cryogenic system is adjusted to be working at a temperature where it has maximum capacity, the temperature of the system is very stable, depending slightly on the orientation of the telescope. Due to the high gain of the maser (greater than 30dB) the contribution of the mixer is very small. Variations in the maser gain will, however, cause perceptible changes in the system temperature. These gain variations have two major causes: changes in the physical temperature of the maser and changes in the magnetic field required for the operation of the maser. Since the field produced by the electro-magnet depends on the temperature in the feed cone it is difficult to obtain a quantitative measure of how the maser gain affects the noise temperature, because the causes of the gain change also affect other sources of noise. If the reason for gain changes can be established (i.e. whether the magnetic field or the cryogenic temperature variations are responsible for the changes) then the effects can be calculated.

The minimum detectable temperature (r.m.s. noise temperature) for this type

of radiometer is (Nicolson 1970)

$$dT_e = 2T_e.(1+T_e/T_n)/(2B.t)^{1/2} \qquad 2.2.2$$

where t is the post-detection time constant and B is the bandwidth of the system, which is limited to 16 MHz by the maser. T_n is the noise temperature of the noise diode and T_e is the system noise temperature. For these observations the system temperature was typically 27K with the antenna pointing towards the zenith position and not pointing towards the galactic plane. The noise diode had a noise temperature of 45K, yielding a typical minimum detectable temperature of 15 mK using a 1 second integration period (i.e. a 1 second time constant on the chart recorder).

The output of the radiometer is connected to a chart recorder via a second-order low-pass filter with a switchable time constant, giving a visual indication of the system performance and a permanent record of any observation. An integrating digital voltmeter (D.V.M.), which is under computer control, is also conected to the radiometer, thus enabling the observing program to sample the radiometer output. The input to the D.V.M. is switchable to either the filtered or unfiltered radiometer output. For sky mapping observations the unfiltered output is used, and the D.V.M. set to a 0.1 second integration period. The resolution of the D.V.M. is 10μV, which corresponds to very nearly 1mK. The A.G.C. voltage is also monitored on the chart recorder, indicating changes in the maser gain.

A gas discharge tube is coupled to the feed of the maser via a directional coupler to provide a constant flux reference for system calibration. The noise tube is frequently calibrated against radio sources of known flux densities.

2.3 The Observing Technique

Because imaging radio telescopes are not practical due to the long wavelengths involved, radio brightness maps must be observed using either a scanning or an interferometric technique. For the observations presented in this thesis a scanning technique was used because of the large area of sky involved and the lack of multiple telescopes to form an interferometer.

The data were observed using declination scans, each scan tracking a constant right ascension. The first observations were made scanning in 1950 epoch co-ordinates. This meant that the command co-ordinates had to be precessed from 1950 to the current date. Later observations have been made using current co-ordinates for reasons discussed later. The pattern that the telescope traces out in the RA-Dec plane is shown in figure 2.3(a), the arrows indicating the motion with time. The apparent rotation of the celestial sphere from east to west is used to advance the right ascension for each scan. One night's observation of this form is called a raster, analogous to a television set display. The rasters start at sunset and end at sunrise, but the first hour of data is not used because the antenna environment temperature must be allowed to stabilize. While the temperature is stabilizing the baseline of the data drifts down.

The terrestrial noise contribution due to the atmosphere and antenna spillover is a function of antenna altitude, and thus varies with declination and hour-angle. Since this terrestrial contribution cannot be eliminated it must be consistent for each scan in an observation, so that it may be removed later. This implies that the antenna must track the same path in the HA-Dec plane for each scan in the raster. Figure 2.3(b) shows the motion of the antenna in the HA-Dec plane. The hour angle, and thus the terrestrial noise contribution, is different for up and down scans, but is the same for scans of the same direction. This is not strictly true if the

Figure 2.3

Raster scanning patterns:

(a) in the right ascension - declination plane,

(b) in the hour angle - declination plane.

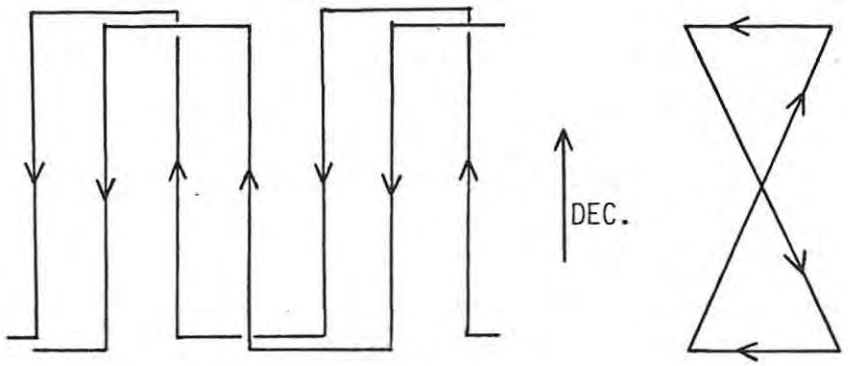

(a) (b)

map is observed in precessed co-ordinates. If the co-ordinates are precessed the hour angle varies cyclically with right ascension, one cycle every 24 hours of right ascension. The declination co-ordinates vary in a similar way. These cyclic variations can cause significant changes in the terrestrial noise contribution throughout the observation. For this reason later observations have not included precession.

The separation between successive scans in a single raster is determined by the length and speed of the declination scans. For the 39 degree scans used in these observations the spacing is 0.8 degrees. Since a 0.1 degree scan spacing is required for adequate sampling, eight interleaved rasters had to be observed. An example of two interleaved rasters is shown in figure 2.3(a) (the declination offset is for clarity). The use of interleaved rasters has the additional advantage that adjacent scans are independent of one another, and thus systematic effects are reduced. Note that 0.1 degrees of right ascension does not, in general, correspond to 0.1 degrees of arc on the celestial sphere. This is a function of both right ascension and declination:

$$\text{real angle} = \text{angle in RA} \times \cos(\text{Dec}) \qquad 2.3.1$$

This is commonly called the 'cosine Dec' compression. This implies that for scans below -60 degrees declination it is only necessary to sample at 0.2 degree intervals in right ascension. Each raster is observed three times in order to ensure reliable data, thus 24 nights of observation were required for the map presented.

In order to be able to remove the declination-dependent terrestrial effects it is necessary that each raster includes 'cold sky'. This is an area of radio sky which contains no significant large scale radio structure. This is used as a zero reference.

A program was written to implement this technique, called SKYMP (Mountfort

1981). Besides controlling the telescope throughout the observation it also logs the incoming data from the radiometer and writes it to 9-track magnetic tape together with co-ordinate and other relevant information. The only operator intervention required is to load the tape and start the program in the evening, and close it down in the morning.

2.4 Data validation

There is no way to display in real time the data being observed. The chart record provides a rough indication of how the system is performing, but does not show much detail. Programs have been written for the R.A.O. computers which allow a preliminary look at the raw data directly after a night's observation. BINTD, written by P.Mountfort, reads data from an observation tape (one raster) and writes it to a random access disc file, after reducing each scan into 256 declination bins. Binning consists of averaging data samples which fall into equally spaced intervals of declination, thus creating average data samples with regularly spaced declination coordinates. The right ascension of each sample in the scan is assumed to be the nominal right ascension of the scan for simplicity, remembering that these programs are only used to check the validity of the data.

Program BACOF subtracts a profile representing the atmospheric and terrestrial background from the binned scans. It was written by P.Mountfort and later modified by J.Jonas. The background profile is estimated to be represented by the fifth lowest binned sample for each declination interval. A low order polynomial is fitted to the 256 points obtained so that a smooth profile may be subtracted from the data.

The resulting data may be displayed in two formats, either as hidden line plots of declination scans using program RPLOT, or as hidden line plots of drift scans of the raster using program HIDPL. RPLOT was written by J.Jonas

and modified by A.Greybe, and HIDPL was written by A.Greybe and modified by J.Jonas.

In order to reduce the noise on the data, the scans may be filtered prior to plotting using a simple one dimensional Fourier Transform filter program, FILT, written by J.Jonas. The particular spatial frequency filter used was a Hamming window in order to reduce edge effects.

These processes are completely local to the observatory and in no way affect the data on the magnetic tape. They serve only as a 'quick look' facility to detect faults in the system or observation, and allow a preview of interesting features.

2.5 Data Reduction

All of the data reduction is performed on the Rhodes University I.C.L. 1904S computer. This is a relatively old mainframe with limited core and disc storage, which limited the scope of the data reduction process. All of these reduction programs were written by P.Mountfort (Mountfort 1981) and are outlined very briefly below. The reduction process falls into four distinct sections: binning and reformatting, drift removal, terrestrial background removal and raster recombination. Medians are often used in preference to means in the reduction to reduce the effects of uncertain data (Tukey 1977, Wall 1979).

As mentioned previously, the data set consists of a number of interleaved rasters, each of which was observed at least 3 times. All of the observation tapes are passed through the binning and reformatting process. The highly redundant ASCII format tapes are read and the data is subjected to a three point median filter to eliminate spurious spikes in the data. The co-ordinates recorded on the tape are derived directly from the digital readouts of the telescope. Pointing corrections are applied to these co-

ordinates and they are also precessed if necessary. The data are then binned into 0.1 degree declination intervals and written out as one record per run (scan). For each of these records there are associated two other records. One contains the average right ascension deviations for each declination bin (to take into account bad antenna tracking), and the other the number of D.V.M. samples that went into each declination bin. These two types of record are used for raster recombination. Associated with each record is a header which labels its type, observation number, nominal right ascension, starting declination and number of declination bins. Two other streams of reduced data are produced, one of which is used for baseline drift compensation and the other for background removal. The data for both of these streams is binned into 1.6 degree (twice the antenna beamwidth to first nulls) declination bins using medians rather than means in order to remove point sources.

The next step in the processing removes a base surface from each observation. This base surface is made up of temperature contributions from the terrestrial background and instrumental drift. Figure 2.4 is a typical example of the shape of this surface, which would be different for each observation. Ideally the declination profile (the shape of the terrestrial background contribution) of this surface would be independent of right-ascension, but was not for these observations because of the effects of precession. If the instrumental drift varies slowly enough the drift profile is independent of declination. Because the two contributions are orthogonal, they may be removed separately. For these observations the instrumental drift was removed first, and then the terrestrial background. Wide binned data is used for these removals in order to reduce the volume of the data.

Figure 2.4

A typical base surface due to atmospheric and terrestrial background and receiver baseline drift.

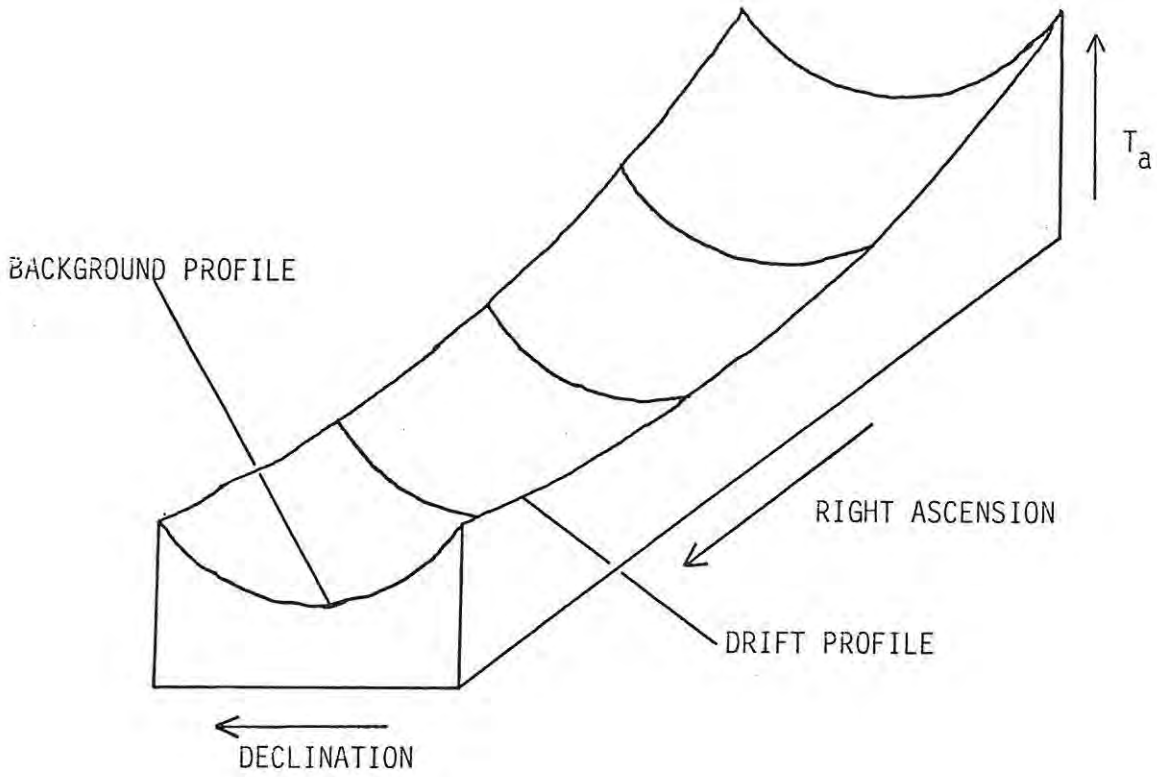
T_a
BACKGROUND PROFILE
RIGHT ASCENSION
DRIFT PROFILE
DECLINATION

As discussed in a previous section, drift in the radiometer output has a number of possible causes. If the maser gain drift is only due to variations in the magnetic field surrounding the maser its effect can be calculated using the maser gain recorded on the chart recorder at the time of the observation. The relationship between maser gain and radiometer output variation may be deduced empirically. The other drift effects result from changes in the telescope environment, such as condensation on the feed cone. These sources of drift cannot be measured directly, but still have to be removed. In order to quantify these drift effects it is necessary that for each point on the map there is at least one of the three repeated observations unaffected by unmeasurable drift. The unaffected sections of each raster are selected by visual inspection of right-ascension scans constructed from the 1.6 degree binned drift data. By comparing scans from different observations against each other, the regions of each observation which are affected by drift become apparent. The 1.6 degree binned drift data from the unaffected regions are combined to produce a highly smoothed map, which is assumed to be free of any spurious drift effects. The wide binned drift data for each observation are compared to this smooth map and the differences recorded. These differences represent an approximation of the unmeasurable drift and are combined with the calculated drift due to the maser gain variation, and this combined drift is removed from the 0.1 degree binned data. This subtraction is performed together with the removal of the terrestrial background component, which is described below.

Background subtraction is performed on each raster individually because each observation will have a different background profile depending on the hour angle at which it was observed. Each raster is split into north (up) and south (down) scans, because their profiles will also differ slightly, as explained in section 2.3. The process below refers to one direction of scan

for one raster and must be repeated for both directions and for all rasters. By comparing the wide binned background data for all right ascensions the twenty lowest temperatures for each 1.6 degree declination interval are recorded. The astronomer then selects which level of these 20 sets of temperatures has the best compromise of noise and real radio source contributions: the higher levels are less noisy, but contain real radio structure and vice versa. A least mean squares polynomial of temperature as a function of declination is fitted to the chosen levels, the degree of the polynomial being chosen by inspection of the fit. Fourth, fifth or sixth order polynomials are normally sufficient for an acceptable fit. This polynomial, which represents the terrestrial background profile, is combined with the drift contribution and the resulting base surface is subtracted from the 0.1 degree binned data.

The last process in the construction of the raw map is the combining of the separate rasters which have had a base surface removed. This involves the creation of a regular grid of temperatures, each grid point being the median of the binned data which fall within that grid area. The grid area has the same dimensions as the grid spacing. Since the telescope does not track perfectly, the actual right ascension of each sample may differ by more than a grid spacing from the nominal right ascension of the scan to which it belongs. Samples are assigned to grid areas using their actual right ascensions. In this way samples with large tracking deviations are not lost. The median takes into account the D.V.M sample count data produced by the reformatting stage. The resulting grid of medians is written to a serial access disc file in the form of a matrix of temperatures.

Chapter 4 relates this matrix to the actual radio brightness distribution. Knowing this relationship it is possible to enhance and manipulate the data using digital techniques, which are described in chapter 5. The next chapter describes the mathematical theory which is used in chapters 4 and 5.

CHAPTER 3 FOURIER TRANSFORM THEORY

The Fourier transform is a mathematical tool which has become increasingly popular in scientific circles because it may be used to simplify some mathematical problems very neatly. The use of the Fourier transform was given a boost when the Fast Fourier Transform algorithms were developed, which allow fast and efficient numerical calculation of the transforms for sampled data. The reasons for wishing to perform Fourier transforms on these observed data vary for different disciplines. The frequency spectrum of the data may be required, as in the case of radio astronomy spectral line studies, or it may be more convenient to process the data in the transform domain, as in image processing. Examples of digital image processing are given in a later chapter. Not only is the Fourier transform useful for data manipulation. The Fourier transform may also be used to explain physical processes which affect the data. The specific case of a scanning radio telescope is considered in the next chapter.

This chapter will introduce the Fourier transform and other related mathematics required to analyze the observing and data reduction processes described in following chapters. I have brought together relevant sections of Fourier theory from various sources so as to have one coherent body of theory. This theory is presented so that it may be conveniently referenced in the analysis.

Initially the analytic transforms for one and two dimensions are defined. Convolution and correlation describe the response of many physical measuring instruments, and these processes may be simplified by the use of the Fourier transform. This is discussed in section 3.2. Basic theorems are listed, and then the concept of generalized functions is introduced with its implications in Fourier theory. This is required to relate the Discrete

Fourier Transform (D.F.T.) to the analytic transform. In section 3.6 the D.F.T. is introduced and it is related to the analytic transform, not derived from it. Finally, the efficient computation of the D.F.T. is discussed.

3.1 The Analytic Fourier Transform

In many instances in Physics it is convenient to consider functions in two forms, that is, the original function, and its Fourier transform. Depending on the application this transform function will have different physical significance. The Fourier transform of a one-dimensional function, g(x), is defined as:

$$G(s) = \int_{-\infty}^{\infty} g(x).\exp(-i2\pi xs)\, dx \qquad 3.1.1$$

where x is considered to be a spatial coordinate, implying that g(x) is a function varying with displacement from some origin. The independent variable, s, is then a frequency coordinate and G(s) represents the amplitude and phase of the Fourier components of g(x). G(s) is the complex spectrum of g(x). In the most general case both g(x) and G(s) are complex functions. The conditions needed for the existence of this integral are:

i) $\int_{-\infty}^{\infty} |g(x)|^2\, dx$ exists, and

ii) the discontinuities of g(x) are finite.

When dealing with generalized functions these conditions are violated (discussed later), so they must be thought of as sufficient rather than necessary.

Given the transform function G(s) it is possible to reconstruct g(x) using

the other integral of the Fourier transform pair:

$$g(x) = \int_{-\infty}^{\infty} G(s).\exp(+i2\pi xs)\, ds \qquad 3.1.2$$

which is similar to equation 3.1.1 except for the different sign in the exponential argument. We discriminate between the forward and reverse transforms by refering to them as the 'minus i' and 'plus i' transforms respectively. Most of the theory here will employ the one-dimensional transform for clarity. The equations of the two-dimensional Fourier transform, analogous to equations 3.1.1 and 3.1.2, are defined as:

$$G(u,v) = \int_{-\infty}^{\infty}\int_{-\infty}^{\infty} g(x,y).\exp(-i2\pi.(ux+vy))\, dx\, dy \qquad 3.1.3$$

$$g(x,y) = \int_{-\infty}^{\infty}\int_{-\infty}^{\infty} G(u,v).\exp(+i2\pi.(ux+vy))\, dx\, dy \qquad 3.1.4$$

Most of the properties of the one dimensional transform generalize to two dimensions. For convenience the symbol $\geqslant$ is used to indicate the Fourier transform, i.e. $g(x) \geqslant G(s)$ and $g(x,y) \geqslant G(u,v)$.

3.2 Convolution and Correlation

Convolution is a mathematical device which conveniently describes a number of processes in measurement systems and data processing. In the next chapter it is used in the discussion of the sky mapping observation technique and subsequent data reduction. For the one dimensional case the convolution of two functions is defined as:

$$h(a) = f * g = \int_{-\infty}^{\infty} f(x).g(a-x)\, dx \qquad 3.2.1$$

When extended to two dimensions it has the form:

$$h(a,b) = f * g = \int_{-\infty}^{\infty}\int_{-\infty}^{\infty} f(x,y).g(a-x,b-y)\, dx\, dy \qquad 3.2.2$$

Figure 3.1

Illustration of the convolution process in the spatial domain and the corresponding multiplication in the spatial frequency domain.

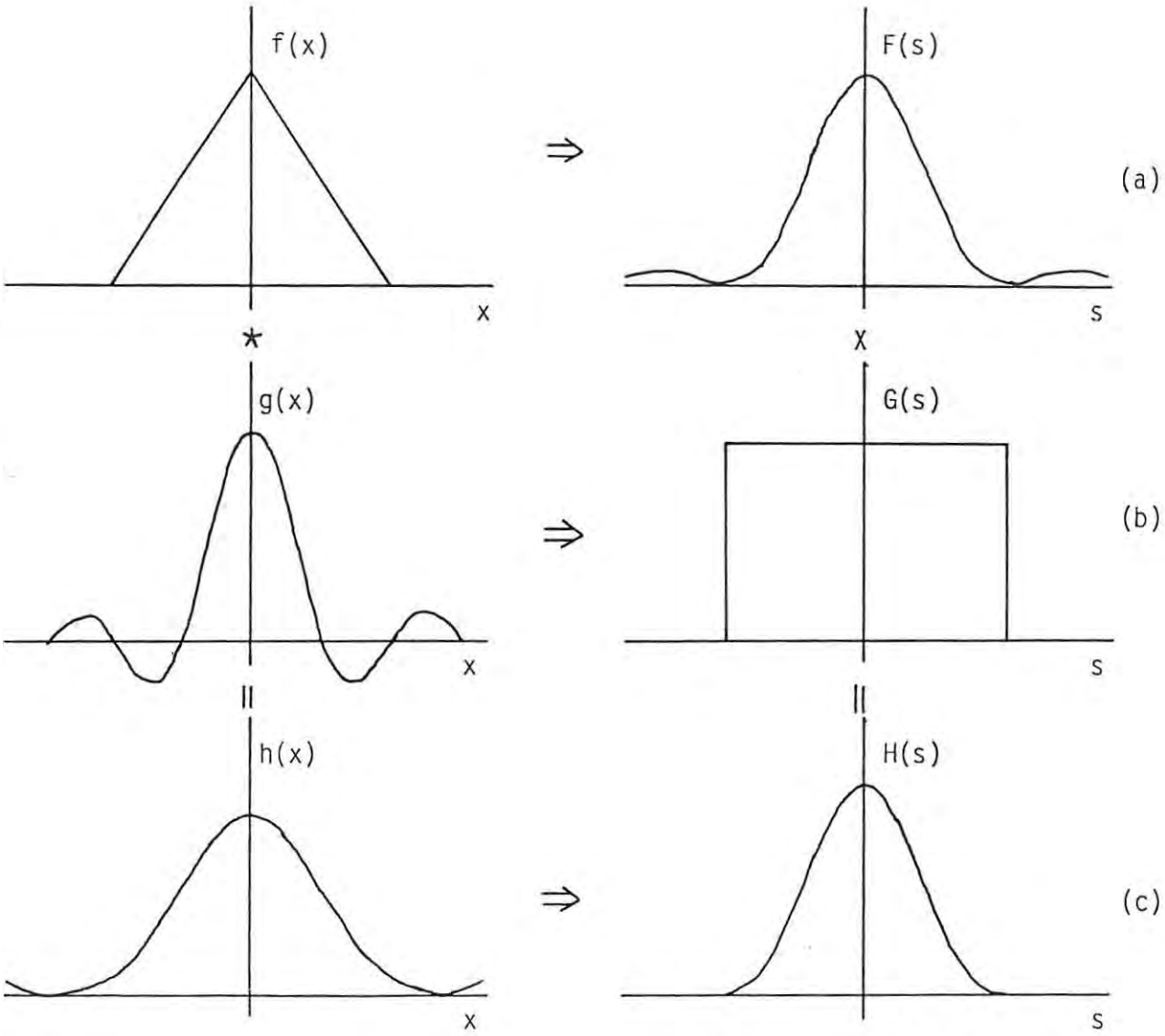
f(x)
x
⇒
F(s)
s
(a)
*
X
g(x)
x
⇒
G(s)
s
(b)
=
=
h(x)
x
⇒
H(s)
s
(c)

It is apparent that convolution is a fairly complicated procedure, perhaps involving a difficult integration. Transforming both sides of equation 3.2.1 simplifies the expression to (Bracewell 1965):

$$H(s) = F(s).G(s) \qquad 3.2.3$$

where F(s), G(s) and H(s) are the Fourier transforms of f(x), g(x) and h(x) respectively. This also applies for the reverse transform,
i.e. if H(s) = F(s) * G(s) then h(x) = f(x).g(x) .
This may be summed up by saying that convolution in one domain corresponds to multiplication in the other, which is a mathematically simpler process.
We are now in a position to explain how convolution may be used as a smoothing process. Convolution appears to be a weighted running mean, and intuitively has a smoothing function. The mechanism of this smoothing may also be understood by considering the corresponding process in the transform domain. Most functions (certainly continuous functions) have transforms which decay to zero with s tending to either plus or minus infinity. Two such functions and their transforms are illustrated in figures 3.1(a) and 3.1(b). In this example G(s) has a smaller extent along the s-axis than F(s). The convolution of f(x) and g(x) corresponds to the multiplication of the two frequency domain functions F(s) and G(s), and thus the higher frequencies of f(x) are attenuated by this multiplication. Thus convolving f(x) with g(x) results in a smoother function, h(x), because H(s) does not contain the high frequency terms of F(s). In this discussion g(x) was considered to be the convolving function, but since convolution is commutative, both functions play the same role. In physical applications it is convenient to think of one of the functions scanning across the other, and this distinction is maintained. Convolution in two dimensions is

exactly analogous, except that the convolving function is displaced about the x-y plane rather than along an axis.

A process closely related to convolution is cross-correlation, which is defined by the equation:

$$h(a) = f \bigstar g = \int_{-\infty}^{\infty} f^*(x-a).g(x)\, dx \qquad 3.2.5$$

for one dimensional functions. $f^*(x)$ is the complex conjugate of $f(x)$. From this it is apparent that

$$h(a) = f \bigstar g = f^*(-) * g$$

where $f(-) = f(-x)$, the dummy variable being left out to avoid confusion. Therefore:

$$H(s) = F^* * G \qquad 3.2.6$$

A special case of the cross-correlation function is the auto-correlation function, where the two functions are identical. For a complex function $f(x)$ the A.C.F. is given by:

$$\tau(a) = \int_{-\infty}^{\infty} f^*(x-a).f(x)\, dx \qquad 3.2.7$$

The auto-correlation theorem, which is easily derived from equation 3.2.6, states that the Fourier transform of the A.C.F. of a function $f(x)$ is $|F(s)|^2$, where $F(s)$ is the Fourier transform of $f(x)$. Since $|F(s)|^2$ defines the power spectrum of the function $f(x)$, we may obtain the power spectrum of any function by transforming its A.C.F. The power spectrum is purely real and thus contains no phase information.

3.3 Basic Theorems and Properties

Theorems which are useful for the manipulation of Fourier transform expressions are listed without proofs below (Bracewell 1965). In all cases F(s) and G(s) are the transforms of f(x) and g(x) respectively.

Similarity Theorem:

$$f(ax) \geqslant \frac{F(s/a)}{a} \qquad 3.3.1$$

Linearity Theorem:

$$a.f(x) + b.g(x) \geqslant a.F(s) + b.G(s) \qquad 3.3.2$$

Shift Theorem:

$$f(x-a) \geqslant \exp(-i2\pi as).F(s) \qquad 3.3.3$$

Any function may be expressed as the sum of an odd and an even component. Furthermore these components may be split into real and imaginary parts, i.e. in general a function consists of four terms: real even, imaginary even, real odd and imaginary odd. Using the linearity theorem it is possible to transform these four components separately and sum the resulting transforms to reconstruct the required transform. The type of transform a function will have is given below.

$$\begin{array}{l} f(x) = \mathrm{Re}(e(x)) + i.\mathrm{Im}(e(x)) + \mathrm{Re}(o(x)) + i.\mathrm{Im}(o(x)) \\ \qquad\qquad \updownarrow \qquad\qquad \updownarrow \qquad\qquad \swarrow\!\!\searrow \\ F(s) = \mathrm{Re}(E(s)) + i.\mathrm{Im}(E(s)) + \mathrm{Re}(O(s)) + i.\mathrm{Im}(O(s)) \end{array}$$

e.g. if f(x) is real (only consists of Re(e(x)) + Re(o(x))) , then F(s) has the terms Re(E(s)) + i.Im(O(s)), implying that F(s) is Hermitian.

The equivalent width of a function is defined to be the width of that rectangle which has the height of the central (zero) ordinate of the function and encloses the same area as the function, i.e.

(Bracewell 1965, p148):

$$E(f) = \frac{\int_{-\infty}^{\infty} f(x)\,dx}{f(0)} \qquad 3.3.4$$

This has its obvious extension in two dimensions.

Another characteristic width of a function is its autocorrelation width, defined by (Bracewell p154):

$$A(f) = \frac{\int_{-\infty}^{\infty} (f \star f^*)\,dx}{(f \star f^*)_0}$$

$$= \frac{\int_{-\infty}^{\infty} f\,dx \int_{-\infty}^{\infty} f^*\,dx}{\int_{-\infty}^{\infty} f.f^*\,dx} \qquad 3.3.5$$

This also has its natural extension in two dimensions.

Given a function f(x) and its transform F(s), the equivalent width of the modulus squared of one function is the reciprocal of the autocorrelation width of the other, i.e. (Bracewell p154):

$$E(f.f^*).A(F) = 1$$

and $$E(F.F^*).A(f) = 1 \qquad 3.3.6$$

3.4 Some Useful Functions

It is convenient to define a function denoted by the symbol $\delta(x)$, known as the impulse function. It is not a function in the normal sense of the word, but rather a generalized function (Bracewell 1965). The property:

$$\int_{-\infty}^{\infty} \delta(x).f(x)\,dx = f(0) \qquad 3.4.1$$

gives the most precise definition of the symbol. Generalized functions are also referred to as distributions or functionals (Papoulis 1962). The

Figure 3.2

Graphical representation of some useful functions:

(a) the impulse function

(b) the shah function

(c) the rectangle and triangle functions.

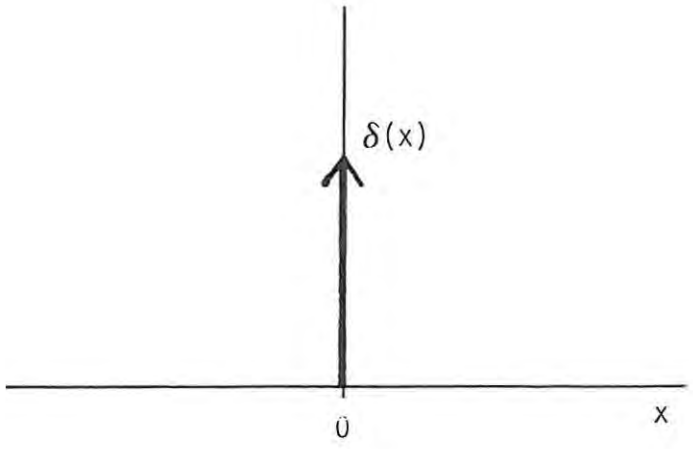

(a)

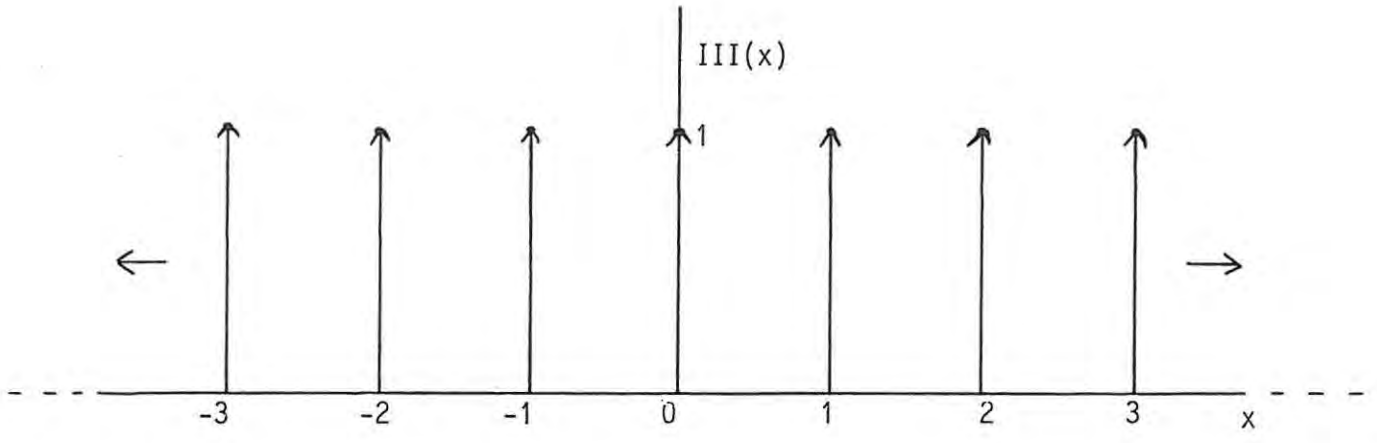

(b)

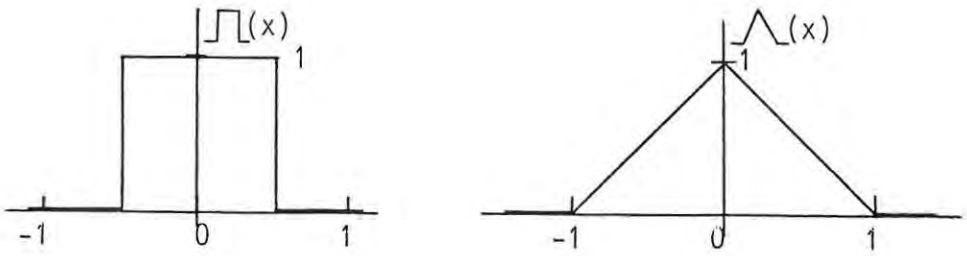

(c)

symbol, $\delta(x)$, is represented graphically in figure 3.2(a). It may be shown that the transform of a generalized function is also a generalized function (Bracewell 1965). $\delta(x)$ has a discontinuity at x=0, which does not satisfy the sufficient conditions for the existence of the Fourier transform. Using distribution theory the transform of the impulse function may be shown to be unity,

i.e. $$\delta(x) \Rightarrow 1$$

and similarly $$1 \Rightarrow \delta(x) \qquad 3.4.2$$

Transforms of other generalized functions may be derived by manipulating the above relations. By the shift theorem (equation 3.2.3):

$$\exp(+i\pi x) \Rightarrow \delta(s-\tfrac{1}{2})$$

$$\exp(-i\pi x) \Rightarrow \delta(s+\tfrac{1}{2})$$

Using these two relations the following two are easy to derive:

$$\sin(\pi x) \Rightarrow \tfrac{1}{2}i(\delta(s+\tfrac{1}{2}) - \delta(s-\tfrac{1}{2})) = i\sqcup(s) \qquad 3.4.3$$

$$\cos(\pi x) \Rightarrow \tfrac{1}{2}(\delta(s+\tfrac{1}{2}) + \delta(s-\tfrac{1}{2})) = \sqcap(s) \qquad 3.4.4$$

Thus it is possible, using generalized functions, to represent the transforms of functions which violate the sufficient conditions of existence.

Another useful generalized function which may be constructed using the impulse function is represented by the shah symbol, otherwise known as the replicating or sampling symbol,

$$III(x) = \sum_{n=-\infty}^{\infty} \delta(x-n)$$

The graphic representation of the shah symbol is shown in figure 3.2(b). The shah function is useful for representing a function which has been sampled at uniform intervals. This is simply the product of the function to be sampled and III(x).

Figure 3.3

Illustration of the sampling and replication properties of the shah function.

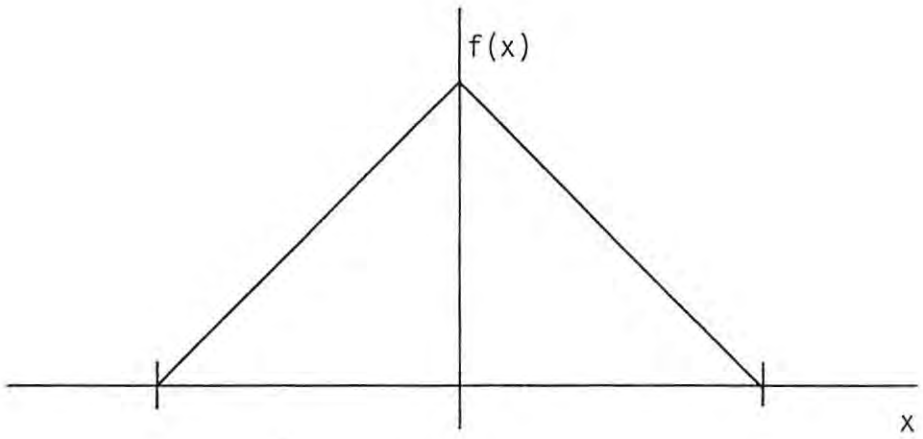
f(x)
x

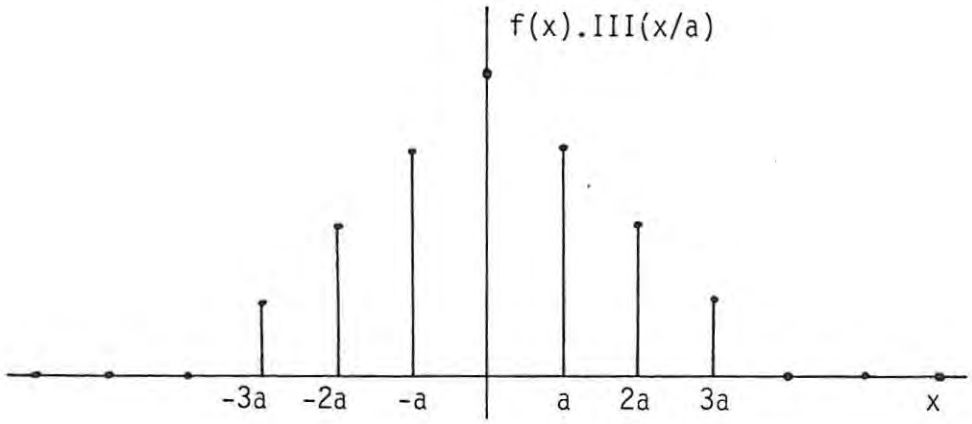
f(x).III(x/a)
-3a
-2a
-a
a
2a
3a
x

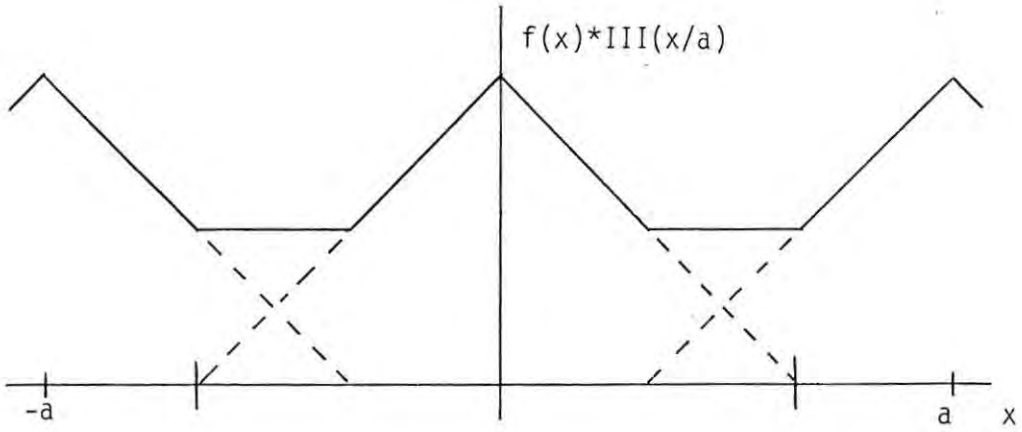
f(x)*III(x/a)
-a
a
x

i.e. $$III(x).f(x) = \sum_{n=-\infty}^{\infty} f(n).\,\delta(x-n) \qquad 3.4.5$$

Convolution by III(x) displays its replicating property:

$$III(x) * f(x) = \sum_{n=-\infty}^{\infty} f(x-n) \qquad 3.4.6$$

These two properties are illustrated in figure 3.3.

As mentioned before, the transform of a generalized function is again a generalized function, and in the case of the shah function:

$$III(x) \geqslant III(s) \qquad 3.4.7$$

$$III(ax) \geqslant III(s/a) \qquad 3.4.8$$

Figure 3.2(c) illustrates two other useful functions: the rectangular function and the triangle function. These functions have the following Fourier transforms:

$$\sqcap(x) \geqslant \mathrm{sinc}(s) \qquad 3.4.9$$

$$\wedge(x) \geqslant \mathrm{sinc}^2(s) \qquad 3.4.10$$

where $\mathrm{sinc}(s) = \sin(\pi s)/(\pi s)$

3.5 The Hankel Transform

The Hankel transform is one of a number of integral transforms which are related to the Fourier transform. If a two-dimensional function is circularly symmetric about the origin, then it is really only dependent on one variable, r, i.e.

$$f(x,y) = g(r) \qquad 3.5.1$$

$$r^2 = x^2 + y^2 \qquad 3.5.2$$

The Fourier Transform, F(u,v), of such a function is also circularly symmetric. Thus we may write:

$$F(u,v) = G(q) \qquad 3.5.3$$

$$q^2 = u^2 + v^2 \qquad 3.5.4$$

The functions g(r) and G(q) are related by the Hankel transform, which is a

one dimensional integral transform using a Bessel function kernel (Bracewell 1965). The Hankel transform pair of defining equations, analogous to the Fourier transform pair, is listed below:

$$G(q) = 2\pi \int_0^\infty g(r).J_0(2\pi qr).r\ dr \qquad 3.5.5$$

$$g(r) = 2\pi \int_0^\infty G(q).J_0(2\pi qr).q\ dq \qquad 3.5.6$$

3.6 The Discrete Fourier Transform

The Discrete Fourier transform, or D.F.T. , is a much misunderstood and misused concept. In order to reduce this confusion it will be introduced by definition, and not by deduction from the analytic Fourier transform. The analytic Fourier transform involves analytic functions of continuous variables, while the D.F.T. deals with sequences of numbers. The relationship between these two mathematical transforms is deduced, following Terry's treatment (1978), to show that the D.F.T. may be used to approximate the continuous transform of a function, given certain conditions. The D.F.T. may also be performed on a sequence of data samples from some physical experiment (which may be recorded on a digital device) in order to obtain the spectral components of an observed phenomenon.

The minus-i D.F.T. of a finite sequence of generally complex numbers

$$h_j \qquad j = 0(1)N-1$$

is defined to be:

$$H_k = \sum_{j=0}^{N-1} h_j .\exp(-2i\pi jk/N) \qquad k = 0(1)N-1 \qquad 3.6.1$$

Using the orthogonality of the harmonic factors it is easy to show that:

$$h_j = 1/N \sum_{k=0}^{N-1} H_k \,.\exp(+2i\pi kj/N) \qquad j = 0(1)N-1 \qquad 3.6.2$$

This is the plus-i D.F.T. The above equations can be considered to be defining functions for two infinite periodic sequences of period N by dropping the restriction that the subscripts lie in the range (0,N-1). Therefore it is possible to calculate the D.F.T. of an infinite periodic sequence of period N by using any N consecutive values.

We now set about relating the D.F.T. to the analytic Fourier transform. Given an analytic function h(x) and its transform H(s), the definition of the Fourier transform states that (equation 3.1.1):

$$H(s) = \int_{-\infty}^{\infty} h(x).\exp(-2i\pi sx)\, dx \qquad 3.6.3$$

Assume that H(s) is only calculated at discrete, equidistant values of the frequency coordinate, i.e. at

$$s = m\Delta s \qquad m = -\infty(1)\infty \qquad 3.6.4$$

Δs is called the sampling period in the frequency domain.

We define $X = 1/\Delta s$ for convenience, the significance of which will be seen later. Substituting equation 3.6.4 into 3.6.3 :

$$H(m\Delta s) = \int_{-\infty}^{\infty} h(x).\exp(-2i\pi mx/X)\, dx \qquad 3.6.5$$

The exponential factor is periodic with respect to x, with period X, for a given m, i.e. :

$$\exp(-2i\pi mx/X) = \exp(-2i\pi m(x+nX)/X) \qquad n \text{ any integer}$$

The integral in equation 3.6.5 may be split up into an infinite number of integrals, each over a range of X.

$$H(m\Delta s) = \sum_{n=-\infty}^{\infty} \int_{nX}^{(n+1)X} h(x).\exp(-2i\pi mx/X)\, dx \qquad 3.6.6$$

By making the change of variable $x = y+nX$, $0 \leqslant y < X$, and using the periodicity pointed out above, this simplifies to:

$$H(m\Delta s) = \int_0^X \sum_{n=-\infty}^{\infty} h(y+nX).\exp(-2i\pi my/X)\, dy$$

or:

$$H(m\Delta s) = \int_0^X h'(y).\exp(-2i\pi my/X)\, dy \qquad 3.6.7$$

where

$$h'(y) = \sum_{n=-\infty}^{\infty} h(y+nX) = III(y/X) * h(y) \qquad 3.6.8$$

which is a periodic function of y, period X.

h'(y) is a replicated version of h(x) (cf section 3.4). Note that the replicated function is periodic, but not the original function. Since h'(x) is periodic it has a Fourier series expansion. Examining equation 3.6.7, it is clear that this is the equation for the coefficients of the Fourier series. Therefore the Fourier series expansion is given by:

$$h'(y) = 1/X \sum_{m=-\infty}^{\infty} H(m\Delta s).\exp(2i\pi my/X) \qquad 3.6.9$$

Assume that the replicated function is only known at discrete, equidistant values of x. It is only necessary to have samples of one period of the function to define it, so if we have N equidistant samples over one period then we only have values for h'(y) at:

$$y = j\Delta x = jX/N \qquad j = 0(1)N-1 \qquad 3.6.10$$

Substituting into equation 3.6.9:

$$X.h'(j\Delta x) = \sum_{m=-\infty}^{\infty} H(m\Delta s).\exp(2i\pi mj/N) \qquad 3.6.11$$

Noting the periodicity of the exponential factor, the infinite summation is

split into an infinite number of finite summations over 0 to N-1 :

$$X.h'(j\Delta x) = \sum_{l=-\infty}^{\infty} \sum_{k=0}^{N-1} H((k+Nl)\Delta s).\exp(2i\pi(k+Nl)j/N)$$

$$= \sum_{k=0}^{N-1} \sum_{l=-\infty}^{\infty} H((k+Nl)\Delta s).\exp(2i\pi kj/N)$$

or rewritten:

$$N\Delta x\, h'(j\Delta x) = \sum_{k=0}^{N-1} H'(k\Delta s).\exp(2i\pi kj/N) \qquad 3.6.12$$

where $H'(k\Delta s) = \sum_{l=-\infty}^{\infty} H((k+Nl)\Delta s) = III(s/(N\Delta s)) * H(k\Delta s)$

$H'(k\Delta s)$ is a sequence consisting of discrete samples of the replicated form of $H(s)$.

Comparing equations 3.6.12 and 3.6.2 it is apparent that sequences formed from N equally spaced samples of one period of the replicated forms of the functions $h(x)$ and $H(s)$ are related by the D.F.T. , i.e :

$$\Delta x.h'_j \quad D.F.T. \quad H'_k \qquad 3.6.13$$

where: $h'_j = h'(j\Delta x)$ and $H'_k = (k\Delta s)$ and $N\Delta x\Delta s = 1$

The above mathematics justifies the use of the D.F.T. for calculating the Fourier transform of a sampled function or data set under certain conditions. These conditions are best examined diagrammatically. Figure 3.4(a) shows a continuous function, $h(x)$, and its hypothetical transform $H(s)$. Replicated and sampled versions of these functions, $h'(x)$ and $H'(s)$, are illustrated in figure 3.4(b). Equation 3.6.13 implies that sequences formed from N consecutive values of both of these functions are related by the D.F.T. It is possible to show that these replicated and sampled functions are also related by the Fourier transform:

Given

$$h(x) \Rightarrow H(s)$$

Figure 3.4

Illustration of the relationship between the analytic Fourier transform and the discrete Fourier transform.

(a) Hypothetical analytic Fourier transform pair.

(b) Functions undersampled in both domains, and thus aliased in both domains.

(c) Spatial function undersampled, frequency function aliased.

(d) Neither function aliased.

(e) Truncation of the spatial sequence causing aliasing of the frequency function.

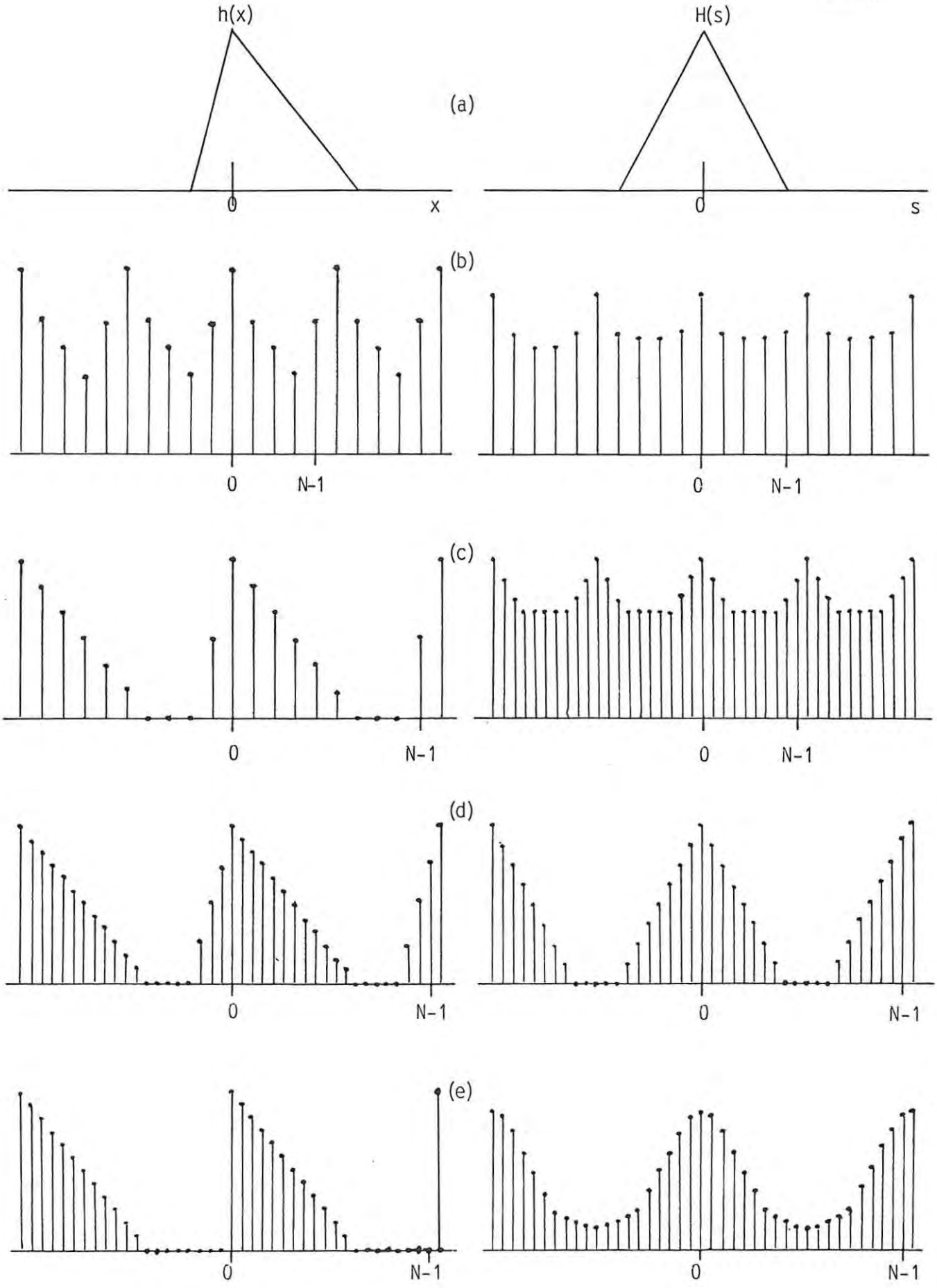
h(x)
H(s)
(a)
0
x
0
s
(b)
0
N-1
0
N-1
(c)
0
N-1
0
N-1
(d)
0
N-1
0
N-1
(e)
0
N-1
0
N-1

replicating the spatial function yields:

$$h(x) * III(x/X) = H(s).III(s/\Delta s)$$

sampling the resulting replicated function:

$$h(x) * III(x/X).III(x/\Delta x) = H(s).III(s/\Delta s) * III(s.\Delta x)$$

or: $$III(x/\Delta x).h'(x) = III(s/\Delta s).H'(s)$$

Thus the discrete functions in figure 3.4(b) are related by the analytic Fourier transform. Note that in this case the replicas of the spatial and the frequency functions overlap, a phenomenon called aliasing.

If the function h(x) has limited extent, then the aliasing in the spatial domain can be eliminated by choosing a long enough replicating period. Figure 3.4(c) illustrates such a case. Note that a sequence of N values of this function, h'(x), is exactly equivalent to the samples of the original function, h(x). Similarly the aliasing in the frequency domain can only be eliminated if the spectrum is limited in extent, i.e. h(x) is band-limited. The replicating period in the frequency domain depends on the sampling period in the spatial domain. If H(s) has a total extent S, then the sampling period must be less than 1/S if no frequency aliasing is to occur. This is an intuitive proof of the Sampling Theorem, which states that if a function has spectral components extending to a frequency F, then it must be sampled at a rate of at least 2F if no frequency aliasing is to occur. For the case in figure 3.4(d), the D.F.T. of N samples of the original function does return N samples of the original spectrum, H(s). If the original function is not sampled often enough the D.F.T. produces samples of an aliased version of the spectrum, as illustrated in diagram 3.4(c). The origin of the term aliasing is apparent from this diagram. In the overlap region various frequency components of the original spectrum are superimposed on one another, and the high frequency components from

replicated versions pose as low frequency components in the adjacent replications.

A complication arises if the spatial function is not limited in extent, or is only known over a limited domain. In such cases it is necessary to use a truncated version of the function. This spatial truncation is effectively the multiplication of the original spatial function by a rectangular function. This corresponds to the convolution of the original spectrum with a sinc function. The resulting spectrum will extend to infinity along the s-axis, and therefore the truncated function will not be band limited. In this case frequency aliasing is unavoidable, and so the D.F.T. of the truncated function is only an approximation to its spectrum. Figure 3.4(e) illustrates the case where the spatial function h(x) is truncated to the left of the origin.

There is an exception to this truncation problem. If the original function is periodic and band-limited, then the D.F.T. of samples of an integral number of periods of this function will return its exact spectrum, if the sampling theorem is satisfied. This may be understood intuitively because the replication of the truncated periodic function reconstructs it.

All of this theory generalizes to two dimensions. Replication in two dimensions corresponds to displacing the function about the x-y plane to points on a rectangular grid and superimposing. This is illustrated in figure 3.5.

The two dimensional D.F.T. pair of equations is defined as:

$$H_{mn} = \sum_{l=0}^{N-1} \sum_{k=0}^{M-1} h_{kl}.\exp(-2i\pi(km/N+ln/M)) \qquad 3.6.15$$

$$= \sum_{l=0}^{N-1} \left(\sum_{k=0}^{M-1} h_{kl}.\exp(-2i\pi km/M) \right).\exp(-2i\pi ln/N) \qquad 3.6.16$$

Figure 3.5

Illustration of replication in two dimensions.

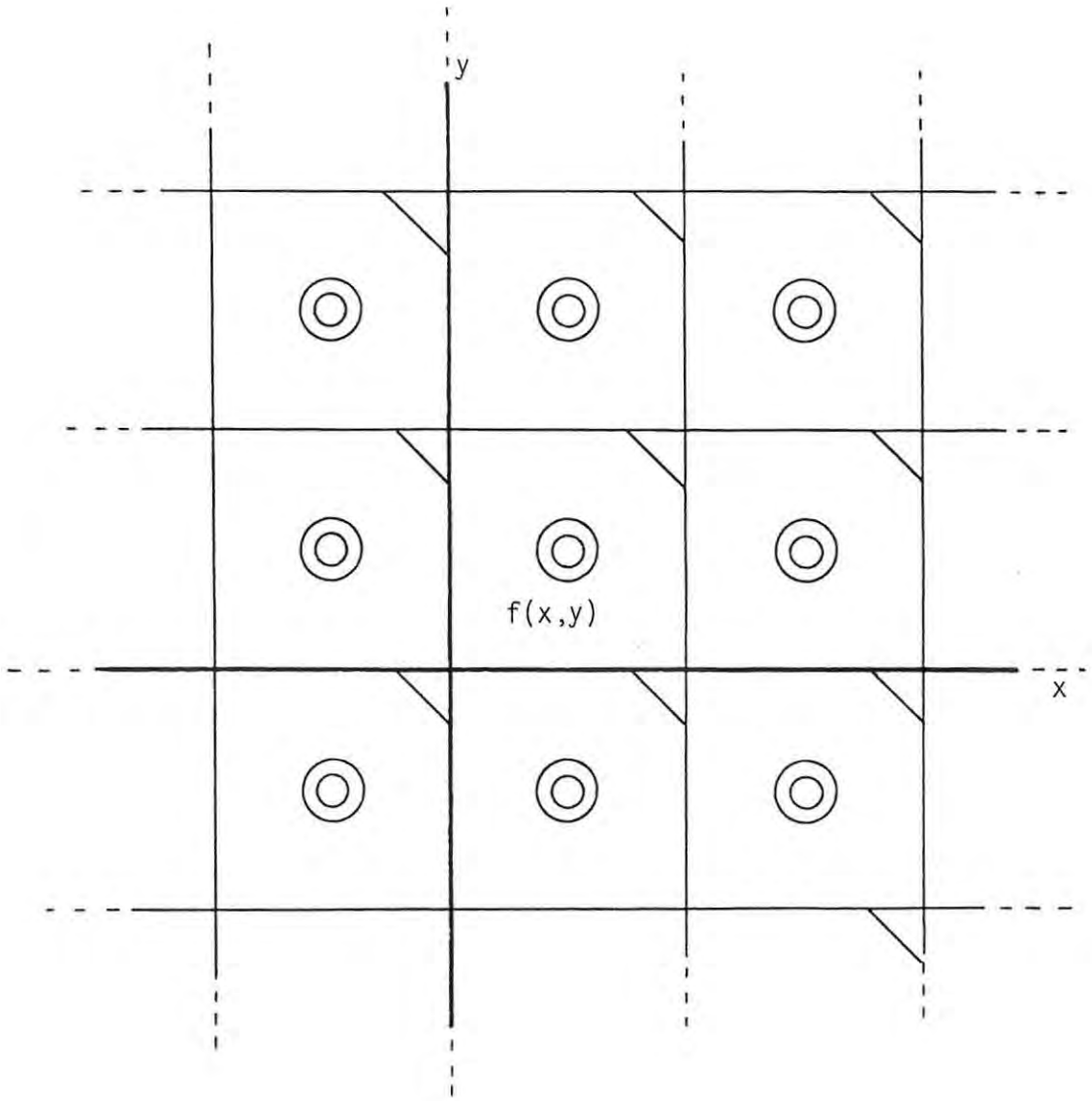
y
f(x,y)
x

and:

$$h_{kl} = 1/MN \sum_{n=0}^{N-1} \sum_{m=0}^{M-1} H_{mn}.\exp(+2i\pi(km/M+ln/N)) \qquad 3.6.17$$

$$= 1/MN \sum_{n=0}^{N-1} \left(\sum_{m=0}^{M-1} H_{mn}.\exp(+2i\pi km/M)\right).\exp(+2i\pi ln/N) \qquad 3.6.18$$

where h_{kl} and H_{mn} are N by M matrices. From the factored versions of these equations it is apparent that the two dimensional D.F.T.may be implemented using one dimensional D.F.T.'s. Individual columns or rows are transformed and then corresponding elements in these vectors are transformed, i.e. M+N one-dimensional D.F.T.'s are performed.

3.7 The Fast Fourier Transform

From the definition of the D.F.T. pair it appears that N^2 complex multiplications and N.(N-1) complex additions are necessary to perform the transform on a sequence of N numbers, making it computationally expensive. Under certain circumstances it is possible to reduce the computation significantly by using the Fast Fourier Transform algorithms (Brigham 1974, Brenner 1976).

The general F.F.T. algorithm may be applied to a sequence of any length N, the reduction in computation depending on the reducibility of N, i.e. if N may be reduced to prime factors then the process is more efficient than if N is prime itself. The most often used F.F.T. algorithm used is the base 2 algorithm, which applies when N is an integer power of two. In this case N is very reducible since all of its prime factors are two's. The base two algorithm reduces the number of complex multiplications to $N.\log_2 N$ and the number of complex additions to $N.\log_2 N$, clearly a substantial reduction in the computation required.

If the numbers in the sequence are purely real a further reduction of the

computation may be effected, using one of two methods (Brigham 1974, Brenner 1976). In the first method two N-point real sequences are transformed simultaneously using one complex N-point D.F.T. The second method transforms one N-point real sequence using a N/2-point complex D.F.T.

For the first method the two real sequences are combined to form a new complex sequence thus:

$$y_j = g_j + i.h_j \qquad j = 0(1)N-1 \qquad 3.7.1$$

The N-point D.F.T. is then performed on this complex sequence. It is then possible to extract the D.F.T.'s of the two original real sequences from the resulting sequence. This method does not require any additional harmonic weights since the sequences are separated by simple linear combinations of the elements of the calculated D.F.T. sequence.

In the second method the N-point real sequence, f_j, is split into two N/2-point real sequences:

$$h_j = f_{2j+1} \qquad j = 0(1)N/2-1$$

$$g_j = f_{2j} \qquad j = 0(1)N/2-1$$

As there are now two N/2-point real sequences we may calculate their D.F.T.'s using the method described above, using one N/2-point D.F.T. and a little unscrambling. It is then possible to reconstruct the D.F.T. of the original sequence using the expression:

$$F_k = H_k + G_k.\exp(-2i\pi k/N) \qquad k = 0(1)N-1 \qquad 3.7.2$$

It is clear that this method requires additional complex harmonic weights. Note that since the D.F.T. of a real function may be shown to be Hermitian, only half the sequence need be calculated to define the entire sequence. Both of the above methods require the same number of weights and computation.

The theory expounded in this chapter is applied in the following two chapters. Chapter 4 uses Fourier theory to simplify the description of how the physical observational processes and the digital data reduction processes affect the data, thus relating the raw map data to the original sky brightness distribution. Chapter 5 describes data processing techniques which either employ the D.F.T. or are best understood using Fourier theory.

CHAPTER 4 THE OBSERVING PROCESS

In order to perform quantitative analysis of the results of the observation it is necessary to know the effects of the observing apparatus and technique on the data. The recorded data does not represent the actual radio brightness distribution in the sky exactly. Chapter 2 introduced the observation and data reduction methods. This chapter is a mathematical analysis of the data recording and reduction processes. The resulting data is related to the the brightness distribution. The analysis also derives properties of the data which need to be known so that digital signal conditioning may be used to enhance the data. This signal processing is described in the next chapter.

The observation and reduction process has three distinct parts: the scanning of the antenna, the signal reception and digitization, and the reduction of the data to produce a sampled map. These three stages of observation are examined in the following sections. Fourier theory and notation are used to simplify the mathematics wherever possible

4.1 The Antenna

It is well known that the resolution of an antenna depends on the ratio of its physical size to its operating wavelength. The larger this ratio, the higher the resolution of the antenna. Thus for a given wavelength, the beamwidth reduces as the size of the antenna increases. The reciprocal nature of these two parameters may be explained using Fourier Transform techniques. The Fourier transform is a useful tool for discussing narrow beam antennas, because it relieves much of the mathematical drudgery involved in other methods. The reciprocity theorem for antennas states that the pattern and aperture of an antenna are the same for transmitting or

Figure 4.1

The coordinate system used in the analysis. The aperture of the antenna is parallel to the x-y plane. The circle is in the y-z plane

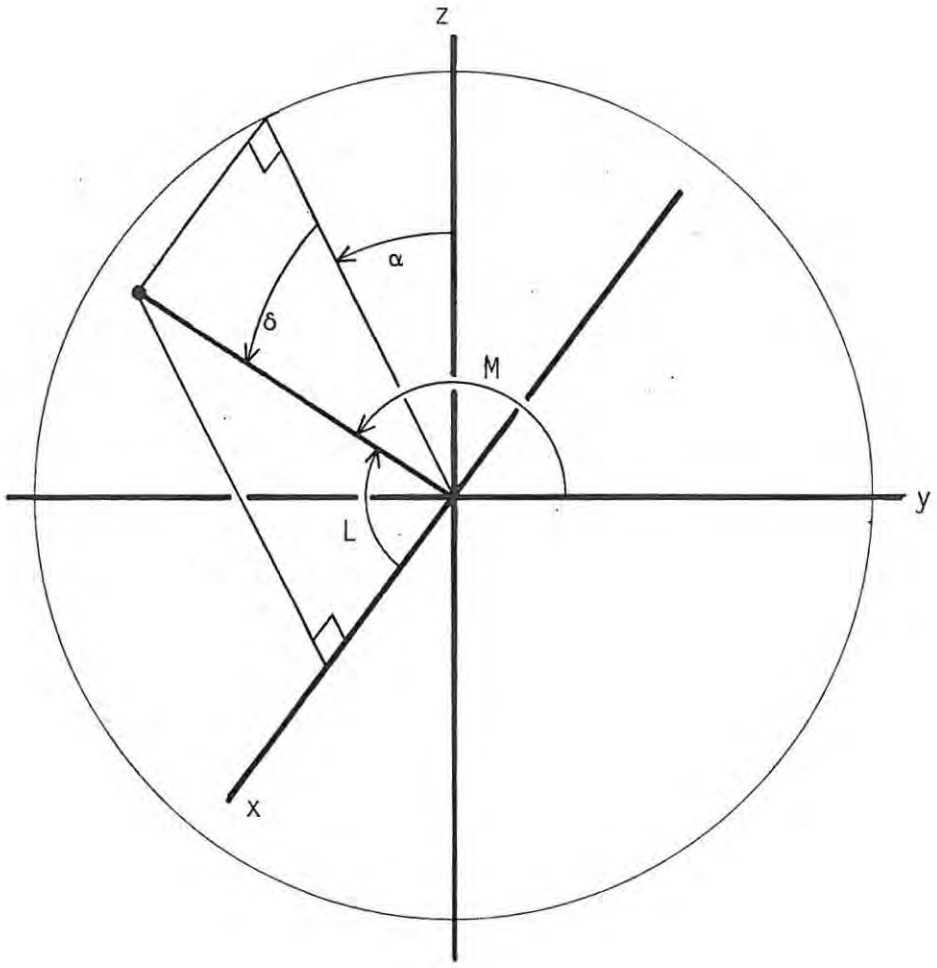

$\cos(L) = l$

$\cos(M) = m$

receiving (Kraus and Carver 1973). In the following discussion the antenna is considered to be either transmitting or receiving, depending on which is most convenient for the analysis.

4.1.1 The Field Intensity pattern and Aperture Illumination Function

The antenna pattern is a description of the directivity of an antenna. The field intensity pattern describes the complex electric field produced by the antenna per unit solid angle. The far field intensity pattern, $F(l,m)$, is of most use. This is the field intensity produced by the antenna at a distance greater than L, where L is numerically equal to the square of the diameter of the antenna divided by the wavelength of the radiation. For most common dish antennae the field intensity pattern has a large central peak normal to the plane of the aperture, called the main lobe. Other peaks in the response are called sidelobes.

The field intensity pattern is related to the aperture illumination function. The aperture illumination function, $E(x/\lambda,y/\lambda)$, is a measure of the complex electric field distribution across the plane of the aperture. For an ideal parabolic reflector this function would be purely real, but it is generally complex due to inaccuracies in the dish surface. The illumination function must be limited in spatial extent due to the physical limits of the antenna. The illumination function is affected by such things as the reflectivity of the dish surface, subreflector illumination and aperture blockage.

The far field intensity pattern and the aperture illumination functions of a narrow beam antenna are related by the Fourier transform. Given the geometry in figure 4.1 the relationship is given by (Bracewell 1965, Rusch and Potter 1970):

$$F(l,m) = \int_{-\infty}^{\infty}\int_{-\infty}^{\infty} E(x/\lambda,y/\lambda).\exp(-2i\pi/\lambda(lx+my)\ dx/\lambda\ dy/\lambda \qquad 4.1.1$$

i.e. $E(x/\lambda,y/\lambda) \geqslant F(l,m)$

If the beam is sufficiently narrow the direction cosines l and m may be approximated by the position angles δ and $-\alpha$, which correspond to declination and right ascension for an equatorially mounted antenna. Thus:

$$E(x/\lambda,y/\lambda) \geqslant F(\delta,-\alpha)$$

or: $$F(\delta,\alpha) \geqslant E(-x/\lambda,y/\lambda) \qquad 4.1.2$$

Therefore the Fourier transform of the far field intensity pattern is the aperture illumination function transposed about the y-axis.

Considering the far field pattern to be a function of angular spatial coordinates, its Fourier transform is an angular spatial frequency spectrum. The (u,v) plane is the angular spatial frequency domain. Therefore the spatial frequency distribution in the (u,v) plane is the same as the aperture illumination function in the $(-x/\lambda,y/\lambda)$ plane because of the relationship described by equation 4.1.2. The distinction between these two planes is kept because of their different physical significance.

4.1.2 The Power Pattern and Beam Solid Angle

The power pattern of an antenna is proportional to the square of the modulus of the field intensity pattern. The power pattern is the power per unit solid angle due to the electric field described by $F(\delta,\alpha)$, and is given by:

$$P(\delta,\alpha) = |F(\delta,\alpha)|^2/Z_o \qquad 4.1.3$$

Z_o is the impedance of free space. It is useful to define a normalized power pattern, $P_n(\delta,\alpha)$, which is independent of the power radiated (or received) by the antenna. Assuming the peak power response of the antenna to be in a direction perpendicular to the antenna aperture the normalized pattern is defined by:

$$P_n(\delta,\alpha) = P(\delta,\alpha)/P(0,0) \qquad 4.1.4$$

By the auto-correlation theorem we may deduce that

$$P(\delta,\alpha) \Rightarrow ACF(E(-x/\lambda,y/\lambda))/Z_0 = P(0,0).A(-x/\lambda,y/\lambda) = P(0,0).A(u,v) \qquad 4.1.5$$

where a new function, $A(u,v)$, has been introduced for notational brevity. The extent of $A(-x/\lambda,y/\lambda)$ is finite and is twice that of the aperture illumination function, $E(x/\lambda,y/\lambda)$. Therefore the power pattern must be a bandlimited function of δ and α because $A(u,v)$ is the spatial spectrum of $P_n(\delta,\alpha)$.

A useful parameter of an antenna which may be deduced from its normalized power pattern is the beam solid angle, defined as:

$$\Omega_a = \iint_{4\pi} P_n(\delta,\alpha)\, d\Omega \qquad 4.1.6$$

$$\approx \iint_{4\pi} P_n(\delta,\alpha)\, d\alpha\, d\delta$$

$$= A(0,0)$$

assuming a sufficiently narrow beam. The beam solid angle is the equivalent width of the power pattern (cf. equation 3.3.4).

The power pattern of the Hartebeesthoek antenna was determined by mapping a point source (a source which has an angular extent much smaller than Ω_a). The results were not very good due to uncertainty in the levels of adjacent scans because of bad antenna tracking. In order to obtain some useful information from this data the pattern was assumed to be circularly symmetric. A one-dimensional cross-section of the normalized pattern was constructed by calculating weighted means of points falling within equal width annuli centered on the source. The weights depended on the radial position of the points within the annuli , i.e. unity at the centre, reducing linearly to zero at the edges. The resulting cross-section, which does not have uncertain levels, is shown by the crosses in figure 4.2(a).

Figure 4.2

(a) Cross-section of beam pattern.

(b) Cross-section of transform of beam pattern.

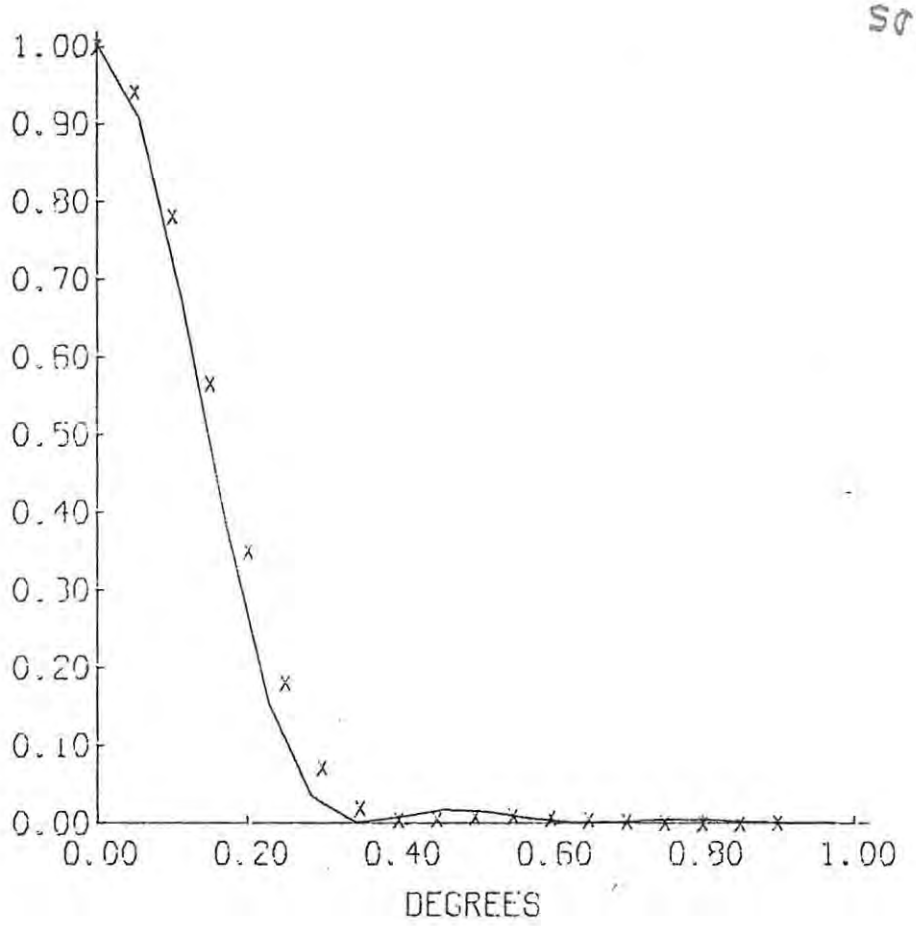
1.00
0.90
0.80
0.70
0.60
0.50
0.40
0.30
0.20
0.10
0.00
0.00
0.20
0.40
0.60
0.80
1.00
DEGREES

(a)

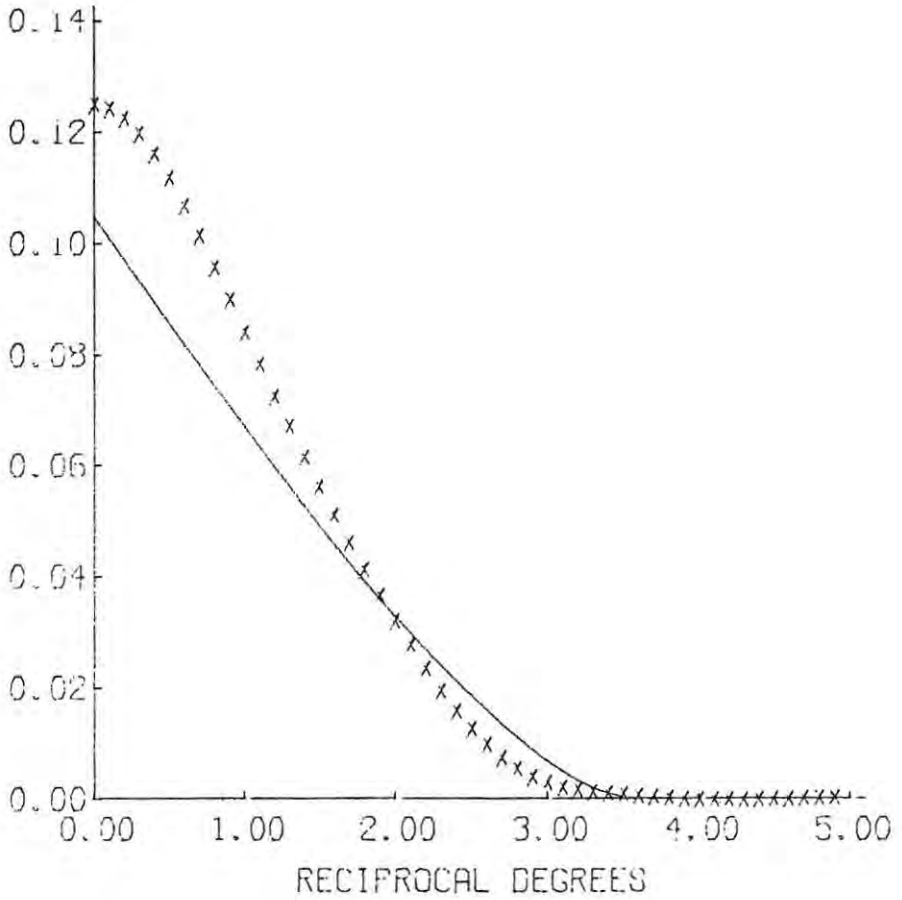
0.14
0.12
0.10
0.08
0.06
0.04
0.02
0.00
0.00
1.00
2.00
3.00
4.00
5.00
RECIPROCAL DEGREES

(b)

The solid curve is the cross-section that would have resulted if the antenna had a perfectly uniform aperture illumination. By performing a numeric Hankel transform (cf section 3.5) on these points the cross section of the transform of the main lobe of the beam was calculated and is illusterated in figure 4.2(b). Again the solid curve represents the result for uniform illumination. The main beam solid angle, Ω_M, is given by the value of this transform at the origin, i.e. Ω_M=0.125 square degrees (3.81×10^{-5} square radians). The beam solid angle is given by Ω_M/ϵ_M, where ϵ_M is the main beam efficiency.

At 13cm the 26m antenna is 200 wavelengths in diameter, which implies that $A(-x/\lambda, y/\lambda)$ may only extend to a radius of 200 in the $(x/\lambda, y/\lambda)$ plane. This implies that the maximum extent of the spectrum of the power pattern is 200 reciprocal radians, or 3.49 reciprocal degrees. Figure 4.2(b) shows that the measured cut-off point agrees well with the theoretical upper bound. The implication of this 'frequency cut-off' is discussed in section 4.1.4.

In order to get a better picture of the beam pattern, rather than its cross-section, a strong point source, RCW 5, was selected from a subsequent survey data set. This source is strong enough to show the first sidelobe of the power pattern. The Fourier transform of the antenna's response to this source is shown in figure 4.3(a). The bold circle has a radius of 3.5 reciprocal degrees, which is the theoretical limit of the angular spectrum. The spectrum of the power pattern only extends as far as these limits, the structure outside of the circle is due to high spatial frequency noise in the spatial domain data due to the receiver. The structure along the axes is due to 'edge effects', because the spatial data is not identically zero at the four edges. Figure 4.3(b) is the resulting beam pattern after the above spectrum was set to zero outside of the circle and reverse transformed. This Fourier filtering was performed using program FILT, described in the next chapter. There is evidence of the first sidelobe, outlined by contour

Figure 4.3

Contour plots of:

(a) transform of beam pattern, 3dB contour spacing, shaded between levels 1 and 2;

(b) filtered beam pattern, 2dB contour spacing, shaded between levels 5 and 4 (note increasing levels indicate increasing attenuation).

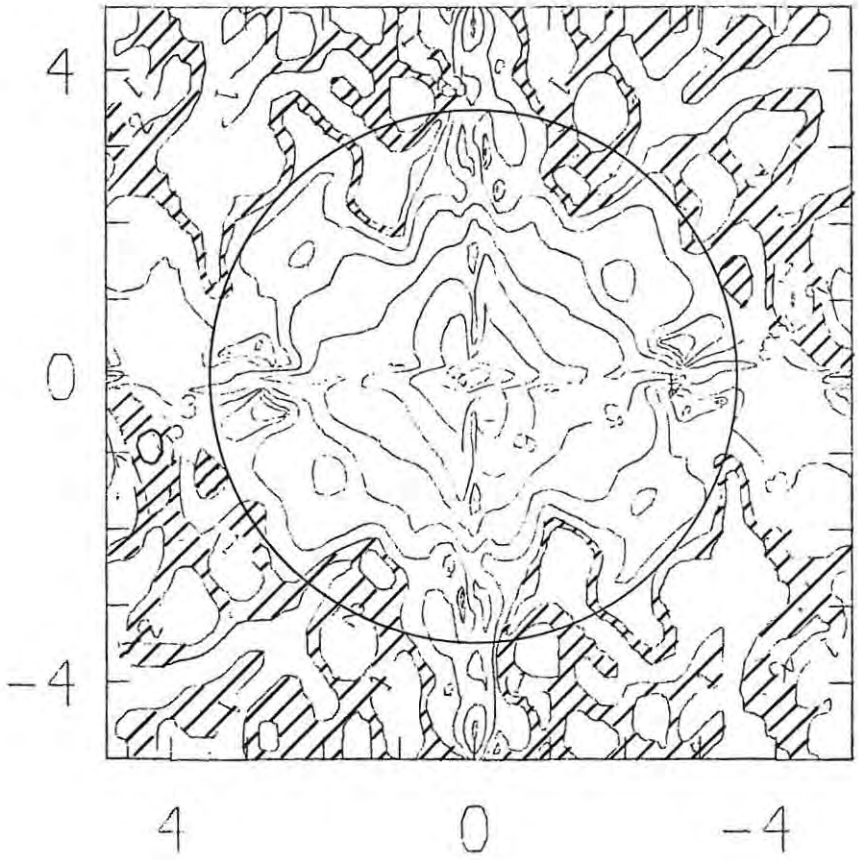

(a)

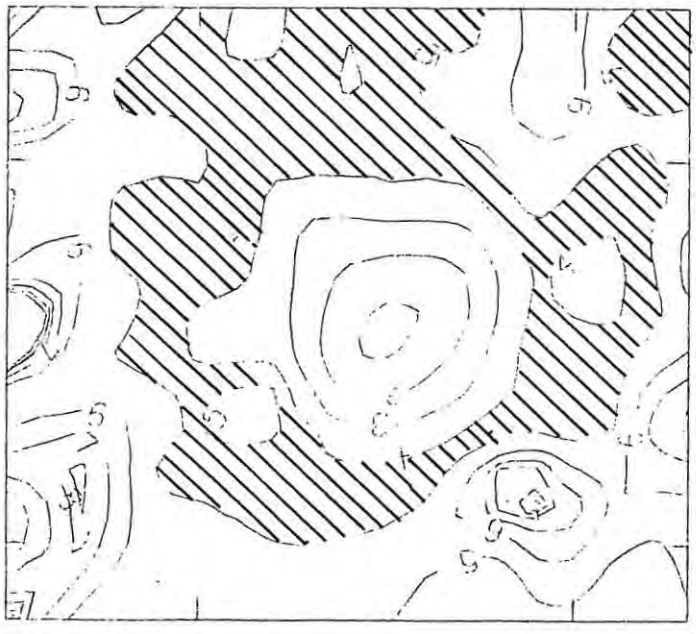

(b)

level 5. This sidelobe has an irregular appearance due to the nature of the aperture blockage by the subreflector support tetrapod.

4.1.3 The Effective Aperture

Because the aperture illumination function is not uniform in general, the effective aperture is smaller than the actual physical area of the antenna. The non-uniformity arises from the tapering of the illumination function, irregularities in the dish surface causing phase errors in the aperture plane, and aperture blockage. The effective aperture is defined to be the total power detected by the receiver divided by the total power density (integral of the Poynting vector) of the incident radiation at the aperture plane (Kraus and Carver 1973; Kraus 1966, P215), i.e.

$$A_e = \frac{R.\left|\iint E(x/\lambda, y/\lambda)\ dx\ dy\right|^2}{\left|E(x/\lambda, y/\lambda)\right|^2\ dx\ dy}$$

$$= \frac{\lambda^2 R.\iint E(x/\lambda, y/\lambda)\ dx/\lambda\ dy/\lambda \iint E^*(x/\lambda, y/\lambda)\ dx/\lambda\ dy/\lambda}{\iint E(x/\lambda, y/\lambda).E^*(x/\lambda, y/\lambda)\ dx/\lambda\ dy/\lambda} \qquad 4.1.7$$

The integrations are performed over the physical aperture of the antenna, A_p. R is a loss factor due to ohmic losses in the feed system.

The effective pattern aperture is defined to be the effective aperture neglecting ohmic losses, i.e. the effective aperture due to the illumination function shape and therefore the beam shape. The effective aperture and the effective pattern aperture are therefore simply related by:

$$A_e = R.A_{ep} \qquad 4.1.8$$

A_{ep} is proportional to the autocorrelation width of the aperture illumination function (cf. equation 3.3.5), and is thus related to the beam solid angle by the expression below (cf. equation 3.3.6):

$$A_{ep} \cdot \Omega_a = A_{ep} \cdot \Omega_M / \epsilon_M = \lambda^2 \qquad 4.1.9$$

This expression explains the reciprocal relationship between antenna size and beamwidth discussed at the begining of this section. The dependence on wavelength is also evident.

The effective pattern aperture of the Hartebeesthoek telescope at 13cm is:

$$A_{ep} = \frac{0.13^2 \epsilon_M}{3.81 \times 10^{-5}} = \epsilon_M 444 \text{ m}^2$$

The effective aperture may be calculated from observations of the increase in antenna temperature due to a radio source of known flux density, using the expression:

$$T_a = \frac{A_e}{2k} \iint B(\delta,\alpha) . P_n(\delta,\alpha) \, d\Omega \qquad 4.1.10$$

derived from equation 4.1.19. For a point source this simplifies to:

$$T_a = \frac{A_e}{2k} . (\text{flux of source})$$

Pictor A, which has a known 13cm flux of 41.8Jy, caused an increase in the antenna temperature of 4.77K. Using these figures the effective aperture is calculated to be:

$$A_e = 315 \text{ m}^2$$

which results in a loss factor of: $R = 0.71/\epsilon_M$

or: $R\epsilon_M = 0.71$

Comparing the effective aperture to the actual physical aperture of 531m^2, the aperture efficiency is calculated to be 59.5%.

4.1.4 Antenna Temperature

The celestial radio radiation is produced by a large number of discrete and extended sources with different radiation mechanisms and intensities. It is convenient to think of the combined radiation of these sources as coming from a celestial sphere with an appropriate intensity distribution. This intensity distribution is called the radio brightness distribution,

$$B(\delta,\alpha,\nu)$$

dependent on position angle and frequency. In radio astronomy the brightness temperature distribution is used in preference to the actual brightness distribution. This brightness temperature is related to the brightness distribution by

$$T_b(\delta,\alpha) = \frac{\lambda^2}{2k}.B(\delta,\alpha,\nu) \qquad 4.1.11$$

For a black body the brightness temperature would be its physical temperature, assuming the Raleigh-Jeans approximation for long wavelengths. Consider the infinitesimal receiving surface, dS_a, in figure 4.4. The power per unit bandwidth passing through this surface from the small area dS_s of the celestial sphere with brightness $B(\nu)$ is given by:

$$\begin{aligned} dW_a &= B(\nu).dS_s.d\Omega_a.\cos(N) \\ &= \frac{B(\nu).dS_s.dS_a.\cos(N)}{R^2} \\ &= B(\nu).d\Omega_s.dS_a.\cos(N) \end{aligned} \qquad 4.1.12$$

Again considering the geometry in figure 4.1, the total power received by the antenna from the cone of solid angle $d\Omega$ in the frequency bandwidth $d\nu$ is:

$$dW = A_e.B(\delta,\alpha,\nu).P_n(\delta,\alpha).H(\nu).\cos(N)\ d\nu\ d\Omega \qquad 4.1.13$$

where $d\Omega = \cos\delta\ d\alpha d\delta$.

Figure 4.4

Power passing through recieving area dS_a due to radiating surface dS_s.

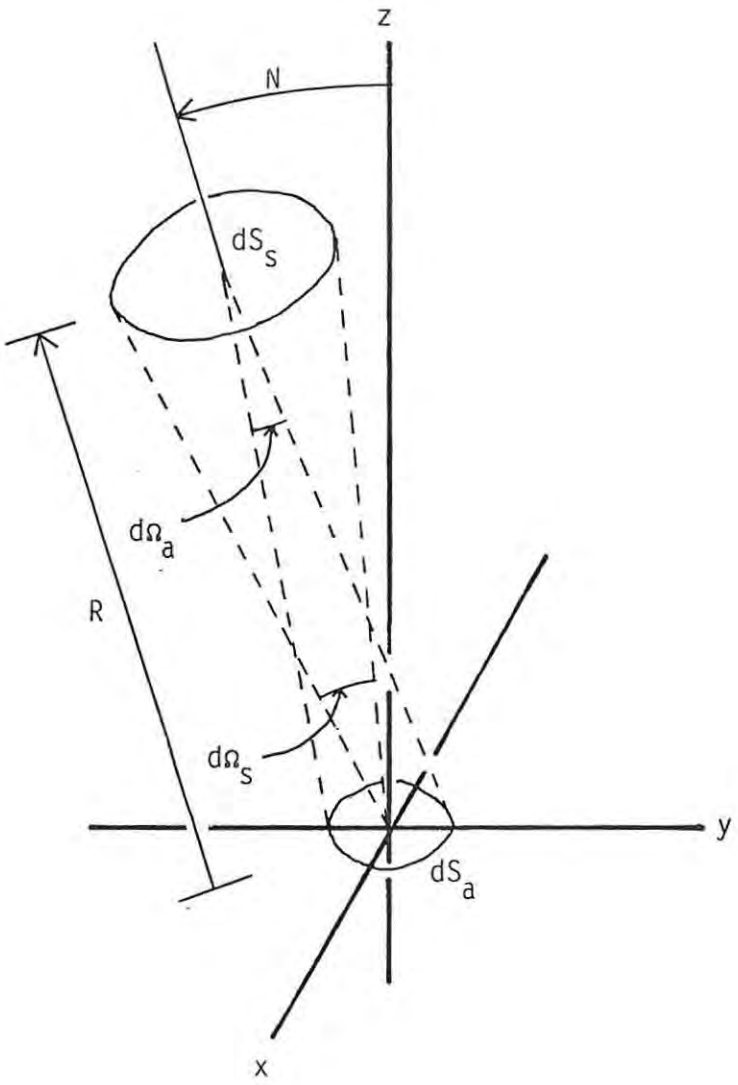
z
N
dS_s
$d\Omega_a$
R
$d\Omega_s$
y
dS_a
x

For a narrow beam antenna the cos(N) factor may be assumed to be unity. $H(\nu)$ is the power response of the receiver. Thus the power received by the antenna for one polarization, assuming random signal polarization, is:

$$W = \tfrac{1}{2}.A_e \iint_{4\pi} \int_{o}^{\infty} B(\delta,\alpha,\nu).P_n(\delta,\alpha).H(\nu)\, d\nu\, d\Omega \qquad 4.1.14$$

The E-vector polarization position angle for the 13cm feed of the Hartebeesthoek antenna is 90 degrees, i.e E-vector aligned east-west.

If the passband of the receiver is narrow compared to the operating frequency then the integrals may be separated and performed independently. The power pattern is independent of frequency over the passband, so the integration over the passband of the receiver reduces to

$$B'(\delta,\alpha) = \int_{o}^{\infty} B(\delta,\alpha,\nu).H(\nu)\, d\nu$$

$$= B_\nu(\delta,\alpha).H_N \qquad 4.1.15$$

where $B'(\delta,\alpha)$ is called the total brightness, $B_\nu(\delta,\alpha)$ is the average brightness over the passband and H_N is proportional to the noise equivalent bandwidth of the receiver.

Substituting this integral into equation 4.1.14 and dividing through by H_N to give a power independent of receiver bandwidth results in

$$w = \tfrac{1}{2}.A_e \iint_{4\pi} B_\nu(\delta,\alpha).P_n(\delta,\alpha).\cos\delta\, d\alpha\, d\delta \qquad 4.1.16$$

In radio astronomy this power per unit bandwidth is specified by the antenna temperature, T_a. The antenna temperature is defined to be the temperature to which a resistor must be heated so that it produces the same noise power as is received by the antenna. , i.e.

$$w = k.T_a \qquad 4.1.17$$

After some substitution the relationship between antenna temperature and brightness temperature may be derived for an antenna pointing towards

$(\delta=0,\alpha=0)$.

$$T_a = \frac{R}{\Omega_a} \iint_{4\pi} T_b(\delta,\alpha).P_n(\delta,\alpha).\cos\delta \, d\alpha \, d\delta \qquad 4.1.18$$

This equation may be simplified for two special cases. If the angular size of the source is much smaller than the beamwidth of the antenna, the normalized power pattern may be assumed to be unity over the source if the telescope is pointing directly at it. Assuming the brightness temperature to be constant accross the source equation 4.1.18 may be written:

$$T_a = \frac{R.T_b}{\Omega_a} \iint_{\text{source}} \cos\delta \, d\alpha \, d\delta$$

$$= \frac{R.\Omega_s.T_b}{\Omega_a} \qquad 4.1.19$$

Thus, knowing the angular extent of the source, the brightness temperature may be deduced from the antenna temperature.

If, on the other hand, the telescope is pointing at a uniform source larger than the beam of the telescope, equation 4.1.18 reduces to:

$$T_a = \frac{R.T_b}{\Omega_a} \iint_{4\pi} P_n(\delta,\alpha).\cos\delta \, d\alpha \, d\delta$$

$$= R.T_b \qquad 4.1.20$$

4.1.5 The Scanning Antenna

Equation 4.1.18 describes the antenna temperature when the telescope is pointing towards the origin of the equatorial co-ordinate system. For a telescope pointing towards an arbitary position, (δ_o,α_o), equation 4.1.18 generalizes to:

$$T_a(\delta_o,\alpha_o) = \frac{R}{\Omega_a} \iint_{4\pi} T_b(\delta,\alpha).P_n(\delta-\delta_o,(\alpha-\alpha_o).\cos\delta).\cos\delta \, d\alpha \, d\delta \qquad 4.1.21$$

The integral in this equation resembles the convolution integral, except for the two cosine factors. For a narrow beam these two factors may be assumed to be constant, i.e.

$$\cos\delta = \cos\delta_o$$

and equation 4.1.21 may be rewritten:

$$T_a(\delta_o,\alpha_o) = \frac{R}{\Omega_a}.T_b(\delta,\alpha) * P_n(-\delta,-\alpha.\cos\delta_o).\cos\delta_o \qquad 4.1.22$$

Since the Fourier transform of the normalized power pattern is known to have finite extent in the transform domain, the transform of $T_a(\delta,\alpha)$ must also have finite limits because of the properties of convolution and the similarity theorem (cf chapter 3). The brightness temperature, $T_b(\delta,\alpha)$, may have a wide spatial frequency bandwidth, but the antenna has a spatial frequency passband, analogous to an electronic filter, which modifies this spectrum. This passband is related to A(u,v). Transforming equation 4.1.22 yields:

$$t_a(u,v) = \frac{R}{\Omega_a}\, t_b(u,v) \;.\; A(u,v/\cos\delta_o) \qquad 4.1.23$$

It is evident that $t_a(u,v)$ shrinks along the v axis as declination increases. Because of this variance it is not strictly valid to use the Fourier theory, but it is a good estimate for narrow declination ranges. For wider declination ranges an upper bound may be placed on the extent of the spectrum of the antenna temperature. Because $A(u,v/\cos\delta_o)$ can never extend beyond 3.5 reciprocal degrees in the (u,v) plane, the spectrum of the antenna temperature must always be bandlimited to 3.5 reciprocal degrees.
The antenna temperature as a two-dimensional function of position angle is a smoothed and attenuated version of the brightness temperature distribution. The attenuation, which is due to the loss factor, can be compensated for,

but it is not possible to reconstruct the brightness distribution from the antenna temperature. No spatial frequency components outside of the passband of the antenna are present in the antenna temperature distribution. Recent signal processing techniques employing the Maximum Entropy Method attempt to estimate spectral components outside the spatial passband of the antenna (cf chapter 9).

Radio astronomy techniques often involve scanning processes which result in a one-dimensional cross-section of the two-dimensional antenna temperature function. The Fourier transform of the one-dimensional antenna temperature as a function of scan angle would be a one-dimensional frequency spectrum which may be deduced from the two-dimensional spectrum of the antenna temperature. Consider the case of a declination scan, $S_{\alpha_o}(\delta)$, at a constant right ascension, α_o. The scan is related to the two-dimensional antenna temperature function by the equation:

$$S_{\alpha_o}(\delta) = (T_a(\delta,\alpha) * \delta(\delta,\alpha+\alpha_o)).\delta(\alpha) \qquad 4.1.24$$

The convolution by the displaced delta function shifts the function T_a so that the desired scan lies along the α=0 axis, and the multiplication by the delta function removes the α dependence. The spectrum of $S_{\alpha_o}(\delta)$, $s_{\alpha_o}(u)$, is calculated by transforming equation 4.1.24 to yield:

$$\begin{aligned} s_{\alpha_o}(u) &= (t_a(u,v).\exp(+2i\pi\alpha_o v)) * \delta(u) \\ &= \int_{-\infty}^{\infty} t_a(u,v).\exp(+2i\pi\alpha_o v)\, dv \end{aligned} \qquad 4.1.25$$

From this equation it is clear that the extent of the spectrum of $S_{\alpha_o}(\delta)$ is the same as the maximum extent of $t_a(u,v)$ along the u-axis. The bandwidth is independent of the variation of $t_a(u,v)$ with v, which is intuitively correct. Therefore $S_{\alpha_o}(\delta)$ is bandlimited to 3.5 reciprocal degrees.

A quick proof of the relationship between the scan and the two dimensional

function is given below:

$$S_{\alpha_o}(\delta) = \int_{-\infty}^{\infty} s_{\alpha_o}(u).\exp(+2i\pi\,\delta u)\,du$$

$$= \int_{-\infty}^{\infty}\int_{-\infty}^{\infty} t_a(u,v).\exp(+2i\,\pi\,(\delta u+\alpha_o v))\,du\,dv$$

$$= T_a(\delta,\alpha_o)$$

4.2 The Radiometer and Data Capture

4.2.1 The Radiometer

The expression for the antenna temperature, $S_{\alpha_o}(\delta)$, in the previous section would be the output of an ideal noiseless receiver connected to the antenna. Let us call this the antenna signal. In practice the main component of the receiver output is due to the thermal noise of the receiver. Using the noise adding radiometer it is possible to balance out the average noise power, but random fluctuations of this noise are superimposed on the radiometer output. The r.m.s. amplitude of these fluctuations is given by equation 2.2.1. These fluctuations, dT_a, have a Gaussian amplitude distribution and have frequency components up to the bandwidth of the final stage of the radiometer.

Because our observing technique involves constant rate declination scans, the output of the radiometer may be thought of as a function of declination angle rather than time. This output may be expressed as:

$$R_{\alpha_o}(\delta) = S_{\alpha_o}(\delta) + dT_a(\delta) \qquad 4.2.1$$

$S_{\alpha_o}(\delta)$ is known to be a band-limited function of declination, but dT_a has a much wider bandwidth. A scan rate of 0.25 degrees/second was used, so the

spatial frequency bandwidth of the noise fluctuations is:

Bandwidth of radiometer(Hz)/0.25 reciprocal degrees

Figure 4.5(a) illustrates a possible radiometer output spectrum for the Hartebeesthoek telescope. The units of the horizontal scale are reciprocal radians and the vertical scale is an arbitrary power scale. The spatial frequency range -3.5 to 3.5 contains the antenna signal spectrum. The receiver noise spectrum extends along the entire axis.

4.2.2 The Integrating Digital Volt Meter

The integrating D.V.M. converts the analog signal from the radiometer into a sequence of digital samples to be read by the computer and written to magnetic tape. The integration time and sample period of the D.V.M. were both one tenth of a second, which corresponds to 0.025 degrees of declination for the scan rate used. The operation of the D.V.M. is described in Fourier notation by:

$$D_{\alpha_0}(\delta) = (R_{\alpha_0}(\delta) * \Pi(\delta/0.025)) \cdot III(\delta/0.025) \qquad 4.2.3$$

The convolution by the rectangular function corresponds to the integration, which is a continuous running mean (Bracewell p167). The multiplication by the shah represents the sampling of the integrated signal. Figure 4.5 illustrates graphically how the spectrum of the radiometer output signal is modified by the integration and sampling processes. The integration of the input signal corresponds to the multiplication of its spectrum (figure 4.5(a)) by a sinc function with its first nulls at 40 reciprocal degrees (figure 4.5(b)) resulting in the spectrum in figure 4.5(c). This does not affect the antenna signal's spectrum appreciably, but the higher frequency noise components are attenuated. The sidelobes of the sinc function allow a little high frequency noise leakage, so the integrated signal is not band limited (figure 4.5(c)). The sampling of the integrated signal results in

Figure 4.5

The effect of the D.V.M. on the spectrum of the radiometer output signal.

(a) The radiometer output spectrum.

(b) The passband due to the 0.1 second sampling interval.

(c) The product of (a) and (b).

(d) The replicating function due to the spatial domain sampling.

(e) The replicated spectrum of the D.V.M. output samples.

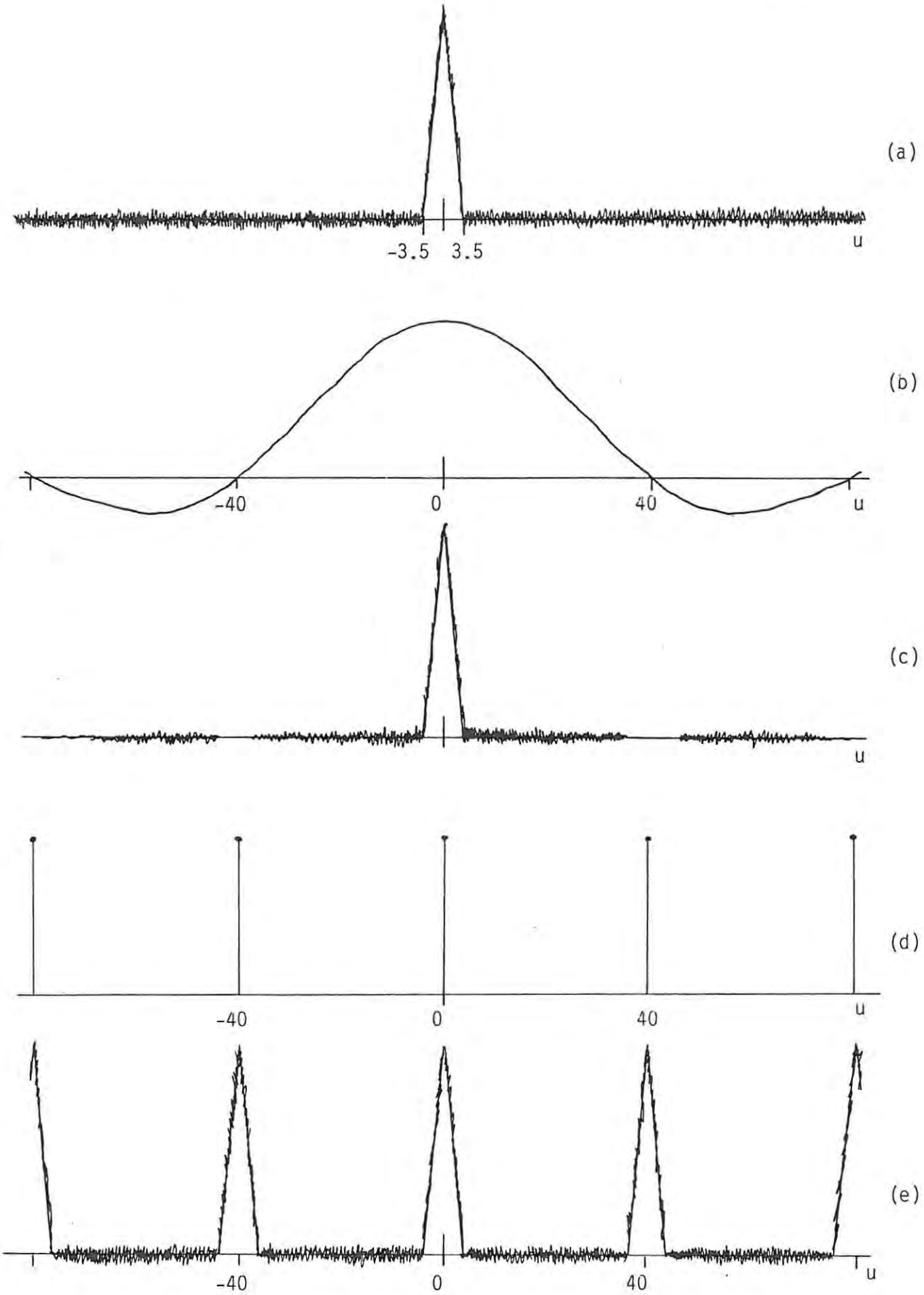
(a)
-3.5
3.5
u
(b)
-40
0
40
u
(c)
u
(d)
-40
0
40
u
(e)
-40
0
40
u

its spectrum being aliased. $s_{\alpha_o}(u)$ is sufficiently narrow not to be aliased onto itself, but the higher frequency noise components are aliased and superimpose on the antenna signal (figure 4.5(e)). The major component of this aliased noise comes from the main lobe of the sinc function.
Therefore the data samples written to magnetic tape represent samples of the antenna signal plus high spatial frequency noise.

4.3 The Initial Data Processing

Not all of the initial data processing affects the resolution or sensitivity of the data. The processes which remove the instrumental drift and terrestrial background are simple subtractions, and will not be discussed here. The declination binning and raster recombination processes are examined below.

4.3.1 Binning

The binning process is similar to the operation of the integrating D.V.M., except that it has sampled data as input, whereas the D.V.M. has a continuous signal. A declination bin size of 0.1 degrees was thought to be optimal, reducing the data set to a manageable size, but not causing aliasing of the spatial spectra of the scans.
The effect of binning on the spectrum of the sampled signal recorded on magnetic tape is illustrated diagrammatically in figure 4.6. Binning is basically the re-sampling of the data at wider intervals. The averaging of the samples over 0.1 degree intervals corresponds to multiplying the replicated spectrum of the sampled input data by a sinc function with first nulls at 10 reciprocal degrees (figure 4.6(b)). The sidelobes of this sinc function allow through higher frequencies, which include replicated versions of the required signal spectrum (figure 4.6(c)). The resampling, which

Figure 4.6

The effect of binning on the spectrum of the D.V.M. samples.

(a) The spectrum of the D.V.M. samples

(b) The sinc function corresponding to the averaging of the samples

(c) The product of (a) and (b)

(d) The replicating shah function due to the resampling of the binned values

(e) The spectrum of the binned samples

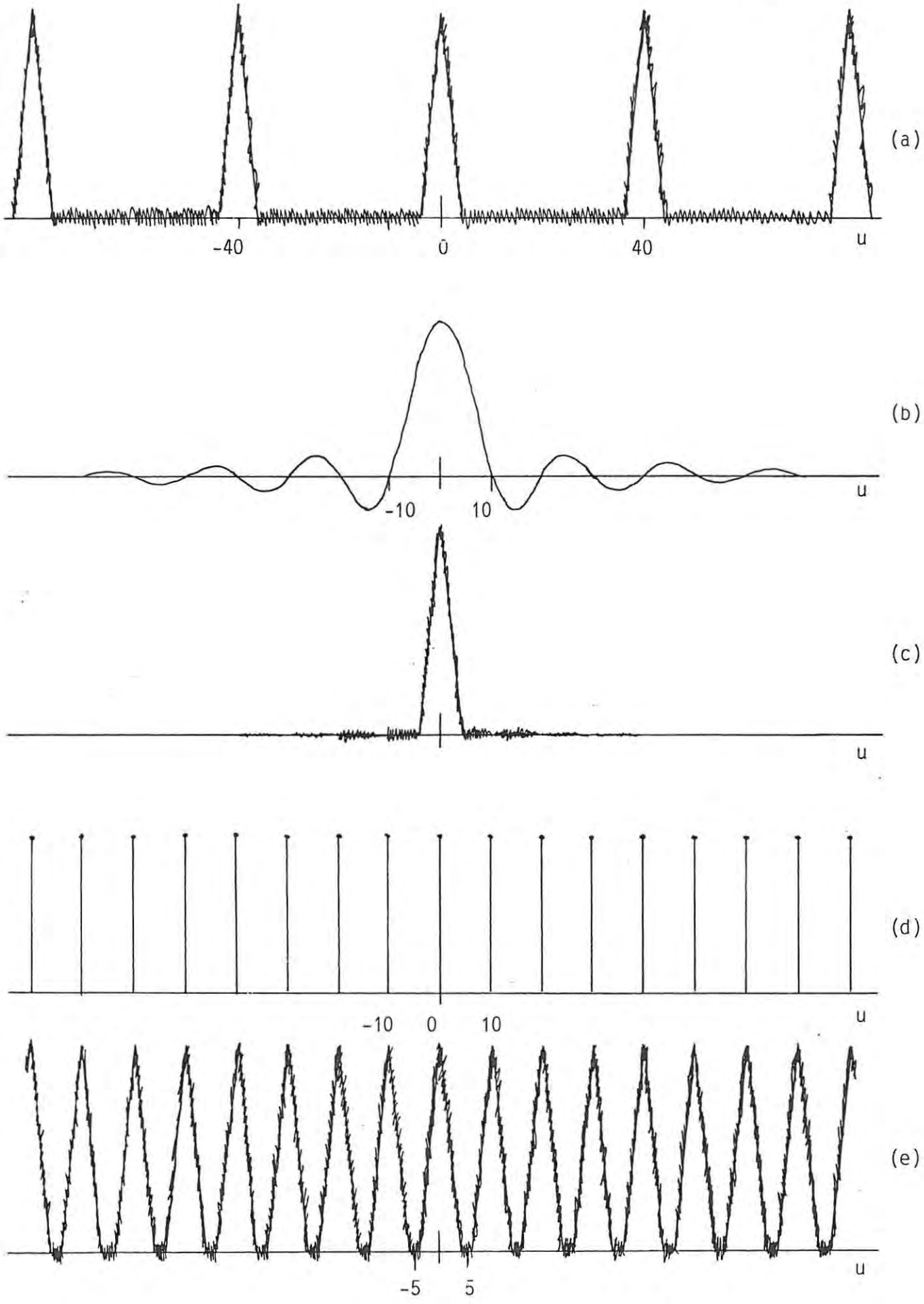
(a)
-40
0
40
u
(b)
-10
10
u
(c)
u
(d)
-10
0
10
u
(e)
-5
5
u

corresponds to the convolution by a shah function with a spacing of 10 reciprocal degrees in the frequency domain (figure 4.6(d)), causes these leaked components to alias on to the original spectrum (together with aliased noise). This leakage is minimal because the replications coincide with the nulls of the sinc function. The main lobe of the sinc function has some smoothing effect on the data since the sinc function drops to 0.81 at 3.5 reciprocal degrees.

The theoretical r.m.s. noise on the data at this stage of the processing may be calculated. Each sample is the result of 0.4 seconds of signal integration (0.1 degrees/0.25 degrees per second). Thus the r.m.s. noise is

$$dT_a = 15.(1.0/0.4)^{1/2}$$
$$= 24 \text{ mK}$$

using the r.m.s. noise deviation for a one second integration time constant calculated in section 2.2.

The binned data represent samples of slightly smoothed cross-sections of the antenna temperature function. The high spatial frequency noise level has been reduced by the multiplication of the spectrum by a sinc function (figure 4.6(b)). The sampling period is still sufficiently short so that no aliasing of the antenna signal's spectrum occurs. The reduction of the high spatial frequency noise is discussed in the next chapter.

4.3.2 Raster Recombination

In the raster recombinaton process the sampled scans are sorted into the correct order and laid out next to one another to construct a matrix of values. If we assume that the antenna tracked perfectly and that all of the data for each of the three repeats of each raster are good, then on combining these rasters the r.m.s. noise level for each sample will be:

$$dT_a = 24/3^{1/2} = 14 \text{ mK}$$

This is an optimistic figure, because if there is any bad data or the antenna tracking error is larger than a scan spacing, only samples from one or two repeats will be used to derive the combined scans.

Let these combined scans be denoted by:

$$C_{\alpha_0}(k\Delta\delta) \qquad \Delta\delta = 0.1 \text{ deg}$$

The reconstruction of the sampled map from these scans may be described mathematically by

$$M(k\Delta\delta, l\Delta\alpha) = \sum_{l} C_{\alpha_0}(k\Delta\delta) * \delta(\delta, \alpha - \alpha_0) \qquad \alpha_0 = l\Delta\alpha \qquad 4.3.1$$

The limits of k and l depend on the bounds of the map. This reconstruction re-introduces the right-ascension dependence removed in the scanning process. Transforming equation 4.3.1 yields:

$$m(u,v) = \sum_{l} c_{\alpha_0}(u).\exp(-2i\pi v l\Delta\alpha) \qquad 4.3.2$$

which is periodic in two dimensions, as expected for the spectrum of a sampled two-dimensional function.

The matrix of values making up the map corresponds very closely to samples of the antenna temperature function because the combined scans are good approximations to cross-sections of this function. Therefore the spatial spectrum given by equation 4.3.2 is a good approximation to a replicated version of the spectrum of the antenna temperature. This replication does not introduce any aliasing of the wanted signal's spectrum because the spatial sampling period is short enough. Therefore the D.F.T. of the matrix of samples making up the map is a good approximation to the spectrum of the antenna temperature plus noise.

This chapter has related the raw map data to the radio brightness distribution function. It has been shown that the brightness distribution cannot be reconstructed exactly because high spatial frequency components

have been lost. The data samples making up the raw map are samples of the antenna temperature function plus random noise fluctuations. The next chapter describes digital enhancement and analysis procedures and the computer programs written to implement them. These processes make use of the properties and relationships derived in this chapter.

CHAPTER 5 DATA PROCESSING AND DISPLAY

Before the raw data can be analyzed effectively it is necessary to perform some sort of signal conditioning on the data. The type of conditioning depends on the analysis, but would generally involve some form of enhancement. Such processes are described in this chapter.

The previous chapter determined the spectrum of the sampled map data. Knowing the properties of this spectrum the signal to noise ratio of the data may be improved by Fourier or convolution filtering. Geometric distortion introduced into the data by projecting the equatorial coordinate system onto a flat plane must be reduced for the filtering to work properly. This may be done by transforming the data onto another coordinate grid. This chapter discusses the implementation of computer programs which perform these operations.

The emission from our Galaxy causes a large brightness gradient accross the map. Low brightness features superimposed on this gradient are not easily detected. A method for subtracting the large scale Galactic emission from the data is discussed in section 5.4. Section 5.5 describes a program which measures the flux density of discrete radio sources which occur in the map.

Data display is perhaps the singularly most important aspect of Radio Astronomy data handling. No analysis is possible without a 'picture' of what is being studied. Various display methods which have been developed are described. Finally, the local implementation of the FITS image transport system is described in section 5.7.

5.1 Coordinate Transformation

There are various reasons for wanting to transform map data from one spherical polar coordinate system to another. The most common use of the coordinate transformation is to reduce the cosine distortion introduced into the data at higher declinations by representing it as a flat plane. This distortion is reduced by transforming the data onto a regular coordinate grid whose equator passes through the data (field centred projection). A more realistic representation of the spatial relationships between objects is obtained on the resulting map. This distortion affects the beam shape across the map, i.e. the response of the antenna to a point source (equation 4.1.22). Thus the extent of the two-dimensional spectrum of the data varies with declination (equation 4.1.23). This make it difficult to filter the data effectively. The distortion is reduced for the field centred data, and thus the data may be filtered more effectively. If required, the data may be transformed back to the original coordinate system.

Since precession is actually a spherical coordinate transformation, data which is on a grid of one epoch may be transformed to another epoch date. Another use of the coordinate transformation is the transformation of data between frequently used astronomical coordinate systems for comparing the data with other results. A common transformation would be the transformation from Equatorial to Galactic coordinates.

A description of the method used to perform the coordinate transformation follows, and then the actual implementation is discussed. Figure 5.1 illustrates the mechanism involved in coordinate transformation. Consider the original data samples to be at the crossing points of the rectangular grid. The coordinate transformation must produce samples at the

Figure 5.1

Lines of longitude and latitude of the new coordinate system superimposed on the original coordinate grid.

Figure 5.2

Cross-section of the Fourier transform of a unit volume cone function with a base radius of 0.1^{o}.

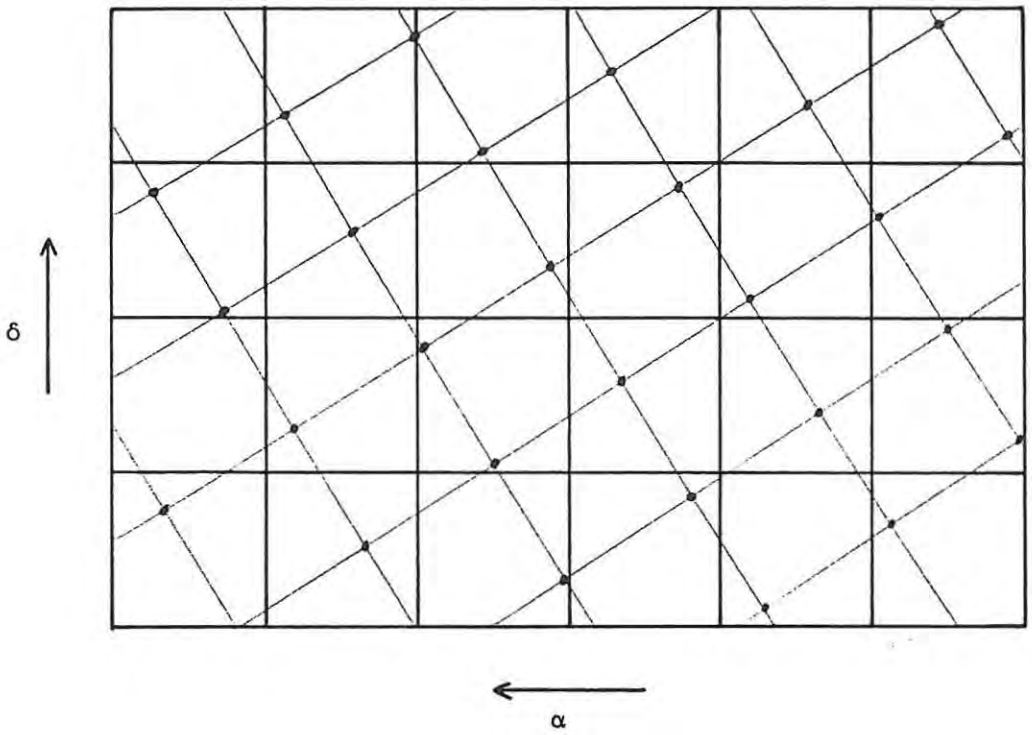
δ
α

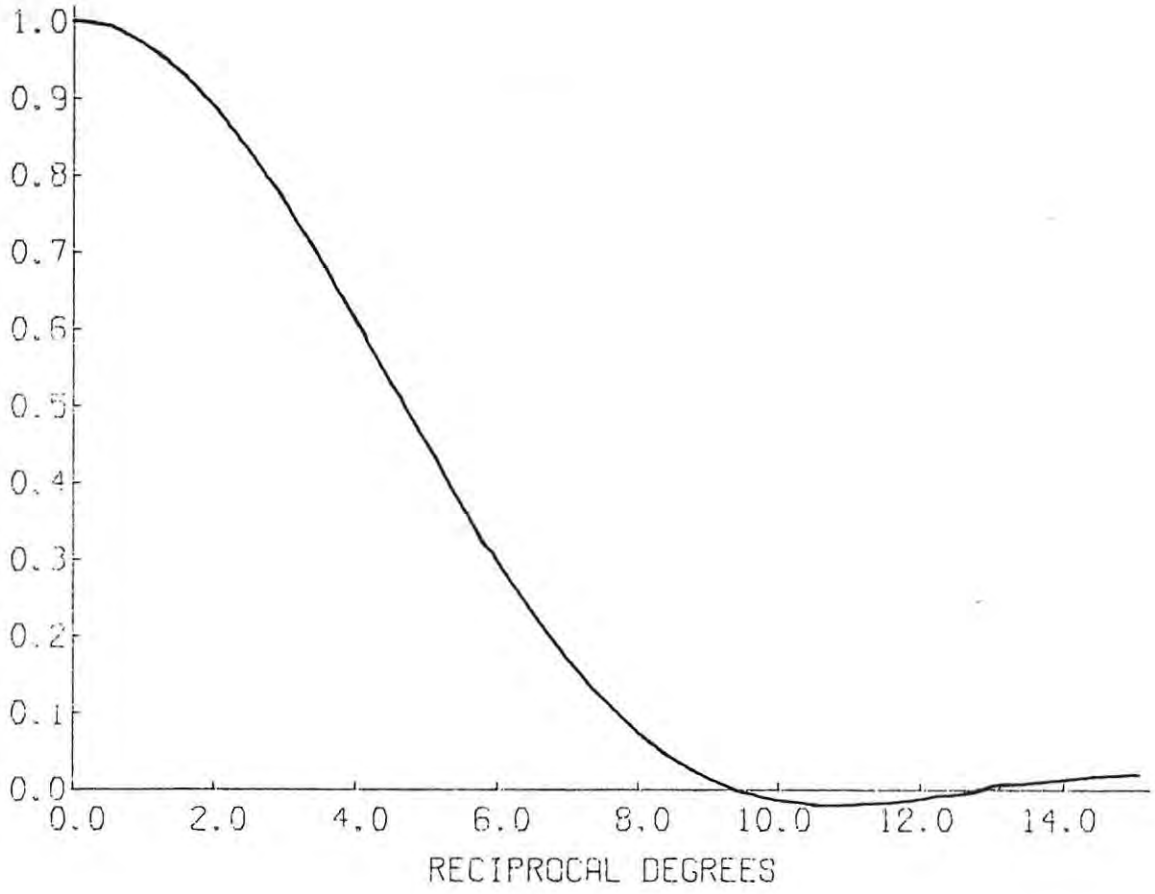
1.0
0.9
0.8
0.7
0.6
0.5
0.4
0.3
0.2
0.1
0.0
0.0
2.0
4.0
6.0
8.0
10.0
12.0
14.0
RECIPROCAL DEGREES

intersection points of the new grid, which is represented by the diagonal lines in the figure. These lines, which represent lines of longitude and latitude of the new coordinate system, are spaced at regular intervals and are curved in general. An interpolation procedure is needed to calculate the values of these new samples from the surrounding original samples. The interpolation takes into account the spectrum of the data, so that the resolution is not degraded.

This interpolation is best understood using Fourier transform theory. Interpolation is essentially the opposite process to sampling. Sampling produces values of a continuous function at discrete points, while interpolation reconstructs a continuous function given discrete samples. The sampling theorem states that if a bandlimited function is sampled often enough, it may be reconstructed exactly from the samples. In our case we know that our data is band-limited prior to sampling, except for the noise fluctuations, and that our sampling rate is adequate. Sampling of the original spatial function leads to the replication of its spectrum. Thus in order to reconstruct the original function it is necessary to single out the unreplicated spectrum. Mathematically this corresponds to multiplying the replicated spectrum by a function which is unity over the central component of the replicated spectrum and zero elsewhere, i.e. a rectangular function. This corresponds to the convolution of the sampled spatial function by an appropriate sinc function (or Bessel function in two dimensions). It is very impractical to use such functions as 'interpolation functions' since they would require a large number of samples because of their large extent. Samples of the interpolation function need to be recalculated for every interpolated sample. The computation of these samples and the numerical convolution would prove to be excessively time consuming.

A two-dimensional cone was implemented as a compromise interpolation

function, being easily calculated, finite in extent and having a Fourier transform which has the correct characteristics. The transform of a two-dimensional cone with a base radius of 0.1 degrees and unit volume is shown in figure 5.2. This is obviously not an ideal frequency domain function, since it allows leakage of the replicated spectra, and it also attenuates the central spectrum. At 3.5 reciprocal degrees, the cut-off frequency of the spectrum of the antenna temperature, the attenuation is about 0.7, which leads to a slight degradation of the resolution of the transformed map. Actual results have shown that the leakage does not have any noticeable effect.

Since the limit of the spatial frequency spectrum of the data is dependent on declination, the extent of the spatial spectrum of the interpolating function must vary accordingly. In general the base of the interpolating cone is an ellipse as illustrated in figure 5.3(a). The corresponding extent (position of first null) of the spatial spectrum of the interpolating function may be deduced using the similarity theorem, and is shown in figure 5.3(b).

This function narrows along the u-axis for higher latitudes, and therefore 'filters out' more high spatial frequency noise. The interpolating function has a larger base area for higher latitudes, and therefore uses more samples to calculate the interpolated value. This filtering does not affect the resolution of the data because the spectrum of the antenna temperature narrows in a similar way (equation 4.1.23).

A FORTRAN program, CTFM, was written to implement this transformation. Ideally the entire data set should reside in the physical memory of the computer to allow fast random access. Unfortunately the limitations of our present I.C.L. computer made this impossible for most data sets. The input

Figure 5.3

(a) The base of the interpolating cone function at a declination δ_o.

(b) The first null of the transform of the interpolation function in the (u,v) plane.

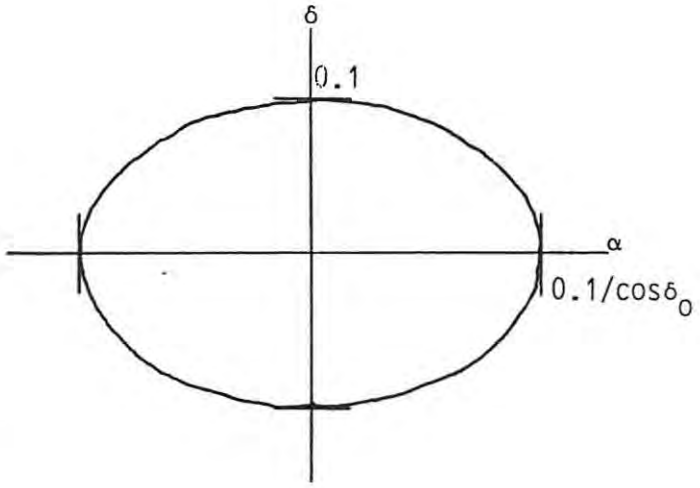

(a)

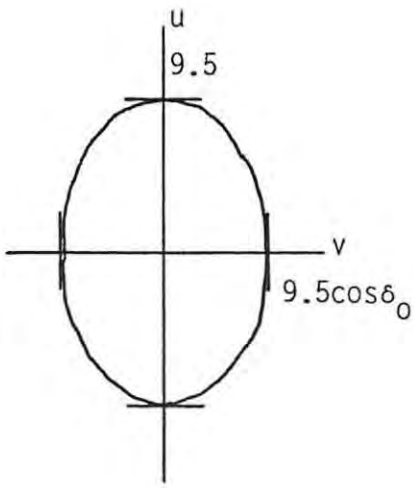

(b)

data are read in segments and these segments are transformed and written out. Another FORTRAN program, COMB, was written to combine the transformed segments and to pad with zeroes the areas where there is no data.

5.2 Filtering

The two dimensional antenna function is known to be band limited (equation 4.1.23), but the samples of the map have high spatial frequency noise superimposed on them. It would seem reasonable that the signal to noise ratio of the data could be enhanced by removing components of the spatial frequency spectrum which have higher frequencies than the known upper limit of the antenna temperature spectrum. Two such procedures are described here. One employs multiplication by a band-pass function in the Fourier transform domain, while the other relies on a convolution in the spatial domain. Ideally the Fourier filtering technique would always be used because it does not degrade the resolution of the data, but unfortunately this is impractical for very large data sets on the present computer because of the limited main memory size. For this reason the convolution filter was devised. The two methods handle the problem of edge effects in different ways, which are described in the relevent sections below.

5.2.1 Fourier Filtering

In order to understand the Fourier filtering technique it is necessary to go back to the radiometer output and consider it as a function of δ and α. This function has two components, the antenna temperature which is known to be bandlimited, and the noise component which has a larger bandwidth. The principle of Fourier filtering is to transform the noisy data, set all the components of the spectrum outside of the limits of the spectrum of the antenna temperature to zero, and inverse transform this spectrum to obtain

Figure 5.4

Fourier filtering of a discrete function:

(a) Noisy, discrete spatial function and its transform

(b) Interpolated spatial function and its truncated discrete spectrum

(c) Spatial frequency filter response function (right) and its corresponding spatial transform

(d) Filtered, continuous function

(e) Resampled, filtered function and its spectrum.

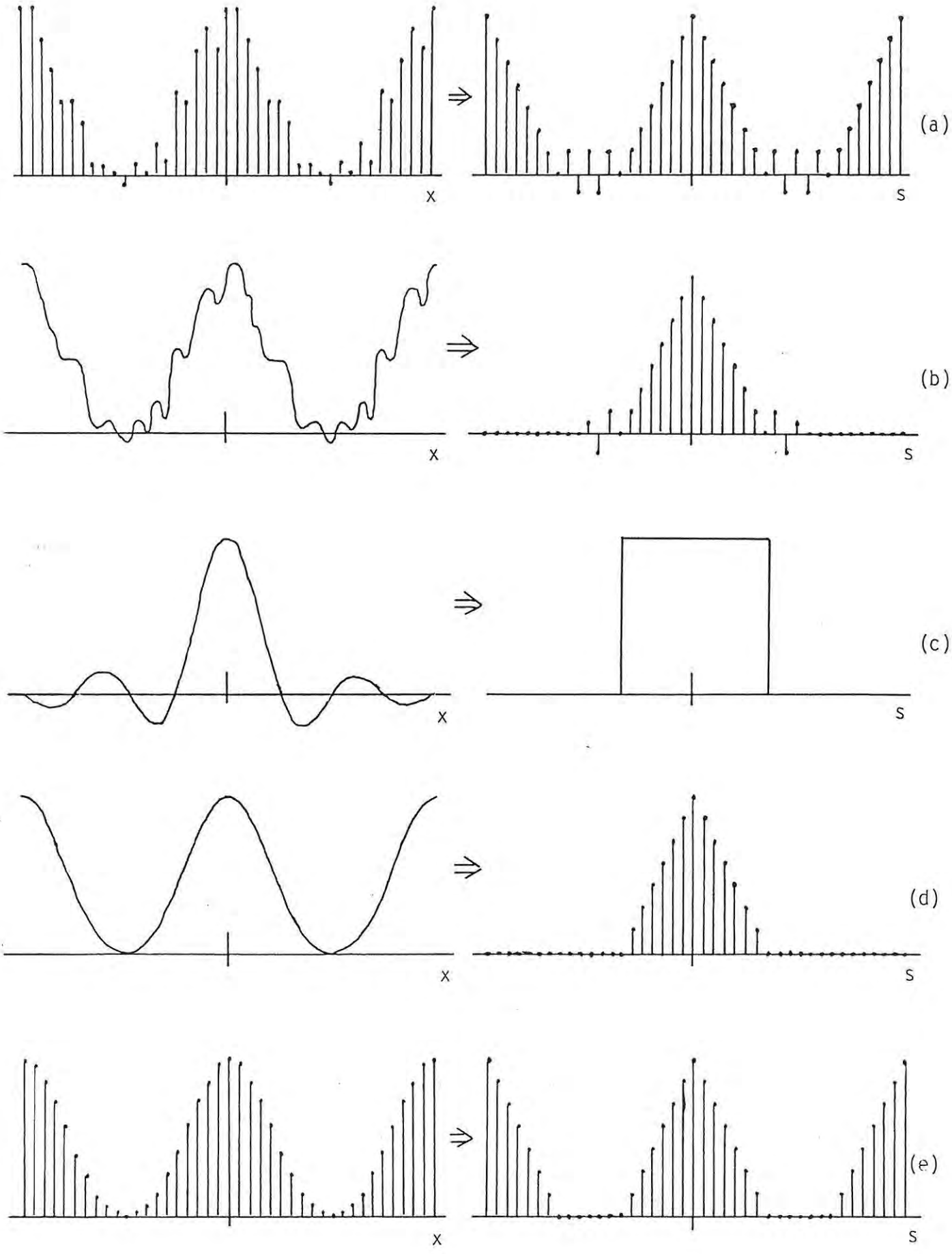
x
s
(a)
x
s
(b)
x
s
(c)
x
s
(d)
x
s
(e)

the filtered data. The removal of the high frequency noise components increases the signal to noise ratio of the data, but does not degrade the resolution since the spectrum of the antenna temperature is not affected at all.

The filtering of samples of this data employs the D.F.T. rather than the continuous Fourier transform. The resulting data should be samples of the continuous filtered data. It is convenient to think of the filtering of the discrete samples to have three phases; interpolation to regain the continuous distribution, removal of high frequencies, and resampling. The interpolation and resampling are not performed explicitly, but are useful devices for explaining the process. A typical replicated and sampled function and its hypothetical spectrum are shown in figure 5.4(a). The interpolation of the spatial data, which reconstructs the original continuous data, corresponds to the isolation of the original unreplicated spectrum (figure 5.4(b)). The resulting spectrum is then multiplied by the required passband function (figure 5.4(c)) to remove the unwanted high frequency components. The resampling is illustrated in figure 5.4(d) as the replication of the spatial frequency spectrum. This filtering process uses the D.F.T. to obtain the spectrum of the sampled data. This is valid because the data is very nearly band-limited (cf chapter 4).

The D.F.T. of the sequence of samples of the original data produces samples of one replica of the spectrum, as illustrated by figure 5.4(b). Note that there has been no explicit interpolation. This spectrum is then multiplied by the required passband. The resulting sequence is subjected to a reverse D.F.T. to produce samples of the filtered data. Note again that there has been no explicit resampling.

Unfortunately there is a problem if the data is truncated, the so called edge effect. This occurs when the entire data set is not available. When

doing large sky surveys, sections of the sky are observed and combined later. The data for each individual section is incomplete. In the description above the unsampled replicated spatial function was continuous and band limited, because of the nature of the data. Consider the continuous replicated function in figure 5.5(a). If a subset of the original continuous data is taken and replicated, the replicated function may have large discontinuities at the places where the replicated versions join. This is illustrated in figure 5.5(b) (cf. section 3.6, truncated functions). This function is clearly not band limited. Fourier filtering becomes invalid because it would remove high frequencies introduced into the data by the truncation. These high frequency components are required to reconstruct the 'sharp edge' introduced into the data. If these components are removed the edges 'ring', an effect similar to the Gibb's phenomenon. Although it is impossible to remove this effect entirely, it may be reduced. It may, in fact, not occur if the data is truncated in a position which does not cause a discontinuity in the replicated function. The method used to reduce the effect employs a 'guard band' around the two dimensional data. This is illustrated for the one dimensional case in figure 5.5(c). The truncated data is extended with a linearly interpolated straight line so that the discontinuity in the replicated data is reduced and very nearly band limited to the limits of the original data. The edge ringing is reduced to a negligible amount. It may be reduced further by using a tapered filter function, but such functions degrade the resolution of the data.

Other passband functions may be used to filter the data for reasons other than noise reduction. High pass filters may be applied to examine the high spatial frequency noise components, or to attenuate features with large

Figure 5.5

Illustration of the interpolation of a guard band to reduce the discontinuity of a replicated, truncated function.

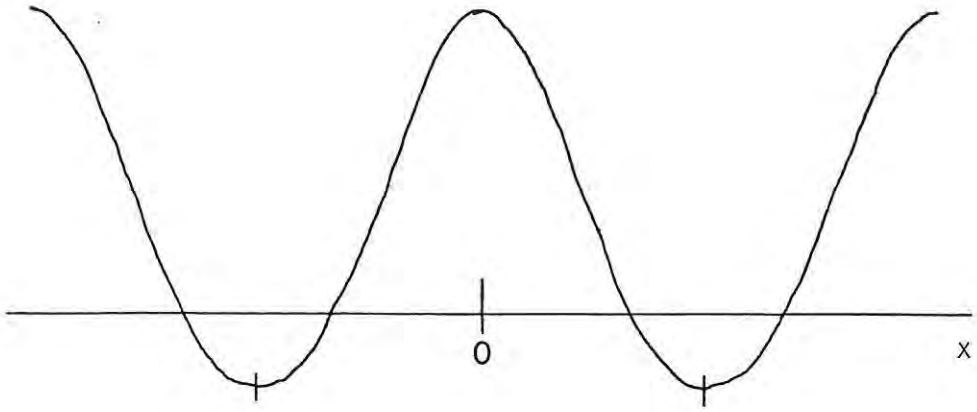

(a)

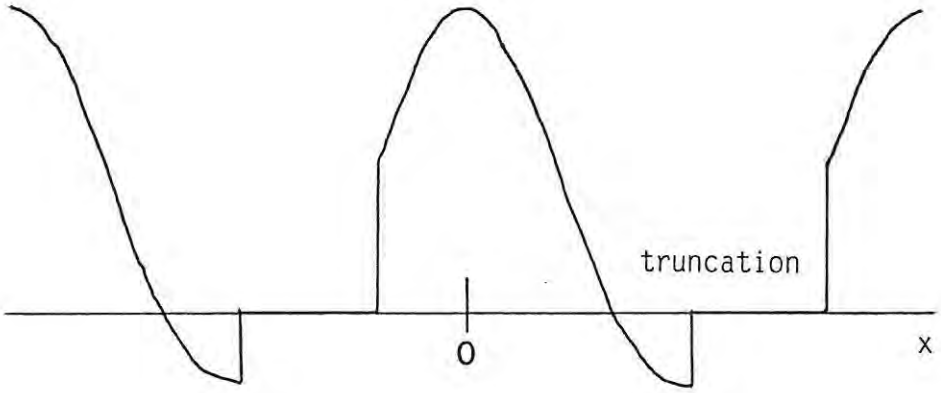

(b)

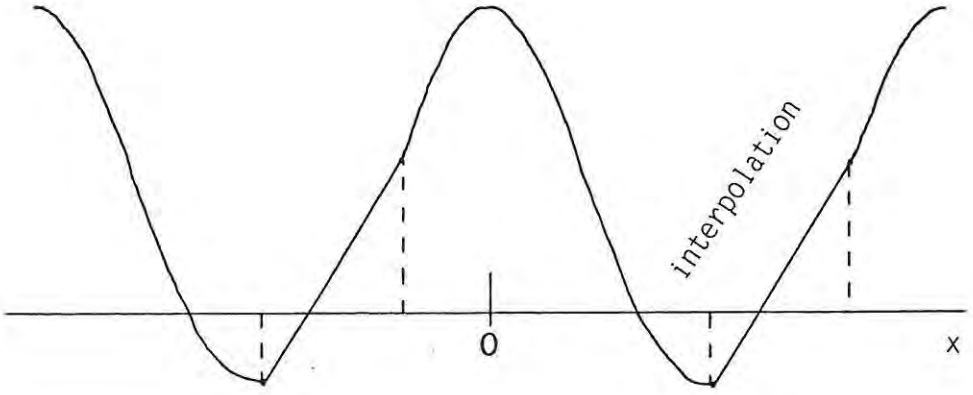

(c)

spatial extent in order to accentuate point sources. The data may be filtered in order to degrade the resolution of the map so it may be compared with data which has a lower resolution. A Gaussian bandpass profile would usually be used for this purpose.

Implementation

In order to implement the Fourier filtering procedure a number of routines were written to compute one and two dimensional D.F.T.'s as efficiently as possible. These routines are discussed individually below. The description of the actual filter program follows these.

PFFT

This routine, written in conjunction with P. Mountfort, performs the plus or minus-i D.F.T. on a complex array of data, using a base-2 F.F.T. algorithm. It was written in PLAN, the machine language of the I.C.L. computer, for greatest efficiency. Since the two dimensional D.F.T. requires a large number of successive one dimensional D.F.T.'s of the same length, the efficiency of the routine was further increased by storing pre-calculated weights in a look-up array. Another look-up array is used to 'unscramble' the F.F.T. (Brigham 1974, p159). A lot of effort was put into making the code for the inner loops as 'tight' as possible to increase the efficiency. Memory reference instructions were kept to a minimum. The resulting routine is four times faster than the equivalent FORTRAN routine. An equivalent FORTRAN routine was written in order to make the programs transportable, if necessary.

UNSCR and SCRAM

The efficient computation of the D.F.T of real sequences was discussed in section 3.7. Subroutine SCRAM implements the second of the methods

described there. The implementation is very efficient because of the way FORTRAN stores complex numbers. An array of N real elements may be considered to be equivalent to an array of N/2 complex elements, the odd elements being the real components and the even elements being the imaginary components. Therefore the D.F.T. of an N element real array may be calculated by presenting it as an N/2 element complex array to PFFT and unscrambling the resulting array using UNSCR. Only N/2+1 complex elements of the D.F.T. are returned, but this is sufficient since the D.F.T is Hermitian.

This routine is also written in PLAN for optimal speed. The unscrambling requires harmonic weights in addition to those used by PFFT, and these are stored in a lookup table to reduce computation.

Subroutine SCRAM performs the opposite operation to UNSCR. Given N/2+1 complex elements of an N-point real sequence, it produces a sequence that results in the real sequence when inverse transformed. The routine is implemented in a similar way to UNSCR, also using a look-up table for weights and written in PLAN.

These two routines are used in conjunction with PFFT to perform very efficient D.F.T.'s on real sequences and inverse D.F.T.'s on Hermitian sequences. Equivalent FORTRAN routines were also written for transportability.

SETUP

This FORTRAN routine sets up the look-up tables for PFFT, and UNSCR and SCRAM if required. Once this routine is called it need not be called again until the direction or length of the D.F.T. is changed. It was not thought necessary to code this routine in machine language because it is only called twice for a two dimensional D.F.T.

RTC2 and CTR2

The FORTRAN routine RTC2 performs a two-dimensional D.F.T. on an array of real data, returning half the Hermitian transform. As discussed in section 3.6, the two dimensional D.F.T. is implemented using one dimensional D.F.T.'s, and therefore the routine calls the routines already discussed. Firstly, the columns of the array are transformed, using PFFT and UNSCR. The columns are transformed first because of the way arrays are stored in FORTRAN. The rows of the resulting complex array are then transformed using PFFT.

CTR2 implements the inverse D.F.T. of Hermitian data. Given an array of half the Hermitian data (eg. the array returned by RTC2), it performs a complex inverse D.F.T. on the rows first, using PFFT. Routines SCRAM and PFFT are then used to perform inverse D.F.T.'s on the columns of the resulting complex array to produce a real array.

Program FILT

The Fourier filtering process was implemented by this FORTRAN program, which employs the routines described above. The size of the data array to be filtered is limited by the size of the main memory allocated to the program, but it need not have dimensions which are integral powers of two. The required section of data is read from the input data file into an array. The array has dimensions which are integral powers of two, and elements which do not contain data are interpolated to form the guard band described earlier. Subroutine RTC2 is called to perform a power of two D.F.T. on this data with the guard band. The resulting D.F.T. is subjected to a filter which eliminated frequency components outside of the known limits of the antenna temperature spectrum, taking into account the cosine factor for optimal filtering. The inverse D.F.T. is performed by subroutine CTR2 and

the resulting filtered array is written to the output file without the guard band. The original and filtered spectra may also be written to an output file if required.

5.2.2 Convolution Filtering

The Fourier filter described in the last section would correspond to the convolution of the spatial data by a two-dimensional function with a Bessel cross-section. Since this function has infinite extent it would be impractical to use it as a convolution filter. A convolution filter was designed so that data sets of any size could be filtered. Only part of the data has to be brought into the main memory of the computer at one time. This means that the convolution function must have a limited extent.

The convolution filter has a similar effect to the Fourier filter, as would be expected, but the band-pass function is different. A two-dimensional Gaussian convolution function is a good compromise, being easy to calculate and having an analytic transform, which is also a two-dimensional Gaussian. A convolution Gaussian with a half-width of 0.2 degrees degrades the resolution of the original data from 0.34 degrees to 0.4 degrees. The cross-sections of this Gaussian and its transform are shown in figure 5.6. The transform, which describes the pass-band of the filter, obviously attenuates spatial frequency components below 3.5 reciprocal degrees, which causes the resolution degradation. Figure 5.7 (crosses) illustrates the degradation of the resolution. This is the result of the convolution of the profile in figure 4.2(a) with the above Gaussian. The solid line is the response of an antenna with a uniform aperture illumination to a point source (cf figure 4.2(a)).

Although the convolving function is essentially band limited it does not

Figure 5.6

(a) Cross section of Gaussian spatial convolving function.

(b) Cross-section of Fourier transform of above function.

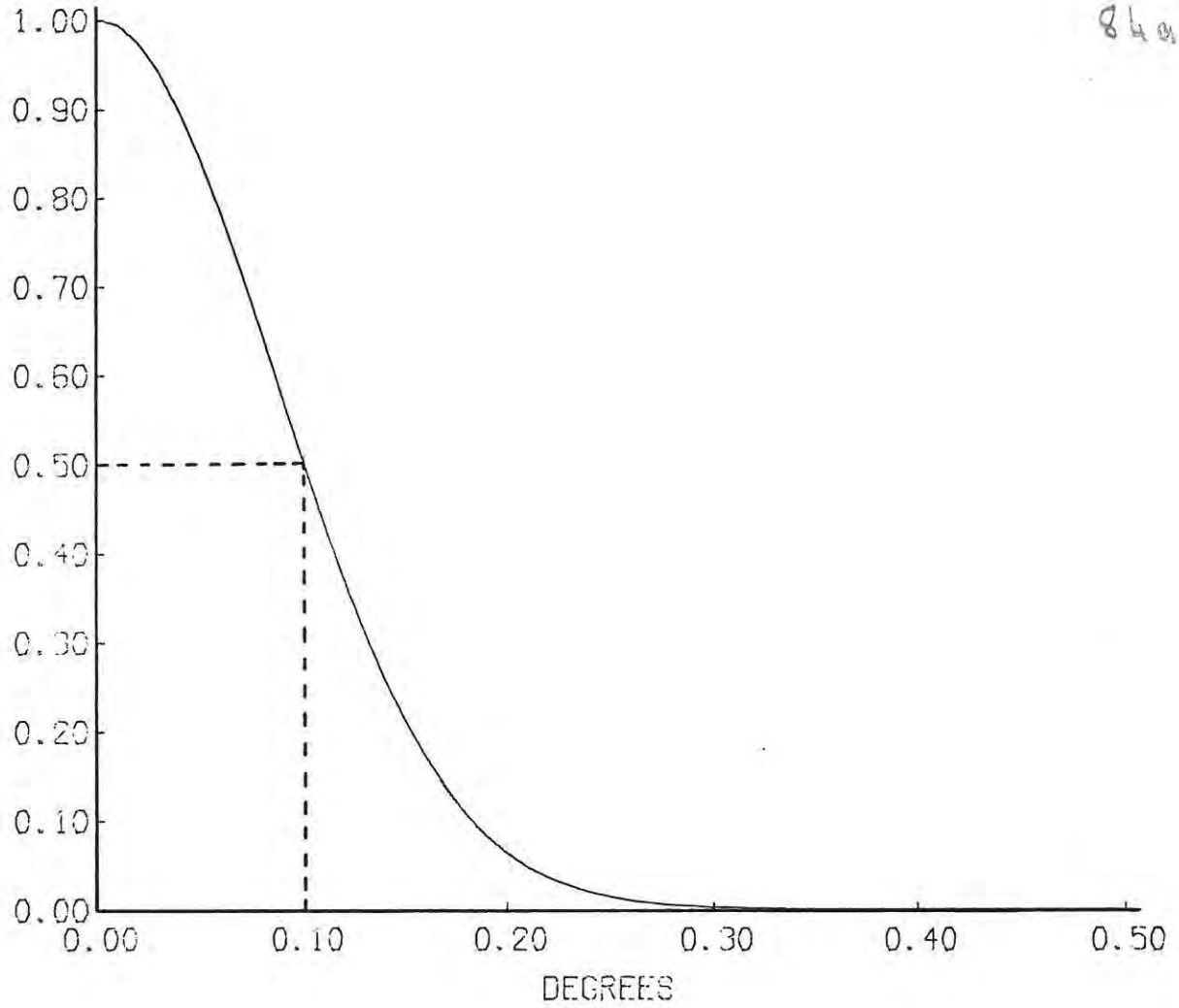
1.00
0.90
0.80
0.70
0.60
0.50
0.40
0.30
0.20
0.10
0.00
0.00
0.10
0.20
0.30
0.40
0.50
DEGREES

(a)

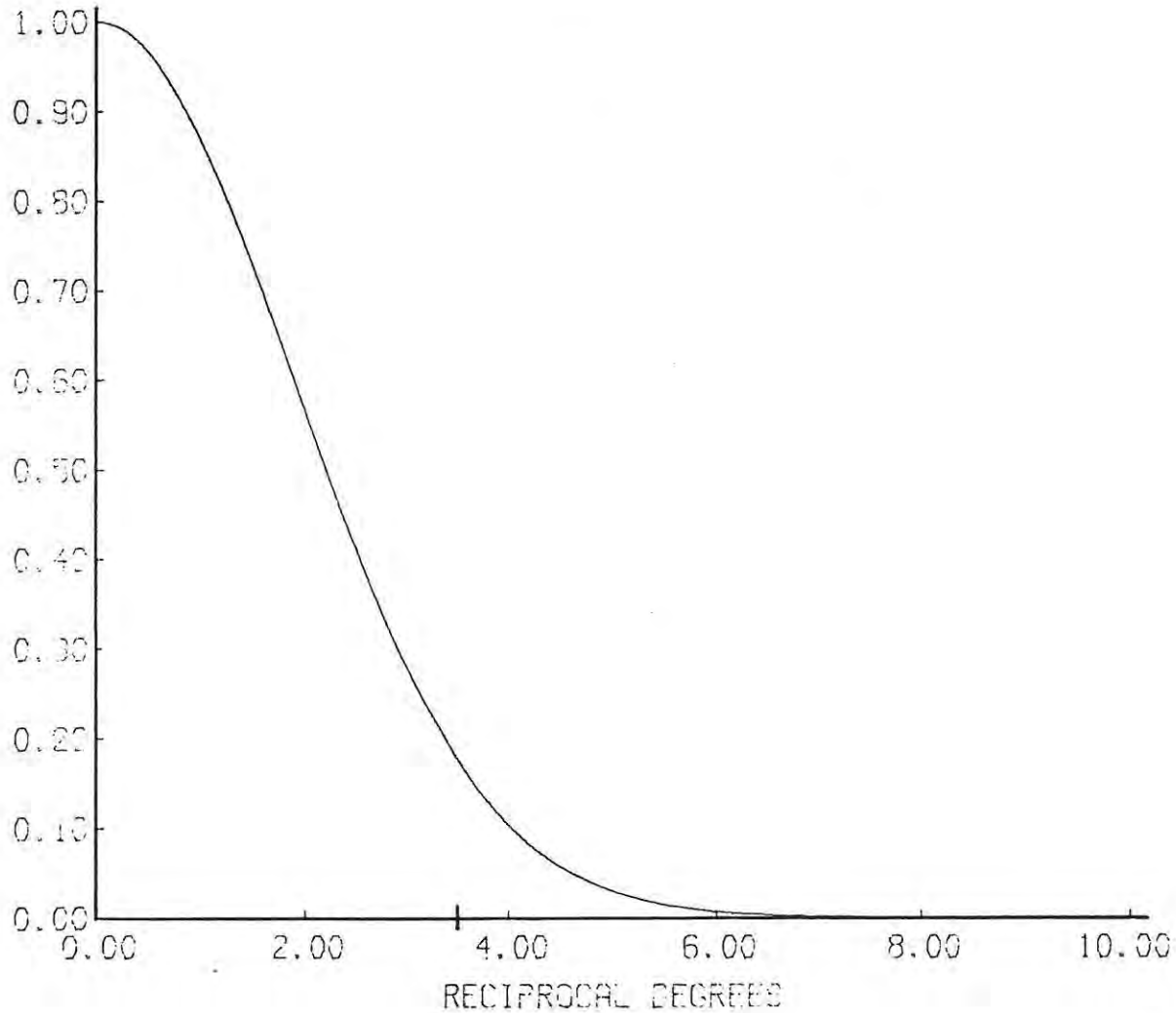
1.00
0.90
0.80
0.70
0.60
0.50
0.40
0.30
0.20
0.10
0.00
0.00
2.00
4.00
6.00
8.00
10.00
RECIPROCAL DEGREES

(b)

Figure 5.7

Degradation of the resolution of the data due to Gaussian smoothing (compare with figure 4.2).

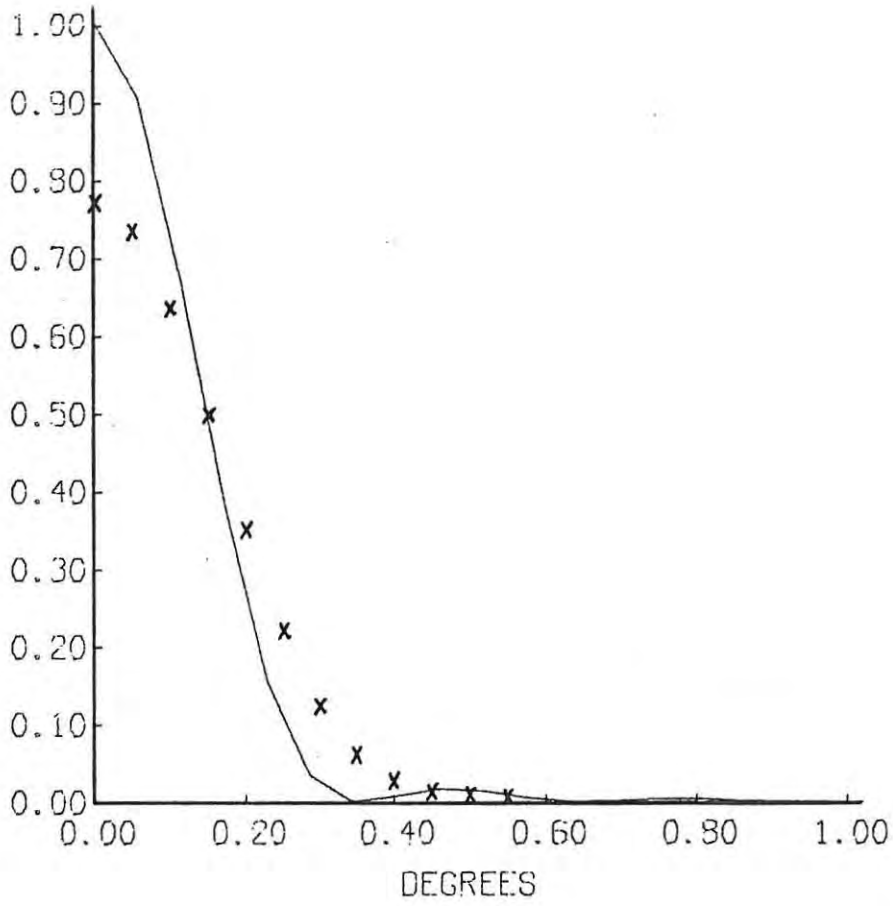
1.00
0.90
0.80
0.70
0.60
0.50
0.40
0.30
0.20
0.10
0.00
0.00
0.20
0.40
0.60
0.80
1.00
DEGREES

eliminate the high frequency noise components completely, because it does not have a sharp cut-off. The spatial frequency passband is tapered, and so the edge effects in the spatial domain are not as severe.

Implementation

Program CONV implements this convolution filter. Since the same samples of the convolution function are used across the entire data set they are pre-calculated and stored in an array. The shape of the base of the filter varies with the lowest latitude of the data in order to take care of the cosine compression. This ensures that the resolution of the data is not degraded beyond 0.4 degrees, but the data is still filtered effectively. The data is read scan by scan from the input data file into a circulating buffer, the width of which depends on the width of the filter in the longitude direction (i.e. it depends on the lowest latitude of the data). After a filtered scan is written out a new input scan is read into the buffer, overwriting the 'oldest' scan in it. Since the spatial filter has a finite extent the edge effects are easily reduced by extending the edge values of the data by half a filter width in all directions. This extension has a similar effect to the guard band used for the Fourier filter.

This program uses much less main memory space than the Fourier filter. Because the total filter width is relatively small (i.e. there are few samples of the convolving function), the speed of the process compares well with the speed of execution of the Fourier filter. It also has the advantage that the data does not have to be extended to have dimensions which are integral powers of two.

5.3 Interpolation

Some small features in the data are resolved or partially resolved by the telescope, but have too few samples to be displayed effectively by means of contour maps or grey scale images. The number of samples may be increased by Fourier interpolation. This interpolation consists of two processes; the reconstruction of the original continuous data from the samples and the resampling of this continuous data. In the spatial frequency domain this corresponds to eliminating all replicas of the spectrum of the sampled signal except for the central one, and then replicating this spectrum at wider intervals.

This process is illustrated in figure 5.8. Diagram (a) shows a typical sampled function and its hypothetical periodic spectrum. The N-point D.F.T. of the sampled data returns a sequence of N values representing one replication of the spectrum, as illustrated in diagram (b). This is the spectrum of the replicated, but unsampled original function. The N-point D.F.T. sequence is extended to N' points and an N'-point inverse D.F.T. is performed on this extended sequence. This returns N' samples of the original function (figure 5.8(c)).

The FORTRAN program INTR was written to implement this interpolation. Again the computer main memory size limits the number of samples making up the interpolated data. The input data are read from the input file into an array with integral power of two dimensions. The D.F.T. of this array is performed by subroutine RTC2. The elements of this array are transferred to a larger array so as to extend the transform data array with zero values. The inverse D.F.T. is then performed on this extended array to return the interpolated data, which are written to the output file. The two arrays mentioned share the same memory space (using the FORTRAN Equivalence statement) so as to reduce the main memory requirement of this program.

Figure 5.8

Illustration of Fourier interpolation.

(a) Original sampled function and its replicated spectrum

(b) Reconstructed continuous function and its spectrum

(c) Resampled function with its spectrum replicated at wider intervals than that in (a)

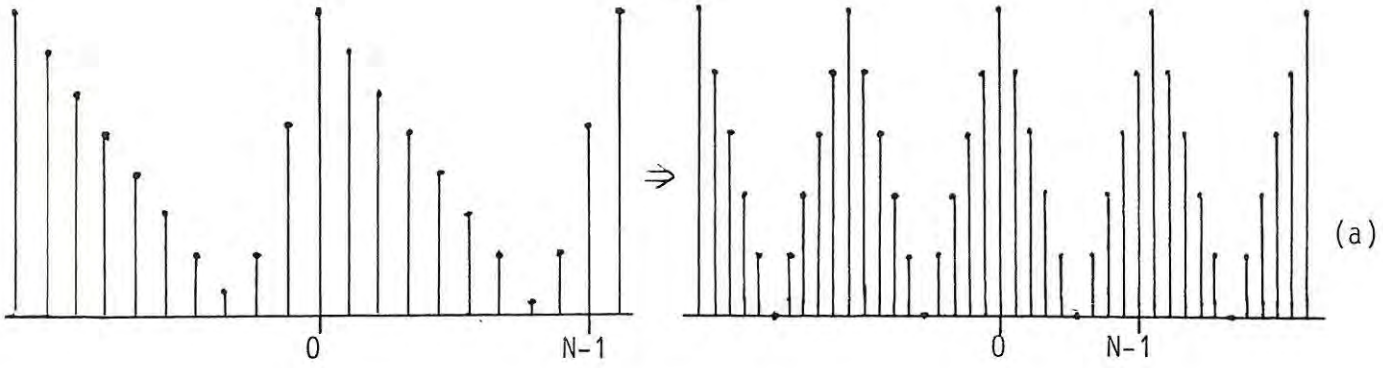

(a)

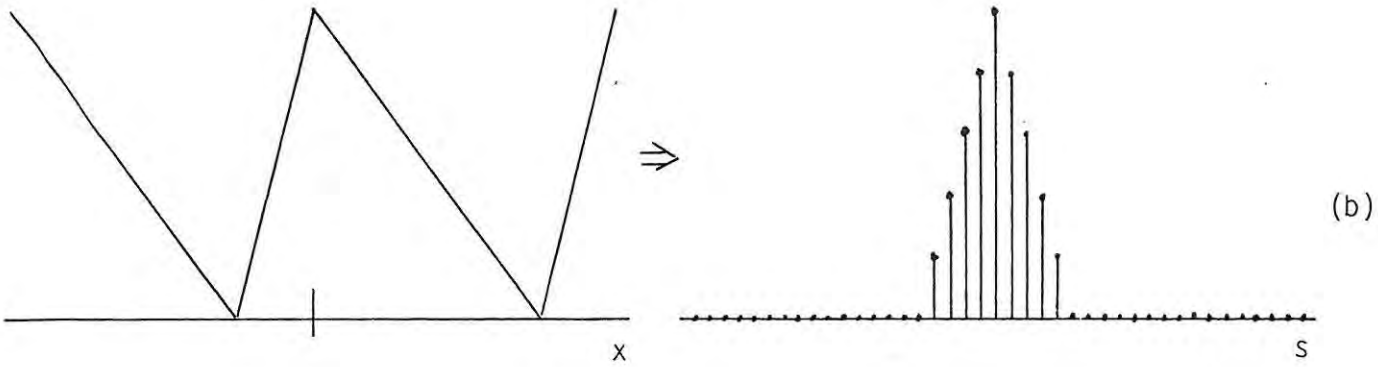

(b)

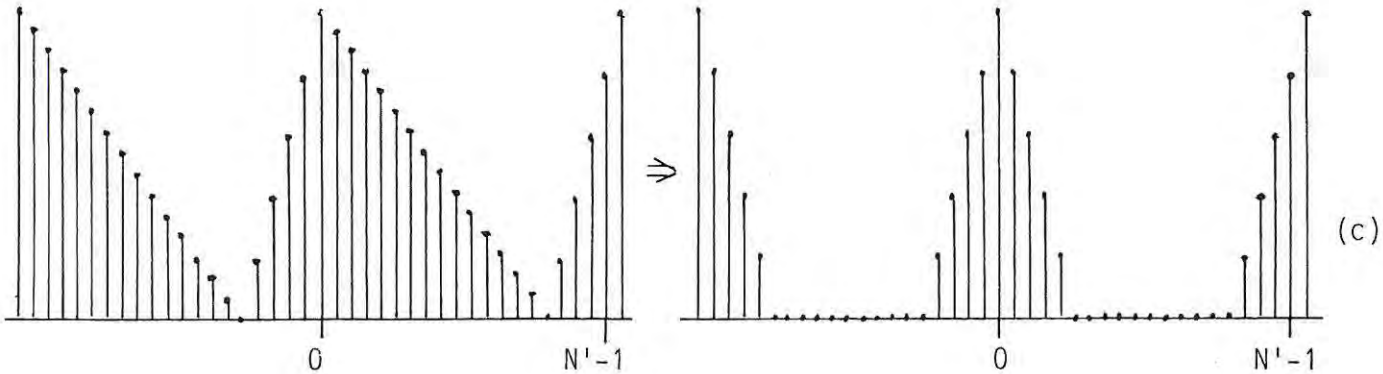

(c)

5.4 Galactic Plane Removal

The major part of the celestial radio power received by the telescope is due to emission from the galactic disc. This radiation consists of both thermal and synchrotron components. Other workers (Phillipps et al 1981a,b) have modelled the synchrotron radiation using the results of the 408 MHz survey (Haslam et al 1982). This radiation introduces a large dynamic range and gradient into the map data, and it is difficult to examine low brightness features superimposed on this gradient. A method for removing most of the galactic disc contribution was devised, making certain assumptions about the radiation.

These assumptions are:

i) The general galactic disc contribution does not form small features (less than 5 degrees in longitude).

ii) It decreases with galactic latitude.

iii) It is symmetric about the galactic equator.

Any galactic radiation which does not obey these assumptions must either be due to some local feature or an asymmetry in the galactic disc. Neither of these two types of radiation should be removed from the data since they are worthy of investigation in their own right.

Flanagan (1981) devised a method for subtracting the galactic disc radiation by fitting Gaussian latitude profiles to a smoothed version of the data (on a galactic coordinate grid), not assuming symmetry about the equator. These profiles were used to construct a 'base surface', which was assumed to model the disc emission, and this surface was subtracted from the data. This resulted in the significant enhancement of low brightness features, but proved to be computationally expensive.

The method described below is illustrated in figure 5.9. The galactic data is split into 5 degree longitude strips. The minimum temperature for each

Figure 5.9

Illustration of the construction of the base surface approximating the Galactic disc emission.

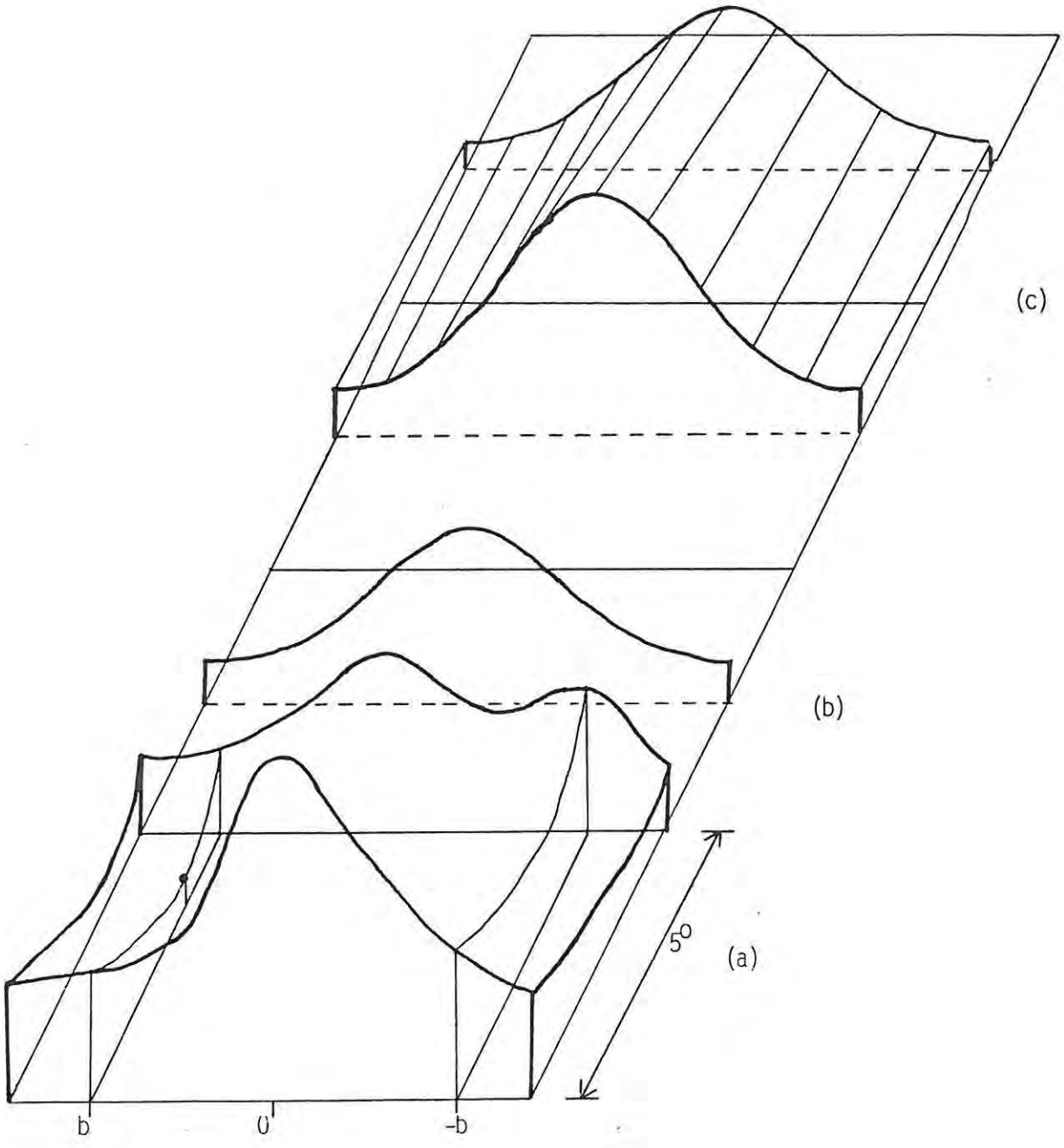
(c)
(b)
(a)
5°
b
0
-b

latitude interval in the strip is calculated, effectively removing any small structure from the resulting profiles (figure 5.9(a)). The minimum of the two values calculated at +b and -b is chosen as being representative of the profile at +b and -b for that strip. These minimum profiles are smoothed and forced to decrease monotonically by running a 'minimum of five' filter along the profiles from the equator outwards. These profiles are assumed to be representative of the galactic disc emission at the centre longitude of the 5 degree strips (figure 5.9(b)). A base surface is constructed by linearly interpolating between these profiles to obtain samples at the grid spacing of the original data (figure 5.9(c)).

Implementation

Two FORTRAN programs were written to perform this base surface subtraction. FITP generates the smoothed, symmetrical profiles at 5 degree intervals, and SUBT interpolates the base surface and subtracts it from the data.

5.5 Flux Measurement

The measurement of the flux density of radio sources is necessary for most quantitative analysis. The process involved consists of separating the source from the surrounding radiation and calculating its integrated flux density. Even though the structure of the source may not be resolved by the telescope, its integrated flux may be measured, so long as no other sources are confused with it. An expression for the flux density of a source superimposed on a zero base-level and isolated from any other sources is derived below.

The integral of the antenna temperature over the source and its sidelobes is related to the integral of the brightness distribution smoothed by the antenna beam pattern by equation 5.5.1.

$$\iint_{4\pi} T_a(\delta,\alpha)\, d\Omega = \frac{R.\lambda^2}{2k\Omega_a} \iint_{4\pi} B(\delta,\alpha) * P_n(\delta,\alpha\cos\delta).\cos\delta\, d\Omega \qquad 5.5.1$$

This is derived from equation 4.1.23 by performing some substitution. Both integrations are performed over a solid angle subtended by the source and sidelobes.

Using the fact that convolution in the spatial domain corresponds to multiplication in the frequency domain, and that the integral of a function over its entire extent is equal to the value of its transform at the spatial frequency origin, the integral on the right hand side of equation 5.5.1 may be separated to yield:

$$\iint_{4\pi} T_a(\delta,\alpha)\, d\Omega = \frac{R.\lambda^2}{2k\Omega_a} \iint_{4\pi} B(\delta,\alpha)\, d\Omega \iint_{4\pi} P_n(\delta,\alpha\cos\delta)\, d\Omega$$

$$= \frac{R\lambda^2}{2k} \iint_{SOURCE} B(\delta,\alpha)\, d\Omega \qquad 5.5.2$$

The integration of the brightness distribution is effectively performed over the area of the source, since the brightness function is zero outside these limits. In practice the integration of the antenna temperature does not include all of the sidelobes, so a correction factor, ϵ, must be applied. This correction factor depends on the source size, and is equal to ϵ_M for a point source. Thus the expression for the source flux is:

$$\iint_{SOURCE} B(\delta,\alpha)\, d\Omega = \frac{2k}{\epsilon R\lambda^2} \iint_{\Omega_\epsilon} T_a(\delta,\alpha)\, d\Omega \qquad 5.5.3$$

Implementation

Program FLUX measures the flux density of a radio source given its central coordinate and angular extent. The fluxes of any number of sources may be measured with just one run of the program, provided the input list of source

coordinates is arranged in order increasing right ascension. This is necessary because an entire map may not fit into the main memory of the computer, so a small section of the data is kept in a circulating buffer at any one time. It would be very inefficient to search backwards and forwards in the data file for each source.

The source temperature distribution is integrated numerically over a rectangle with dimensions given by the user and centred on the source. Before the integration may be performed, a background surface must be subtracted from the data in order to isolate the source from the radiation on which it is superimposed. This surface is obtained by fitting a least squares, two dimensional quadratic to the data around the edge of the rectangle over which the integration is performed. After the subtraction the residual source temperature distribution is integrated, and the flux density is calculated using equation 5.5.3.

5.6 Data Display

No data analysis is possible without some effective form of data display. There are two main practical problems involved in displaying our data, i.e.

1) Large volumes of data, typically 500 000 data samples

2) Large dynamic range, 32 000 to 1.

Three methods of display are currently in use, each with its advantages and disadvantages. Plotting contours of radio isophotes is probably the most versatile and widely used method of radio astronomy data display. Most structures in such maps can be picked out visually and quantitative comparisons are easy. The disadvantages of this method are that some structures, especially large ones, are not highlighted, and the plotting of contours for large data sets takes a long time. Each of the maps in the appendix took half an hour to plot.

By representing radio brightness as shades of grey, features of the data are easily distinguished visually, being in a more 'natural' form. The main disadvantage of producing 'images' of the data is that quantitative analysis of the data is impractical, but in conjunction with a contour map the astronomer has all the visual information he needs for the analysis of the data. Two grey scale imaging techniques were developed; one for producing quick, rough images locally, and another for making high quality images using the satellite imaging facility of the C.S.I.R. The implementation of these various forms of data display are described below.

5.6.1 Contour Plotting

Various contour plotting programs have been in use for some years by the Radio Astronomy group, so these are not described in detail. Various aesthetic modifications were made to the programs. The axes and contour labelling routines were modified to produce neater and more efficient labelling. The original contour program assumed that the data was on an equatorial coordinate grid, so another version was written to accept data on a galactic grid. The coordinate plotting routines were changed so that a galactic coordinate grid can be overlaid on the equatorial data, and an equatorial grid on the galactic data. All of the contour maps presented were drawn by either the equatorial or the galactic plotting program.

5.6.2 Printer Grey Scale Maps

It was always felt that there was a need for some form of display which would afford a 'quick look' at the map data. The turn around time for a contour map is usually one day. The use of a dot-matrix printer to produce coarse grey scale maps reduced this time to less than an hour. For some puposes the grey scale representation is better than the corresponding contour map.

The term 'pixel' is used in image display. This is the smallest distinct picture element in the image. The grey scale output generated by our printer consists of one pixel per data sample. The shade of grey of the sample is a measure of the data value. Each pixel consists of an array of six by six dot positions, the shade of the pixel depending on the number of dots printed. Various patterns for positioning these printed dots were tried to give the best distinction between adjacent shades. Theoretically 37 shades are possible with this matrix, ranging from white (no dots printed) to black (all dots printed). In practice, however, it was found that only 21 distinct levels could be distinguished, therefore the resulting display has a dynamic range of 21 to 1. This is very much smaller than the range of the data, but reasonable results are obtained if the temperature interval between adjacent shades is chosen correctly. This method of display is very good for showing up defects in the data (scanning effects and spurious spikes) and large, low brightness structures.

Two programs were written to produce the grey scale images, PGSC and LINK.

PGSC

This FORTRAN program runs on the I.C.L. computer and generates the ASCII codes required for the printer to produce 'bit mapped' images. An initial character string is sent to the printer to set up the line spacing. Data are sent to the printer in the form of graphics records, consisting of an escape code, a byte count, and the data bytes which represent the 'bit patterns'. The program scales the data to the available dynamic range using a scale factor and offset provided by the operator.

The MAXIMOP operating system limits the length of any output string to 120 characters, and so entire lines of pixels could not be written out in one graphics record. An EPSON 100 printer was used for producing the hard copy,

which allows for 816 dots, or 136 pixels, across a page. Writing out the data in short records resulted in a jerky motion of the print head and slowed down the operation of the printer. This problem was solved by interfacing the printer to the mainframe using a micro-computer running program LINK.

LINK

This program was written in MC6809 machine language for the micro-computer used to interface the printer. It employs interrupt routines to service a terminal, the printer and the data line from the mainframe simultaneously. Normally the computer is transparent to both the terminal and the data line, the terminal acting like any other MAXIMOP terminal. By issuing the command 'CONTROL-R' from the terminal the output from the data line is routed to the printer. This re-routing is not transparent. The program concatenates the short graphics records so that only one long record is sent to the printer for each line of pixels printed. In this way the printer can easily cope with the 1200 baud data rate, and its operation is much smoother. A large fifo stack ensures that no output data is lost if the printer should fall behind for some reason. The command 'CONTROL-S' from the terminal returns the flow of data to the terminal.

5.6.3 Optronics Images

The Satellite Remote Sensing Centre (SRSC) of the C.S.I.R. has a facility for producing very high quality grey scale images on a photographic negative. The dynamic range of these images is 256 to 1 and images of 2500 by 2500 pixels can be produced, each pixel being 100 microns square. The images produced are very good, but the turn-around time is about a month because of the remote location of the Centre.

The equipment which produces the images, made by the Optronics company, requires the data to be written on a computer magnetic tape in a special format. A FORTRAN program, PICT, was written to generate such a tape from our data. Each pixel is represented by one byte on the tape. Due to the small pixel size our data is interpolated to take advantage of the full 2500 by 2500 pixel capability. This amount of data is too large to be interpolated using the Fourier method. A simple linear interpolation technique is used to expand the data dimensions by any integral factor. The dynamic range of the data is reduced in a similar way to that used in program PGSC.

5.7 Image Transportation

Because of the increased use of digital techniques in astronomy a lot of astronomy data is in a digital form. A standard format has been defined for the storage of these data to facilitate the exchange of data between various sites (Wells et al 1981). This system has been given the name FITS (Flexible Image Transport System), and has been adopted by the International Astronomical Union. The format which we use to store our data locally is very different to this standard, but is well suited to our data processing. A FORTRAN program, FITS, was written to generate standard FITS format computer tapes of our image data so that it can be 'exported' easily.

CHAPTER 6 THE OBSERVATIONS AND RESULTS

The apparatus and method used for the observations have already been discussed in chapter 2. This chapter deals with the observation of the second part of the all sky survey. The raw data was processed using the programs described in the previous chapter and the resulting data are presented here in the form of contour maps and images of the radio brightness distribution. The data took two years to reduce and process. Future maps will not take as long because the reduction programs have all been debugged, the image processing programs have been written and the University has purchased a more powerful computer.

6.1 The Observations

The observations for the second part of the survey were made over a period of two months starting from June 1980. Being the middle of winter the nights were long and the weather good, i.e. no rain, clouds or electric storms. Declinations between -63^{o} and -24^{o} were scanned. The observations were started at sunset at a right ascension of about 10h30m and stopped at sunrise. The radiation from the sun is detected in the sidelobes of the antenna pattern and so no useful observing may be done during daylight hours. Data up till one hour after sunset was ignored because of the effect of the cooling down of the telescope environment on the baseline of the receiver output. The hour-angles of the observations varied from -1^{o} to 45^{o}.

Eight interleaved rasters were required to observe the 39^{o} declination range, so a total of 24 observations was required to have three repeats of each raster. The chart record showed interference in a number of the observations. This was due to nearby lightning discharges, electrical

interference from the feed cone air-conditioner, birds flying over the feed and satellite transmissions. Since all of these forms of interference were transient they would not affect the final data because of the method of reducing the data.

A power failure occurred during one of the observations. The observation was continued after the interruption, but because the antenna was scanning at a different hour angle the background profile had changed. The data reduction makes no allowance for this and so the data from the observation was not used, reducing the number of observations to 23. Unfortunately the D.V.M. monitoring the radiometer output has a maximum range of 0.32 volts, which corresponds to 32000mK antenna temperature. Radiometer output voltages in excess of 0.32V cause the D.V.M. to overflow. The observing software detects this overflow condition and truncates the data, thus any strong sources with antenna temperatures greater than 32K are truncated to 32K.

6.2 The Initial Processing

The raw map was constructed using the data reduction programs described in chapter 2. The area between right ascensions 12h00m and 23h00m was common to all of the observations, so all data outside of these limits were excluded from the reduction. No right ascension pointing corrections were applied to the data because of the lack of a reliable pointing error map of the antenna at low declinations. The positional accuracy of the final map was checked by comparing the measured positions of the extragalactic sources listed in chapter 8 against the positions given in the Parkes catalogue of radio sources. The maximum error in right ascension was found to be 0.1 degrees, while the maximum declination error was 0.05 degrees.

Sufficient data were free of baseline drift for the drift removal process to be successful. Sixth order polynomials were thought to fit the background

profiles of the observations best.

After combining the 23 rasters a contour diagram with widely spaced contour levels was plotted. Even from this coarse representation of the data it was evident that there were severe scanning effects in the data. These scanning effects appeared as striations parallel to the scanning direction, and were due to uncertainty in the relative levels of adjacent scans. This uncertainty was introduced by the variation of the background profile within some rasters because of the effects of precession and bad antenna tracking. The background profile subtracted from each raster was not representative of the entire raster. The next section discusses the technique developed to reduce these scanning effects. This reduction was possible because the rasters are independent and observed at different hour angles. Therefore the effects can be reduced by fitting the individual rasters to a smooth surface derived from the combined rasters.

6.3 Scanning Effect Removal

A set of three programs was written to reduce these scanning effects. The process implemented is similar to the drift removal. The idea is to construct smoothed right ascension scans at various declinations across the data and adjust the data to conform to these smoothed scans. The major difference between this removal and the drift removal is that the drift removal subtracts a constant value from each scan in a raster, while this process removes a profile from each scan. This declination profile is dependent on right ascension, because it is due to precession effects which depend on right ascension (cf section 2.3). The striations in the data are reduced, but the absolute level of the data may still be uncertain.

The raw map is used as input to the first program, 'FDRF'. This program divides the map data into a specified number of wide declination intervals

of equal width. Seven intervals were used for this data. For each scan in the data the medians of the samples which fall into each interval are written out, together with the centre declination of the interval and the right ascension of the scan. This median is assumed to be representative of the level of the interval to which it belongs. Right ascension scans constructed of these medians were plotted for each declination interval.

The next program, 'SDRF', filters these scans in right ascension, using a running median filter. This removes any unwanted rapid variations in the scan which result from the scanning effects. It was realized that this filter would erroneously remove valid rapid variations from sections of the scans which contain large structures and steep gradients. Such areas occur where the scans pass through the galactic plane. Sections of the scans which were likely to be affected were selected and not smoothed. For this reason some striations are still evident in areas of the map close to the galactic plane. The filter used is not a normal running mean. The filter is 16 samples long. These samples are sorted into ascending order, the top and bottom three values are excluded and the mean of the remaining ten values calculated. The difference between the smoothed and the unsmoothed values for a particular scan and declination interval is assumed to be the error in the background profile at the centre of that interval.

Program 'RDRF' removes these residuals from the original map data. Piecewise linear interpolation is employed to obtain residuals for declinations between the centres of the declination intervals. This process greatly reduced the scanning effects, but there was still evidence of uncertain data, mainly single samples which appeared much higher or lower than surrounding samples. These were removed using a 9-point, two dimensional median filter. There was evidence of bad data after 22h00m, so this data was excluded. The RMS noise fluctuation in the data at this stage

of the processing was 21.6 mK, measured by calculating the standard deviation of 3731 samples from a flat area of the data.

6.4 The Results

The appendix contains a mosaic of contour maps of the data smoothed using the convolution filter described in section 5.2. The filter reduces the RMS noise level by a factor of

$$2.13\sqrt{\sec(\text{lowest declination of map})}$$

where the lowest declination is the declination with the smallest absolute value. The key for these maps gives the details of the contour levels. The convolution filter masks the effects of the D.V.M. overflow problem, smoothing the flat tops of the truncated sources. Any source which appears stronger than 30000mK must be assumed to be truncated, and thus the peak temperature for these sources is unreliable. Due to the relationship in equation 4.1.20 the full beam brightness temperature may be calculated from

$$T_b = 1.41T_a$$

The large dynamic range of the data makes these contour maps very difficult to interpret and the equatorial projection distorts the data. Figure 6.1 is a grey scale image of the data on a galactic coordinate projection. The coordinate transformation was performed by the program described in chapter 5, using the coordinates given by Lane (1979). This map also contains data from the third section of the sky survey, an area from -80^{o} to -61^{o} declination and over the same right ascension range as the second section. These two sets of data could only be combined after the coordinate transformation because of their different right ascension scan spacing. The additional data still has bad scanning effects in it, but it was incorporated so that the galactic disc emission could be modelled more effectively. Large scale structures which extend through both sections of

data also become more evident.

The transformed data was smoothed using the convolution filter, and the image was produced by the imaging facility of the S.R.S.C. Program PICT was used to generate the data for the imaging device. A base offset of 100mK was added to the data and one grey scale level represents 5mK. The offset ensured that there were no negative data pixels due to noise fluctuations. The data were interpolated so that the image would fill the negative. No contour map of this data is presented because of the large number of data points and large dynamic range of these data.

Using the observing method and data reduction process describe previously, a raw data map was produced. These raw data were then enhanced using techniques described in chapter 5 and presented as contour maps and images. The following two chapters deal with large and small scale features of these maps, presenting more detailed maps of the areas of interest.

Figure 6.1

Grey scale image of the data on the Galactic coordinate grid.

RHODES UNIVERSITY SOUTHERN SKY SURVEY
2.3GHz

CHAPTER 7 GALACTIC ASTRONOMY

This chapter deals with the emission from our Galaxy, the Milky Way. This emission is due to a number of mechanisms. The source and mechanism of the various galactic emission features may be deduced by examination of the structure, brightness, spectral characteristics and optical counterparts of this radio emission.

The general Galactic emission consists of a strong ridge peaking within 3 degrees latitude of the plane, and lower brightness emission extending out to higher latitudes. The brightness of this extended emission decreases with increasing latitude, the brightness and latitudinal extent depending on the galactic longitude. At zero longitude the emission extends out to at least -40 degrees latitude.

Superimposed on this general galactic disc emission are numerous sources of emission with wide ranges of angular size and brightness. Many of the small point sources (i.e. sources which have angular extent much less than the antenna beamwidth) are of extragalactic origin, and are discussed in chapter 8. The large emission feature at 13h30m right ascension and -44 degrees declination is CENTAURUS A which is also an extragalactic source discussed in the next chapter.

This chapter examines prominent galactic emission features observed in the second part of the survey, comparing the new data with previous results, and indicating the large loop-like and filamentary structures which occur about the galactic plane. The detailed examination of all of the features in this map is beyond the scope of this thesis.

7.1 The Galactic Disc Emission

In order to obtain a map of the large scale galactic emission distribution the galactic coordinate grid data (fig 6.1) were processed using program FITP. This program, which was described in chapter 5, derives a 'lower base surface' from the input data, removing all small scale structure and discrete sources of emission. A contour map of the resulting surface is shown in figure 7.1. The surface is symmetric about the galactic equator and decreases monotonically with increasing latitude because of the assumptions made to obtain it. This surface, which contains no features with angular dimensions smaller than 5 degrees, is assumed to represent the galactic disc emission.

The strong equatorial ridge of emission seen in the original data is still very evident in the smooth surface. This ridge is evidence that the Milky Way is disc shaped. The enhanced emission occurs along lines of sight which pass through the galaxy edge on, i.e. in a narrow band about the Galactic equator. This emission is generally understood to be due to synchrotron radiation by electrons spiralling in the Galactic magnetic field. Another possible explanation is that it is thermal emission due to gas ionised by stars in the disc. The spectrum of the radiation can be used to disinguish between these two possibilities.

Figure 7.2a illustrates the profiles of the original data and the base surface along b = 0 degrees. Similar profiles (Phillipps, et al 1981a) derived from the 408MHz all sky survey data (Haslam, et al 1982) are shown in figure 7.2b for comparison (note that the longitude axes of these two diagrams are mutually transposed). The peaks (marked a, b, c, etc) in the two unsmoothed profiles correspond. Phillipps et al use their smooth profile to determine a two-armed spiral model for the galaxy, assuming the galactic radiation to be due to synchrotron emission. The steps in the

Figure 7.1

Base surface representing galactic disc emission at 2.3 GHz.

Contour levels

Contour label	Antenna temperature (mK)
1	50
2	100
3	150
4	200
5	250
6	300
7	400
8	500
9	600
10	700
11	800
12	900
13	1000
14	1300
15	1600
16	2000
17	2500
18	3000

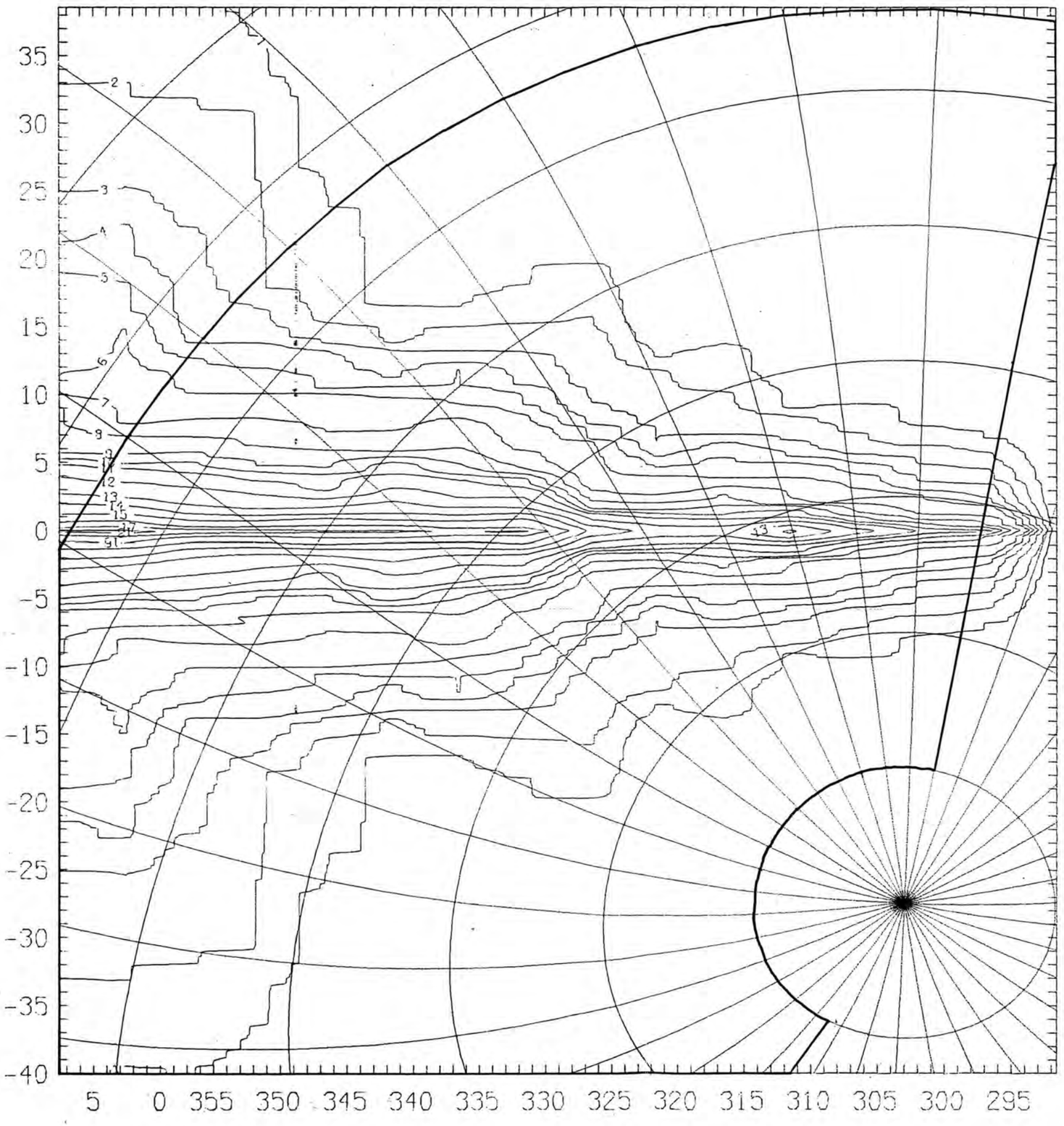
35
30
25
20
15
10
5
0
-5
-10
-15
-20
-25
-30
-35
-40
5
0
355
350
345
340
335
330
325
320
315
310
305
300
295
1
2
3
4
5
6
7
9
11
12
13
14
15
17
21
91
13

Figure 7.2

Original and lower profiles along the Galactic equator.

(a) 2.3 GHz (Note scale is in units of 10^4mK)

(b) 408 MHz (after Phillipps et al 1981a)

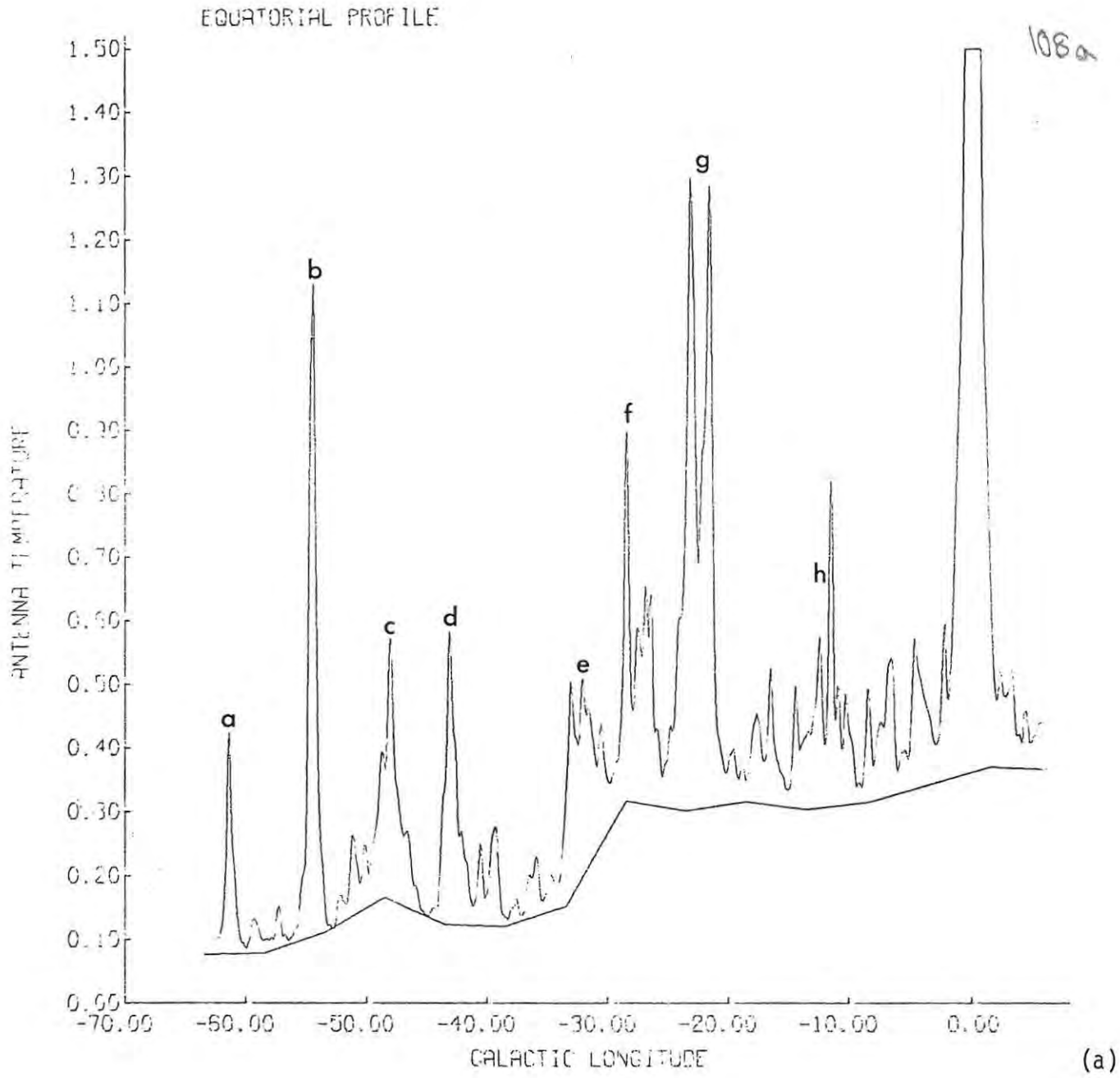
EQUATORIAL PROFILE
ANTENNA TEMPERATURE
1.50
1.40
1.30
1.20
1.10
1.00
0.90
0.80
0.70
0.60
0.50
0.40
0.30
0.20
0.10
0.00
-70.00
-60.00
-50.00
-40.00
-30.00
-20.00
-10.00
0.00
GALACTIC LONGITUDE
a
b
c
d
e
f
g
h

(a)

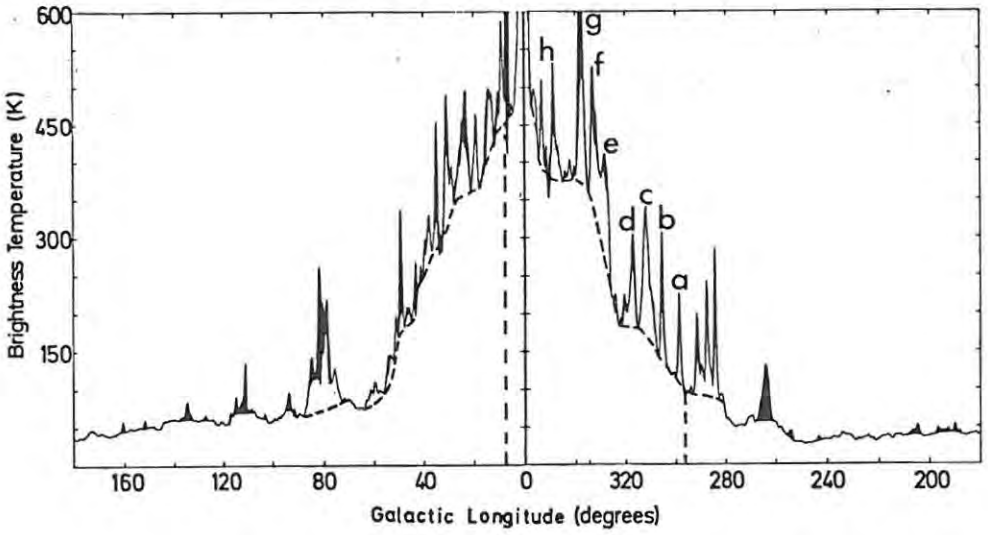
Brightness Temperature (K)
600
450
300
150
160
120
80
40
0
320
280
240
200
Galactic Longitude (degrees)
a
b
c
d
e
f
g
h

(b)

profile are consistent with the spiral model. The steps in the brightness occur where the line of sight passes tangentially through a spiral arm. Because the absolute zero level of the 2.3GHz data is not known, it is not possible to find the spectral index as a function of longitude by comparing the absolute brightness temperatures of the two smooth profiles. The spectral indices for the radiation causing the steps in the profiles can however be calculated. The magnitude of these steps is independent of the absolute level of the data. The steps at $l = 310^{o}$ (-50^{o}) and $l = 330^{o}$ (-30^{o}) are clearly defined for both profiles. The size of each step was taken from the difference in height of the plateaus on either side of the step. The peak at the galactic centre does not appear in the smooth profile for the 2.3GHz data because it is less than 5 degrees in extent. By comparing the amplitudes of the steps at the two different frequencies the spectral index of the radiation responsible for the steps may be calculated. Because the brightness temperatures of large scale features are being compared there are no beam dilution effects which have to be taken into account. The table below gives the results of this analysis.

Step at	T_b(408MHz)	T_b(2.3GHz)	α
$l = 310^{o}$	90K	609mK	$-0.89 \pm 20\%$
$l = 330^{o}$	200K	2660mK	$-0.50 \pm 20\%$

assuming $T_b = K.\nu^{\alpha-2}$

These spectral indices are indicative of non-thermal emission. Thermal emission has a minimum spectral index of -0.1 (cf section 7.3), so the steps are definitely not due to the thermal mechanism. The non-thermal synchrotron mechanism produces radiation with a spectral index which depends on the energy distribution of the electrons spiralling in the magnetic field (Shklovsky 1960). If these electrons have the energy distribution of cosmic

ray electrons the spectral index of the radiation would be -0.7 (Kraus 1966). Phillipps et al assume the synchrotron mechanism in their modelling process.

The smooth map of the disc emission shows the latitude dependence of the general galactic radiation clearly. The bold outline indicates the extent of the original data. Since the base surface is forced to be symmetrical it shows emission outside the bold outline where there is no original data, substituting the brightness values from the latitude of the same magnitude but opposite sign. The large extended structure along zero longitude is due to data on the south side of the plane only, because of the lack of data on the northern side.

The latitudinal extent of the emission is seen to broaden at the same longitudes as the steps in the $b = 0^{o}$ profiles. This is especially prominent in the strip within 5 degrees latitude of the plane. Using the 408Mhz survey data (Haslam, et al 1982), Phillipps, et al (1981b) derive a cross-section of the emissivity of the Milky Way galaxy. Again the radiation is assumed to be due to the non-thermal synchrotron mechanism. In order to obtain spectral indices for the high latitude radiation, longitude scans from the 408MHz and 2.3GHz data were compared. The scans for the 2.3GHz data were obtained from the base surface, while the scans for the 408MHz data were generated from the published contour map of the data smoothed to 2 degrees spatial resolution (Haslam, et al 1982). The data for the 408MHz scans were chosen so that the scans would compare with those of the 2.3GHz data (i.e. from the same side of the plane). In order to avoid the problem of absolute temperature levels for the two sets of data, base levels were subtracted from the longitude scans so that the temperature at 40 degrees latitude was zero. The average spectral indices, with standard

deviations, are tabulated below.

l =	300^{o}	330^{o}	0^{o}
α =	-0.64 ± 20%	-0.84 ± 20%	-0.83 ± 20%

The average spectral index, taking into account all the data for the 3 scans, was calculated to be -0.73 ± 20%. This confirms the assumption of Phillipps et al that the high latitude disc radiation is predominantly due to synchrotron emission.

The lower base surface was subtracted from the original data using program SUBT, and a grey scale image of the residual data is shown in figure 7.6. Many emission features are enhanced in this map because of the removal of gradients caused by the galactic disc contribution. So also are residual scanning effects which appear as lines radiating from the celestial south pole. These are mainly in the poor data of the third part of the survey. Because the subtracted surface is symmetric about the galactic equator, asymmetries in the galactic emission remain in the residual data. Numerous features appear about the Galactic equator. Those very close to the equator are mainly due to thermal emission from HII regions. There is too much information in this data to all be covered in this thesis. The remainder of this chapter examines prominent and interesting features in this residual data.

7.2 Supernova Remnants at High Latitudes

The map in figure 7.6 shows the emission from 3 known high latitude supernova remnants. Their occurrence at high latitudes implies that they are nearby objects, which is borne out by their relatively large angular size. Each of the emission features associated with the the supernova remnants is discussed in turn below.

Figure 7.3

Supernova remnant PKS 1209-52

(a) Contour map of emission at 2.3 GHz. Contour intevals of 30mK antenna temperature. New galactic coordinates.

(b) Continuum spectrum of PKS 1209-52. Point with error bars represents flux density at 2.3 GHz.

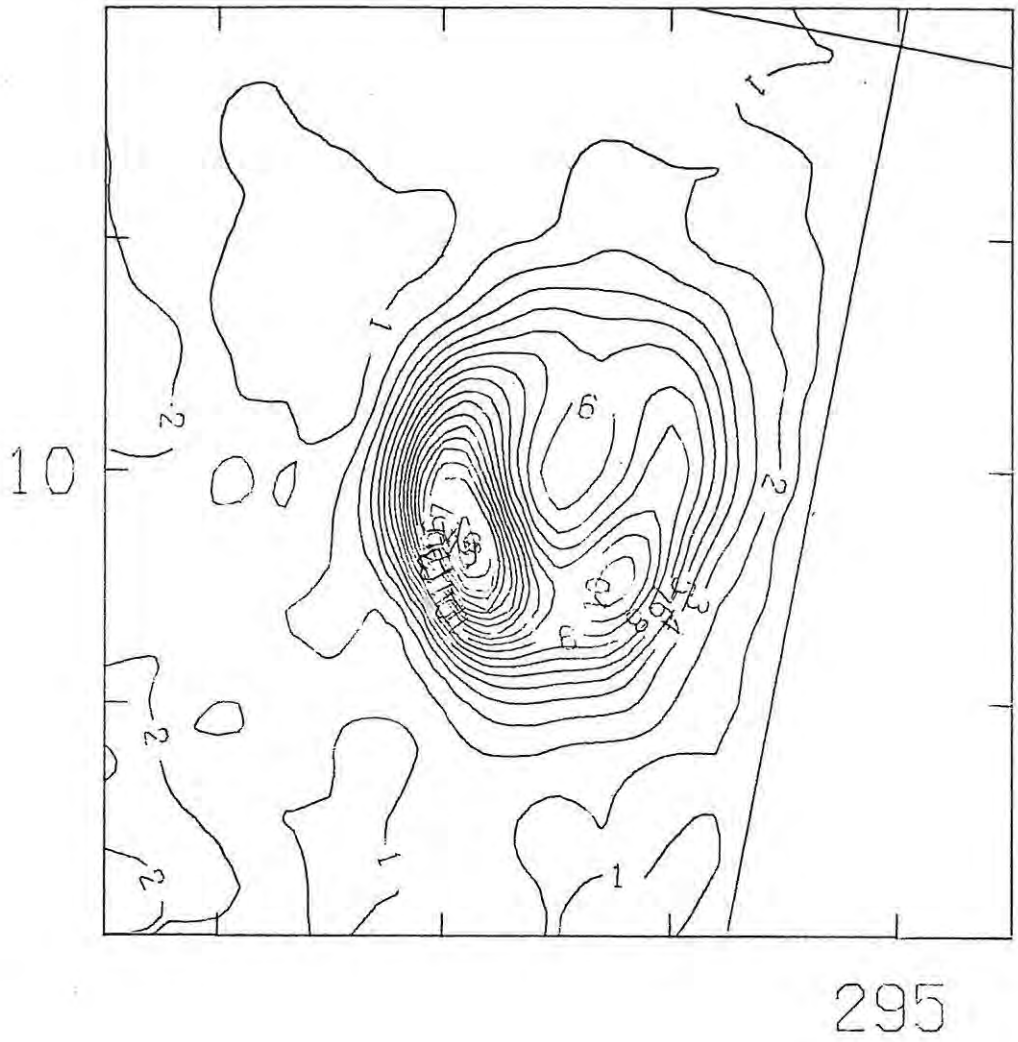
10
295

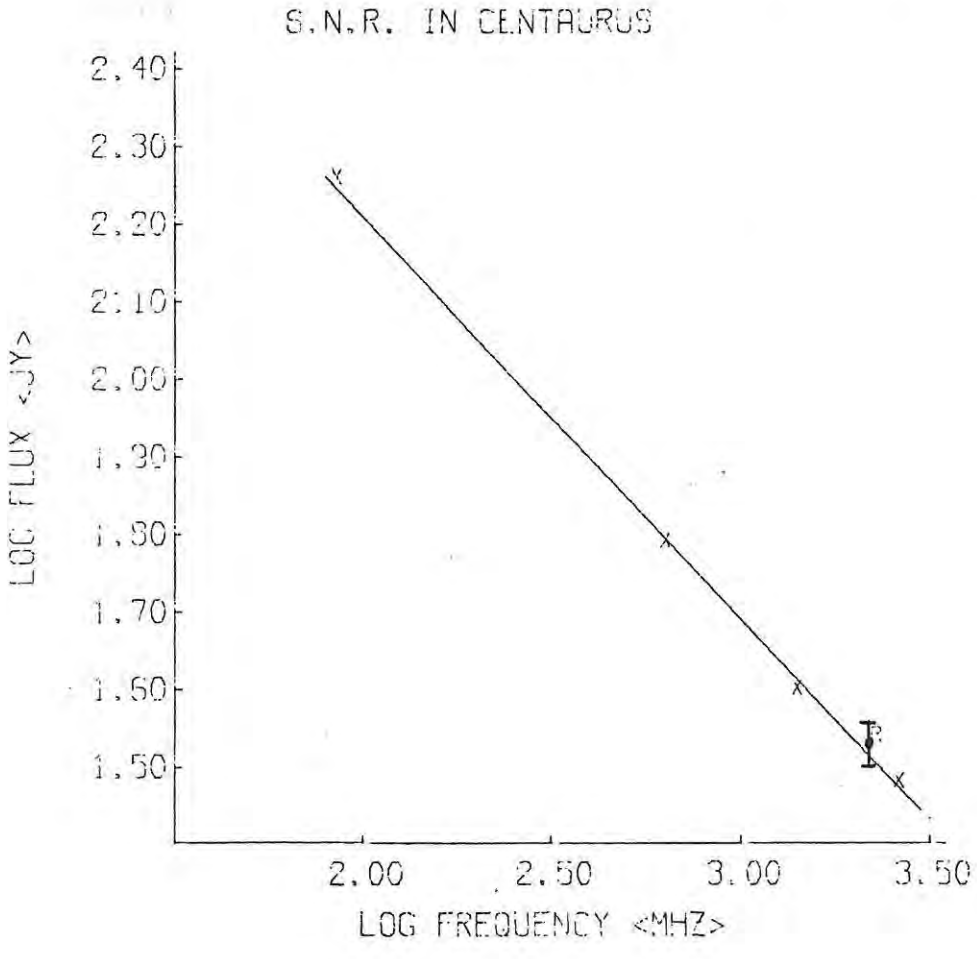
S.N.R. IN CENTAURUS
LOG FLUX <JY>
2.40
2.30
2.20
2.10
2.00
1.90
1.80
1.70
1.60
1.50
2.00
2.50
3.00
3.50
LOG FREQUENCY <MHZ>

i) S.N.R. in Centaurus (PKS 1209-52)

There is a distinctive shell-like emission feature at 12h06m right ascension, -52.3 degrees declination. Figure 7.3(a) is a more detailed map of the feature. It has an angular diameter of 1.5 degrees and has approximate galactic coordinates $l = 297^{o}$, $b = 10^{o}$. The shell structure of the brightness distribution is resolved by our beam. Whiteoak and Gardener (1968) have studied the polarization and intensity distribution of the radio source at 629MHz, 1410MHz and 2650MHz. They suggest that the emission comes from the remnant of a type II supernova, taking into account the strong polarization (15-25%), circular symmetry and flatter spectrum ($\alpha = -0.52$) of the radiation. They report that no optical counterpart has been found, making distance measurement difficult.

The integrated flux of the source at 2.3GHz was measured to be 34.5Jy with error limits of 6%. This value is compared to the data of Whiteoak and Gardner in figure 7.3(b). Interpolating their data results in 2.3GHz flux of 33.9Jy. This value compares well with the observed 2.3GHz flux, even though the observed flux is not corrected for polarization. The maximum error due to polarization would be 12.5%.

ii) SNR 1006 (PKS 1459-41, MSH 14-415)

Gardner and Milne (1965) have suggested that the emission feature at 15h00m right ascension, -41.75 degrees declination (see figure 7.4) is due to the remnant of the supernova of 1006. The intensity distribution is not resolved by our antenna, but the feature in the map (figure 7.4) is seen to be more extended than a point source, implying that it has an angular extent which is of the order of minutes of arc. Higher resolution maps by Milne (1971) show that the source has a shell structure with an angular diameter of 35' of arc. The structure of this source is very similar to that of

Figure 7.4

Contour map of SNR 1006 - Lupus Loop area at 2.3 GHz.
Contour spacing of 20 mK antenna temperature.

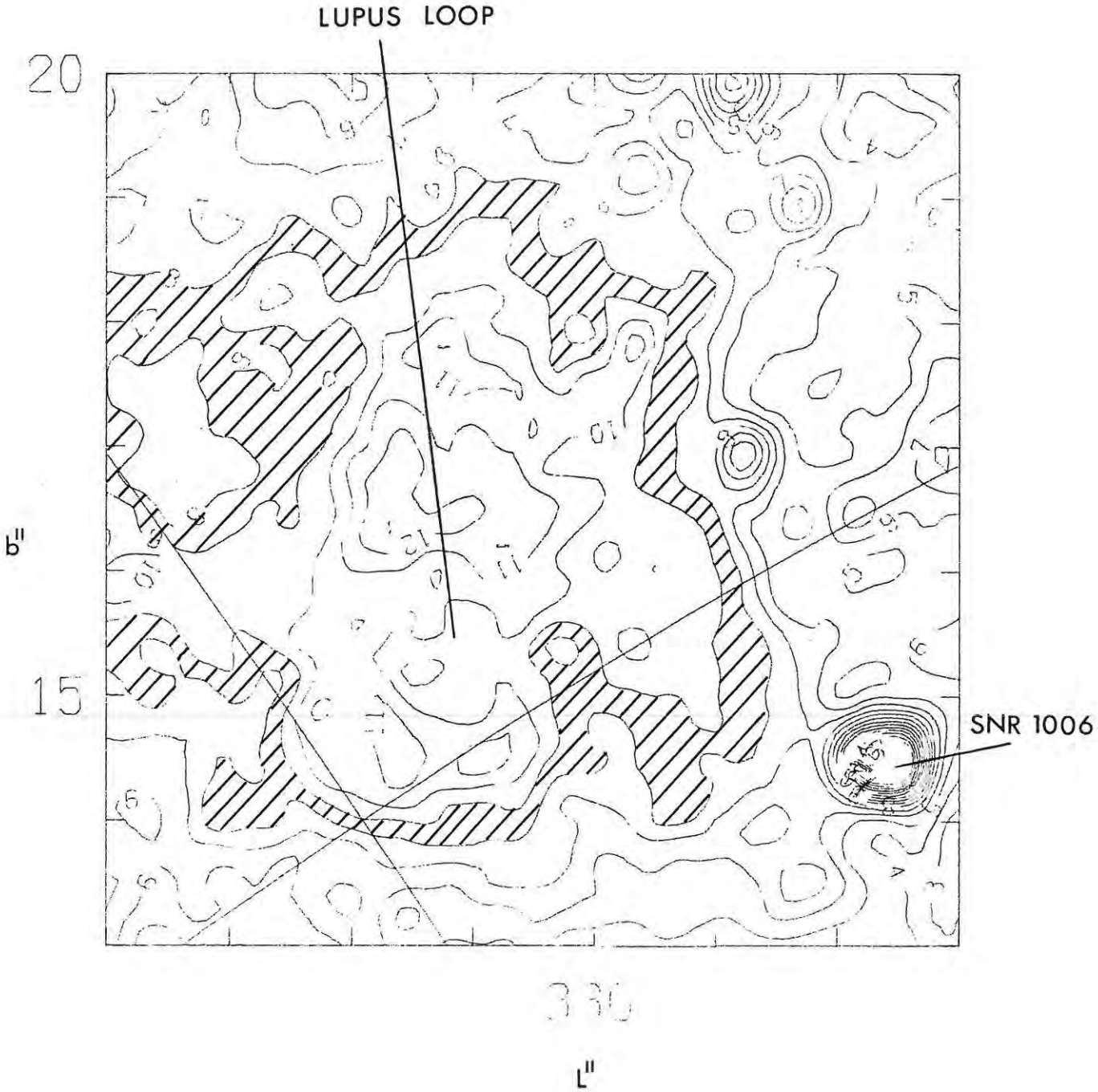
LUPUS LOOP
20
15
b"
SNR 1006
330
l"

Figure 7.5

Continuum spectrum of SNR 1006.

Point with error bars represents 2.3 GHz flux density.

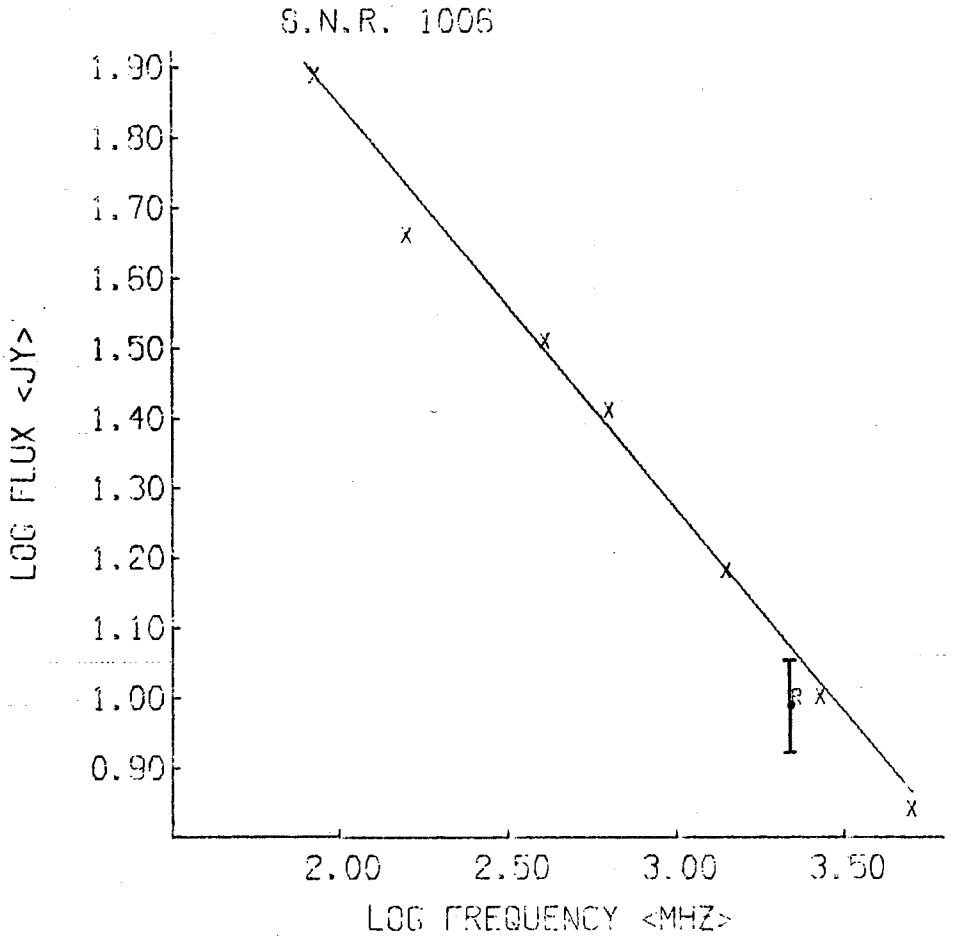
S.N.R. 1006
1.90
1.80
1.70
1.60
1.50
1.40
1.30
1.20
1.10
1.00
0.90
LOG FLUX <JY>
2.00
2.50
3.00
3.50
LOG FREQUENCY <MHZ>

PKS 1209-52, both having lobes of emission aligned with galactic longitude. The integrated flux density of the radiation at 2.3GHz was measured to be 9.9Jy, with error bounds of 15%. The source is superimposed on a very confused background, which makes a more accurate flux measurment very difficult. Figure 7.5 is a log-log plot of flux density versus frequency using the data listed by Milne (1971) and the 2.3GHz flux given above. A spectral index of -0.58±5% was calculated from these data, which agrees well with the value of -0.57 given by Milne.

iii) The Lupus Loop

The arc of emission associated with the Lupus supernova remnant is shown in figure 7.4. The subtraction of the gradient due to the Galactic disc emission shows up a plateau of emission on which the loop is superimposed. This plateau is also evident in a similar map at 635MHz by Milne (1971). An X-ray survey of the area shows an extended feature which co-incides with the radio structure (Riegler et al 1980). No optical counterpart has been detected. Two concentric expanding neutral hydrogen shells centred on the Lupus Loop have been found (Colomb and Dubner 1982).

By comparing integrated fluxes at four different frequencies Milne (1971) calculated a spectral index of -0.38 for the Lupus Loop complex. This value is representative of all the emission from the area, including the plateau. The integrated flux at 2.3GHz has not been calculated because of the background confusion. Milne's 635MHz map has approximately the same resolution as the map in figure 7.4, so antenna temperatures may be compared to obtain spectral indices. By measuring the antenna temperatures of the loop components above the extended plateau an average spectral index of -0.7±10% was obtained. The discrepancy in the spectral indices calculated from integrated flux and antenna temperatures indicates that the plateau may

be due to thermal radiation with a spectral index of about -0.1. The co-incidence of the plateau and the loop suggest that they are both associated with the remnant. The thermal emission could originate from a region of the gaseous shell of the remnant ionized by early stars in the Scorpio-Centaurus association.

7.3 The Sco OB2 and Scorpio-Centaurus stellar associations

In a previous survey Baart et al (1980) surveyed the region around the Sco OB2 association at 2.3GHz. Part of their map coincides with a section of the map in figure 7.6. All of the features pointed out by Baart et al are evident in the new data and will not be discussed further.

The subtraction of the galactic disc radiation shows up a large area of emission extending from 319^{o} to 345^{o} longitude and between 12^{o} and 22^{o} latitude. The H-alpha plates of Sivan (1974) show a corresponding low brightness feature. This area encloses stars of the Sco-Cen association of B-type stars (Bertiau 1958, Gutierrez-Moreno and Moreno 1967, Petrie 1961). These stars and associated interstellar gas form part of the Gould Belt, a local Galactic feature. Assuming the emission is due to thermal radiation from gas ionized by the B-stars, a lower limit may be placed on the ionizing (Lyman continuum) flux from these stars. The integrated flux density of the large emission feature was measured to be 500Jy ± 50%. The large error margin results from possible inaccuracies in the base surface subtraction.

We digress here to derive formulae which will allow the calculation of physical parameters of the ionized region.

Physical parameters of an optically thin HII region

The brightness temperature of the continuum radiation due to free-free emission from an optically thin HII region may be expressed as

$$T_b = \tau_c T_e \qquad 7.3.1$$

T_e is the electron temperature of the region and τ_c is the optical depth. The continuum flux received from such a source is

$$S_\nu = \frac{2k}{c^2}\lambda^2 \iint_{source} T_b \, d\Omega$$

$$= \frac{2k}{c^2}\lambda^2 \iint_{source} \tau_c T_e \, d\Omega \qquad 7.3.2$$

where ν is the observing frequency in Hz. The optical depth of the ionised hydrogen is given by the following equation (Mezger and Henderson 1967)

$$\tau_c = 8.235 \times 10^{-2} \times T_e^{-1.35} \times \nu^{-2.1} \times E \qquad 7.3.3$$

where: ν is in GHz

$E = \int_0^\iota N_e^2 \, dz$, N_e being the electron number density assuming there is only hydrogen in the nebula.

ι is the physical depth of the nebula along the line of sight. A correction factor has been omitted from the original equation since it is very close to unity. Substituting equations 7.3.1 and 7.3.3 into equation 7.3.2 results in

$$S_\nu = 2.5263 \times 10^3 \times T_e^{-0.35} \times \nu^{-0.1} \times N_e^2 \times V \times D^{-2} \qquad 7.3.4$$

where: S_ν is in Janskys

V is the volume of the ionised region in pc^3

D is the distance to the nebula in pc

Given the flux density, electron temperature, volume and distance of the HII region the average electron number density may be found by re-arranging equation 7.3.4

$$N_e^2 = 3.9583 \times 10^{-4} \times S_\nu \times \nu^{0.1} \times T_e^{0.35} \times D^2 \times V^{-1} \qquad 7.3.5$$

The ionising Lyman continuum flux required to maintain the HII region is given by

$$L_c = \text{no. of electrons X no. of ions X recombination rate}$$
$$= V \times N_e^2 \times (\beta - \beta_1) \qquad 7.3.6$$

$(\beta - \beta_1)$ is the total recombination rate to all levels except the ground state, since a transision to this level would emit a photon capable of ionising another hydrogen atom. This recombination rate is given by (Mezger and Henderson 1967)

$$(\beta - \beta_1) = 1.2029 \times 10^{46} \times T_e^{-0.8} \quad (pc^3 s^{-1}) \qquad 7.3.7$$

Combining equations 7.3.5, 7.3.6 and 7.3.7 results in an expression for the Lyman continuum flux

$$L_c = 4.7613 \times 10^{42} \times S_\nu \times D^2 \times T_e^{-0.45} \times \nu^{0.1} \qquad 7.3.8$$

which agrees with the formula given by Rubin (1968). Note that the derivation I have put forward here does not make any assumptions concerning the shape of the ionised region, only its volume. Assuming an electron temperature of 10 000K and an observing frequency of 2.3 GHz the Lyman continuum flux is

$$L_c = 8.2016 \times 10^{40} \times S_\nu \times D^2 \qquad 7.3.9$$

The distance to the Sco-Cen association is 170pc (Clube 1967) which, when substituted into equation 7.3.9 together with the measured flux density, results in a Lyman continuum flux of 1.2×10^{48} photons/sec. Taking into account the error bounds on the flux density, a lower limit of 6×10^{47} photons/sec is obtained for the ionizing flux from the stars of the association. It is not possible to calculate the expected Lyman flux from the Sco-Cen stars because they are all later than B2 and there are no reliable values for the Lyman flux from such stars. The distinct gap between the SCO OB2 emission and the SCO-CEN emission suggests that both the

HII regions are ionization bounded, assuming both associations are in the same gas cloud.

7.4 Loop and Filamentary Structures

The current view of the inter-stellar medium is that it consists of hot, tenuous gas with energy input from supernova explosions (McKee and Ostriker 1977, Salpeter 1978, McCray and Snow 1979). This theory is well supported by experimental evidence. The Galactic radio emission shows many loop structures in both continuum radiation (Haslam et al 1971) and HI (Heiles 1979). The presence of filaments has been suggested though not observed. Four large continuum loops (loops I to IV) have been studied extensively to determine their origin (Berkhuizen et al 1971, Spoelstra 1973). Their surface brightness to linear diameter ratio suggests that they are due to local supernova remnants (Berkhuizen 1973). Weaver (1978) postulates that supernova remnants and large bubbles driven by stellar winds are common features of the galactic disc. Heiles (1979) comments on the filamentary nature of the HI emission from the Galaxy. Brand and Zealey (1975) point out the loop and filamentary structure evident in the H-alpha and dust cloud distribution. They postulate that the loops are due to supernovae and stellar winds driving material out of the plane of the Galaxy. The filamentary structure arises when the material falls back to the plane.
All observations point to a turbulent interstellar medium with a filamentary rather than regular structure.
The grey scale image of the 2.3GHz continuum emission in figure 7.6 clearly shows many filamentary features. This would seem to be the first time they have been detected from their radio continuum radiation. The subtraction of the background disc emission enhances these features, especially those

closer to the plane. The overlay associated with this figure indicates features which are listed below. Only the brightest and most obvious features have been selected. Any optical counterparts or previous identifications are indicated.

A Two intersecting loops in the direction of the galactic centre.

B Arc of emission, centre at $l = 352.5^{o}$ $b = 4^{o}$, diameter 4^{o}.

C Emission associated with Sco OB2 association: RCW 129, S9 (Baart et al 1980).

D Part of a spur extending from the plane (Baart et al 1980, Haslam et al 1981).

E Filament, possibly part of an arc. Sharp minimum along inner edge.

F Faint arc corresponding to RCW 114 (Rodgers et al 1960).

G Bright arc, no optical counterpart.

H Large faint loop.

I Complex filamentry and loop structure.

J Large area of emission associated with the Sco-Cen association.

K Lupus Loop (see section 7.2).

L Two intersecting arcs.

M Faint filament.

N Small arc.

O Part of very large faint loop.

P Loop close to plane.

Q Faint filamentary structure, possibly part of a large loop (Haslam et al 1981).

R Faint filamentary region.

S Narrow arc of emission, possibly related to the Coalsack region.

T Large scale filamentary structure, weakly aligned with the local

magnetic field (solid lines, Mathewson 1968).

Note that these features cannot be residual scanning effects. They do not extend radially from the celestial pole and they occur on all eight independent rasters. They are also well above the noise level of the data. The limited dynamic range of the photographic print tends to reduce the contrast between these features and their surroundings, but they are more clearly visible on the photograph than on an ordinary contour map.

Many of these features may be associated with ionised hydrogen clouds, but no corresponding H-alpha emission is detected because of the severe optical obscuration near the plane. There are no obvious correlations between the above continuum features and the local HI features investigated by Cleary (1977). The 408MHz survey (Haslam 1982) does not show up the unidentified features because of the lower resolution and the unsuitability of contour maps for showing faint filamentary structures.

It would be very difficult to measure the continuum flux of the filaments because of the large degree of confusion. Radial cross-sections of the filaments could be used to obtain a surface brightness, but no corresponding data at another frequency are available to investigate the continuum spectra. It is thus difficult to determine the radiation mechanism of the un-identified features. Observations with a similar resolution and sensitivity, but different frequency are required to calculate the spectral indices of the filaments. These indices could be used to determine whether the filaments are due to a thermal or non-thermal mechanism.

The high latitude filaments are most probably due to local features extending out of the galactic plane. If these extensions are due to supernova explosions, then the observed radiation would be due to the synchrotron radiation of the supernova remnant. For this case the filaments

should be aligned with the magnetic field. Only the filaments of feature T seem to be aligned with the local magnetic field as determined by Mathewson (1968). It is most probable that this is the only feature affected by the local magnetic field. The other features are probably more distant than the field mapped by Mathewson.

If the filamentary emission features are of thermal origin then two questions must be asked: how did the matter get out of the plane and what is the source of the ionizing flux. Stellar winds of early type stars or supernova explosions could be responsible for blowing the matter out of the plane. The ionizing Lyman continuum flux could come from nearby OB associations or from OB associations formed in the ejected matter (Elmegreen and Lada 1977, Herbst and Assousa 1977).

Whatever emission mechanisms are responsible for the filaments, the observations support the theory of a turbulent interstellar medium.

Figure 7.6

Grey scale image of residual data after the subtraction of the base surface of figure 7.2. Features discussed in the text are outlined. Lines on south side of the plane show the direction of the local magnetic field.

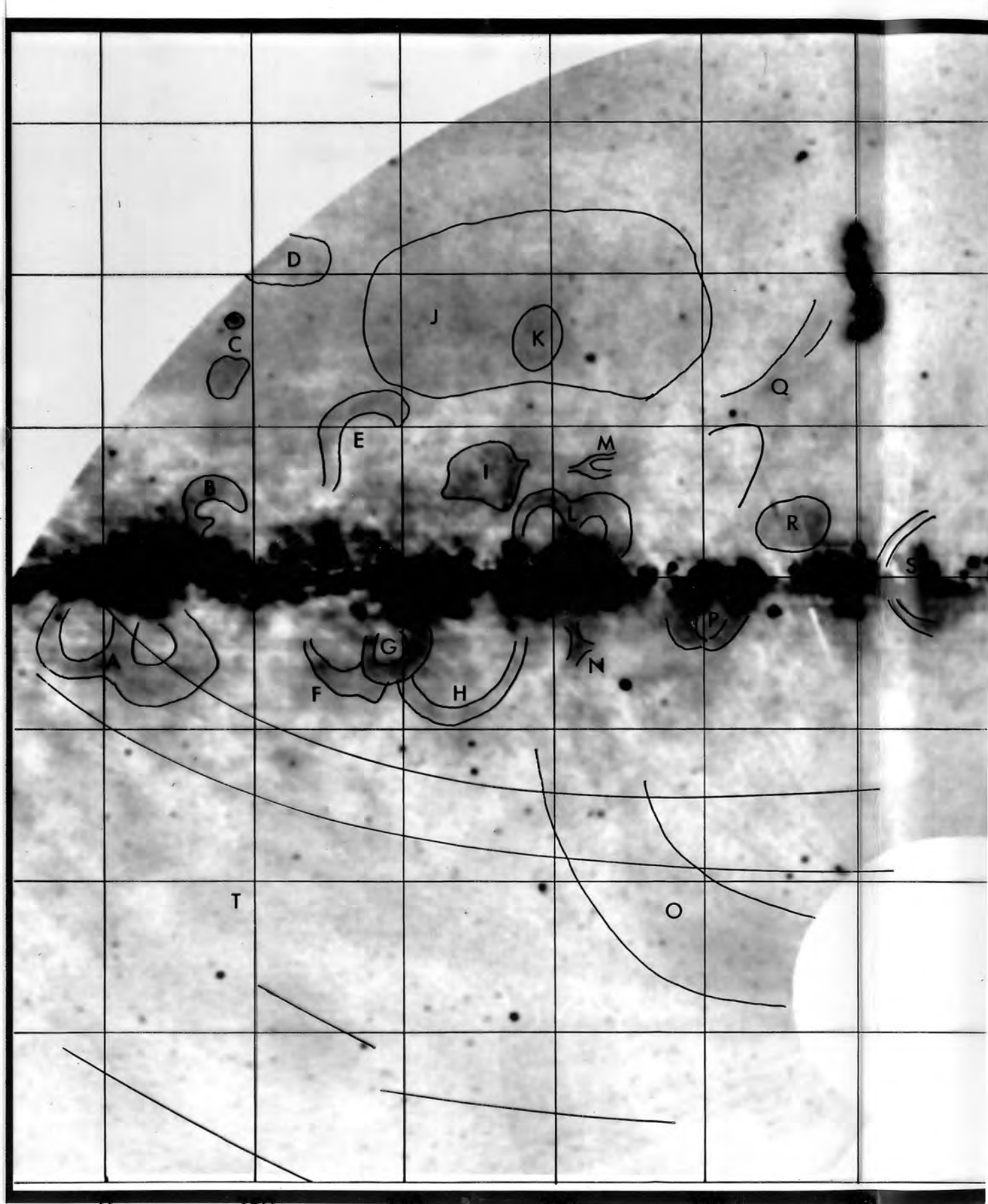
30
20
10
0
-10
-20
-30
-40
LAT.
0
350
340
330
320
310
LONG.
A
B
C
D
E
F
G
H
I
J
K
L
M
N
O
P
Q
R
S
T

CHAPTER 8 EXTRA-GALACTIC ASTRONOMY

With the relatively low resolution of the 26m antenna at 2.3GHz it is not possible to map the radio brightness distribution of most extragalactic radio sources, because of their small angular size. They appear as very compact sources on the survey maps, many of them being effective point sources. Even though the structure of the sources cannot be resolved, useful information about the extragalactic sources can be gained from the survey data, as discussed below.

The integrated flux density of a source may be measured if it is not confused with other sources. If the source has angular dimensions comparable with the antenna beamwidth then the source will be seen to be extended on the survey map. Extragalactic objects sometimes have low brightness tails or jets which have relatively large angular dimensions, and these might be detected. These extended objects would be good candidates for investigation using higher resolutions. Comparisons of surveys done at different times may show up variable sources.

Centaurus A is the strongest and largest extragalactic feature on the map and its large scale structure is resolved. For this reason it is examined in closer detail than the other sources. All the smaller sources which are not confused in the galactic emission and which have integrated flux densities greater than 0.5Jy are listed. Possible extended emission is indicated in the list.

8.1 Centaurus A

The large area of emission at about 13h30m right ascension and -42^{o} declination is associated with the radio galaxy NGC 5128, or CEN A. This is an E0 type galaxy with a distinct dust lane about its equator. The distance to NGC 5128 is 4Mpc and it has an absolute magnitude of -20.8 (Sersic 1958).

The radio emission extends from 13h11m to 13h37m right ascension and -37.5 to -47.0 degrees declination. This corresponds to a linear extent of 340kpc by 660kpc. The emission feature is made up of a strong central peak and extended lobes to the north and south. The central peak is actually two sources which are not resolved in the map (Cooper et al 1965). Unfortunately the antenna temperature of the central peak is greater than 30K and is thus truncated because of the D.V.M. overflow problem.

The integrated flux density of the entire source at 2.3 GHz was measured to be 936Jy with an error of 10%. The measured flux density is a lower estimate because of the truncation of the central peak. Figure 8.1 compares this value with flux densities at 408MHz, 960MHz and 1428MHz given by Cooper et al (1965). A spectral index of $-0.60 \pm 5\%$ was calculated from the four values, which compares well with their value.

The 960MHz map of Cooper et al has the same resolution as the 2.3GHz map. The peak brightness temperatures of the northern and southern lobes at the two frequencies were compared to obtain approximate spectral indices for the two structures. Values of -0.84 and -0.68 were calculated for the northern and southern lobes respectively. The error limit on these values is 15%. This error includes a factor introduced by the fact that the 2.3GHz brightness temperatures were not corrected for polarization. The emission must be due to the synchrotron mechanism. The different spectral indices obtained for the two lobes implies that the electron energy distribution is probably different for the two lobes.

Figure 8.1

Continuum spectrum of Centaurus A.

2.3 GHz flux has error bars.

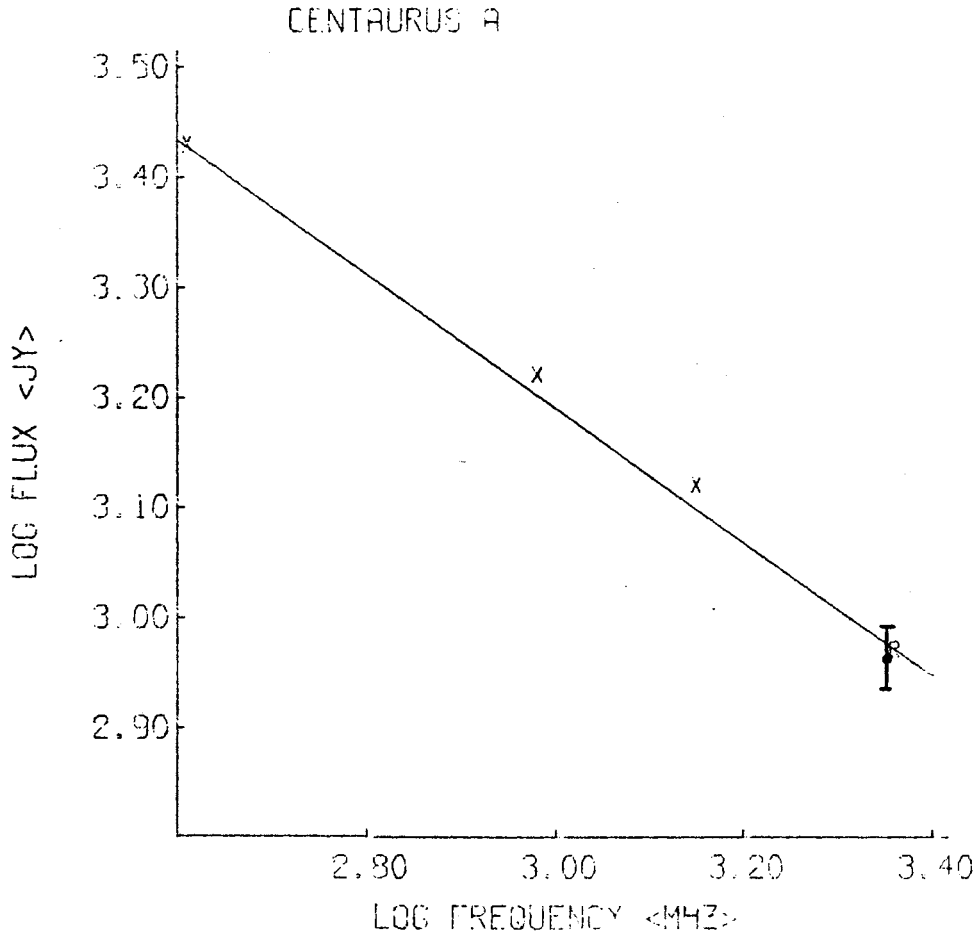
CENTAURUS A
3.50
3.40
3.30
3.20
3.10
3.00
2.90
LOG FLUX <JY>
2.80
3.00
3.20
3.40
LOG FREQUENCY <MHZ>

8.2 Other Extra-galactic Sources

No other extra-galactic emission features in the map are well resolved. All known and possible extra-galactic sources which are not confused and have flux densities greater than 0.5Jy are listed below. The fluxes were measured using program FLUX discussed in chapter 5. The following sources were used for calibration purposes (Nicolson, private communication):

Source	Assumed 2.3GHz flux density (Jy)
1215-45	3.48
1302-49	5.15
1827-36	3.53
1932-46	7.68
2104-25	7.86
2150-52	2.38

The peak error for the measured fluxes is 0.2 Jy, corresponding to an error of 20mK in the baseline determination.

Table 8.1 is a list of the detected sources which have been identified in the Parkes catalogue (Ekers 1969 and others), together with their optical identifications. The abbreviations used for the optical identifications are those used in the Parkes catalogue and are given below.

D	spherical galaxy with diffuse envelope
db	dumb-bell or double galaxy
E	elliptical galaxy
g	galaxy, too faint to classify
N	compact galaxy
S	spiral galaxy; SO elliptical with dust lane
Q	quasi-stellar object
Q?	possible quasi-stellar object
II	several galaxies within uncertainty of radio position
III	nothing above plate limit
IV	obscured field

The contour map of each source (see appendix) was examined in order to detect any possible extended structure associated with the source. The remarks next to some of the sources indicate sources with possible extended features.

Table 8.1

Source	Optical ident.	2.3GHz flux density	Remarks
1215-45	III	3.75	Two tails to north-west
1221-42	db	1.75	
1232-41	E	1.47	
1233-24	Q	1.80	
1243-444	III	0.64	
1244-255	Q	0.75	
1245-41	E	1.89	NGC 4696 Tail to west
1251-289	E	0.51	
1302-49	S	4.90	
1313-333	Q	1.59	Tail to west?
1330-328	Q	1.72	
1333-33	E	12.78	Three resolved sources in Parke's catalogue IC4296
1334-29	S	2.47	
1346-39	III	0.57	
1355-41	Q	2.21	
1416-49	II	0.54	
1420-27	Q	1.80	
1421-38	Q	1.35	
1421-49		6.03	
1424-41	Q	2.01	
1451-364	E	2.54	
1519-294	III	1.39	
1519-273	Q	1.42	
1550-269	III	1.49	
1610-60	E	33.06	Extended
1733-56	g	6.69	
1737-60	III	1.59	
1740-517	III	4.57	
1754-59	III	2.01	
1806-458	III	1.66	
1814-51	III	1.84	
1827-36	III	3.48	
1839-48	?	1.72	
1840-40	III	1.03	
1921-293	Q	6.99	OV 236
1929-397	E	1.50	
1932-46	III	7.67	
1933-400	Q	1.64	
1933-58	III	1.64	
1950-613	Q	1.65	
1951-50	II	1.40	
1953-42	III	2.44	
1954-38	Q	1.55	
1954-55	E	3.56	
1955-35	II	1.38	
2002-50	III	0.92	
2005-489	N	0.71	
2009-52	III	1.51	
2020-57	II	1.56	

2032-35	III	4.54	
2040-26	E	0.57	
2052-47	II	1.86	
2058-28	E	3.69	Tails to north-east and south
2058-425	Q	1.49	
2104-25	E	8.24	
2106-413	III	2.89	Extended to north-east and south-west
2115-30	Q	1.13	
2130-53	II	1.25	
2140-43	III	1.69	
2149-28	III	1.61	
2150-52	III	2.64	
2158-380	E	0.93	

All sources in the Parkes catalogue with interpolated fluxes at 2.3 GHz greater than 0.5Jy were detected and appear in the above list.

A number of sources were detected but not identified in the Parkes catalogue, but appear in the Molonglo catalogue (Large et al 1981). These are listed in table 2 below.

Table 8.2

Co-ordinates R.A.	Dec.	2.3GHz Flux density (Jy)	Molonglo catalogue
12 35 00	-50 36 35	2.68	1235-506
12 45 48	-45 46 33	1.45	1245-461
13 52 24	-51 59 27	0.71	1352-520
13 58 48	-49 16 41	1.69	1358-493
14 32 18	-48 11 34	1.47	1431-481
14 52 30	-51 50 35	0.95	1452-517
14 58 06	-39 06 19	1.59	1458-391
15 27 06	-42 26 06	2.90	1526-423
16 13 36	-58 39 54	1.72	1613-586
17 23 12	-55 30 44	4.18	1722-554
18 17 30	-39 12 14	1.92	1817-391

These sources are too close to the galactic equator to be included in the Parkes survey.

CHAPTER 9 DISCUSSION OF METHOD AND RESULTS

The initial results from the sky survey program have shown that the method is capable of producing good data. The observation technique and data reduction processes are improved as experience in sky mapping is gained. Latent problems in the system become apparent after the production of a number of maps. Changes also occur due to the introduction of new equipment and more sophisticated processing requirements. This chapter briefly outlines changes and improvements which have been implemented by the author, and introduces proposed modifications. Most of the proposed changes are the result of the introduction of additional computing power, i.e. a CDC 825 mainframe replacing the ICL 1904, and the purchase of a VAX 11/730 super-minicomputer for departmental use. Data processing techniques which were attempted but not implemented are also discussed.

Section 9.3 discusses the results presented in chapters 7 and 8.

9.1 Observing Procedure and Hardware

9.1.1 SKYMP

The basic method of observation has not been changed as yet. Observations done since the third map have employed current observing coordinates, rather than coordinates precessed from 1950. This change was made after the problem of inconsistent background profiles due to the diurnal precession variation was discovered.

A minor change was made to SKYMP, the observing program, which allows it to read the parameters for observations from a disc file. This file contains a schedule of parameters for the current set of observations. The parameters for an observation are accessed using the observation number, which is

supplied by the operator. This modification made it possible for the R.A.O. staff to run the mapping program. The schedule file is kept up to date by Rhodes astronomers.

Further changes were made to SKYMP which improve the operator interface and perform checks to see whether the observing hardware is working and conforms to minimum specifications. These additions ensure that no telescope time is wasted due to operator errors, or running SKYMP when the hardware is not performing properly. The improvements are listed below.

i) Computer control of noise tube and D.V.M. inputs.

ii) Radiometer consistency checks.

iii) Magnetic tape integrity test.

iv) Power failure checks.

v) Matching the allowed antenna settling time to the servo integrator time constant.

vi) Alternate observing program initiation if SKYMP aborts.

In order to reduce problems of bad antenna tracking and inconsistent terrestrial background contributions, some thought has been given to modifying the observing method to a constant hour-angle scanning technique. Such a method (NOD) has been used for other large area mapping observations (Haslam et al 1981). The implementation of this technique will involve large changes in the initial reduction processes, but the changes to SKYMP will be minimal. No firm decision has been made on whether to make this change or not, as yet.

Small Area Mapping

A version of SKYMP has been adapted to map small areas of sky. This program, BEAMP, facilitates the mapping of small areas of interest. An area of 6^{o} by 6^{o} may be mapped in one night with a scan spacing of 0.8 degrees and a scan

rate of 0.15 degrees/second. Five repeats of each raster are obtained. Using a smaller scan spacing and a corresponding smaller declination bin size allows the data to be Fourier filtered more effectively because less noise is aliased into the data. Very good sensitivity is obtained because of the many repeats of each raster, and the slower scan rate. BEAMP automatically repeats the observations of the area, each observation being eqivalent to a normal SKYMP observation, but much shorter. Successive observations are made at increasing hour-angles as the area to be mapped progresses from East to West at the sidereal rate. The data for all of the observations are written to a single magnetic tape, which simplifies the initial reduction of the data. Further simplifications in the reduction process are possible because of the small volume of data and negligible drift effects over such short rasters.

9.1.2 The Antenna Control

The antenna control programs have had minor corrections and modifications made to them by the observatory staff, but their basic operation is still the same. The telescope pointing correction function used by COMND needs to be updated, especially for southern declinations.

The antenna control programs COMND and STEER use a major share of the control computer's resources. The observing programs, such as SKYMP, have to share these resources, and so the programs have to be limited in size and execution time. In order to relieve the computer of the burden of closing the antenna servo feedback loop a project is in progress to implement a micro-computer controlled servo system. This will be a multi-processor system which should provide improved antenna control and protection.

9.2 Data Processing

9.2.1 The Initial Processing

Only one major change has been made to the initial reduction process. An initial background profile is subtracted from the data in small declination bins produced by TABN, the reformatting and binning program. This addition was made to reduce unwanted gradients in the data, which affected the calculation of the medians for the large declination bins used for the calculation of the 'drift'. The large 'drift' and 'background' bins are now created from the data in the small bins with the background profile subtracted.

Because the variations in the maser gain may have a number of causes, the predicted drift due to changes in the maser gain is no longer subtracted from the data. Each different cause of gain variation has a different effect on the noise temperature of the receiver system. Thus without knowing the cause (or causes) an exact compensation is not possible. These causes of gain drift have been investigated extensively by the R.A.O. staff, and have been removed or reduced to have negligible effect (less than 1dB peak diurnal variation).

The replacement of the existing ICL computer by a new CDC machine will hopefully speed up and simplify the current reduction method. The increased computing power should also allow improvements to be made to the current reduction system. Experience in the new machine must be gained before these changes are implemented. The purchase of the VAX mini-computer, which will include a tape deck and plotter among its perepherals, will allow observation data tapes to be verified quickly, using programs similar to those already in use at the observatory, and described in chapter 2. It may, in fact, prove easier to perform the entire data reduction on the VAX

computer, due to the interactive and operator intensive nature of the task. If the NOD scanning system is implemented, the existing data reduction programs will have to be updated. The existing programs may be modified to handle the new data, but in order to take full advantage of the observing method a new reduction process would have to be developed.

9.2.2 Image Processing

The author attempted to implement various non-linear image enhancement techniques, but no working, two-dimensional implementations were developed. The method given the most attention was the Maximum Entropy Method, or MEM. A one-dimensional implementation of Gull and Daniell's method for images (Gull and Daniell 1980) was developed, but deficiencies in their method were noticed (Jonas 1980) and the extension to two-dimensions was not attempted. Bryan and Skilling also noticed these inadequacies and improved the method (Bryan and Skilling 1980). An algorithm to implement this method was sought, but no stable solution could be found. While attempting to produce a one-dimensional solution it became apparent that a full solution would require more computer resources than those which were available at the time, and so the work was stopped completely. With the arrival of the two new computers this work may be restarted. The CDC mainframe should have ample speed for the execution of a working MEM program. In addition STARLINK, a system of astronomy programs written for the VAX computer, has Bryan and Skilling's MEM program in its libraries. If STARLINK is installed on the Physics Department's VAX, it will be a simple matter to evaluate the suitability of the Maximum Entropy Method for enhancing survey data.

One section of STARLINK is dedicated to image processing and therefore there should be no need for duplicating the image processing programs, discussed in chapter 5, on the VAX. The locally developed programs are very similar

to those available on the STARLINK system, and it will be possible to have equivalent programs running on both the CDC and the VAX computers. The ICL assembly language routines will have to be rewritten in COMPASS, the CDC assembly language. The larger main memory and faster execution speed of the CDC will make the processing of large data sets much easier and quicker, using the current programs modified to run on the new machine.

9.2.3 Image Display

A quick and effective means of displaying the map data has always been a problem. The large volume and large dynamic range of the data requires high resolution both spatially and in 'depth'. The solution to this problem would be a medium resolution grey-scale or colour video graphics system. Various attempts by the author and others to provide a video display of the data met with little success. A number of commercial colour graphics systems are available, but most of these are too expensive for consideration.

At present a few of the reasonably priced systems are being considered. All of these systems are readily interfaced to the VAX computer. If STARLINK is implemented on the computer then a software driver will be developed for the video display device so that it may be used with the STARLINK software.

9.3 The Results

The results of the second part of the 2.3 GHz survey contain a wealth of information. The most obvious emission features have been discussed in this thesis, but there is still a lot of scope for further work on this set of data.

Relatively large areas of emission, such as the Lupus Loop and the emission from the Sco Cen area, are easily detected in the data. The exact extent of these extended sources may be measured because they are contained completely

within the bounds of the surveyed area. Three emission features due to well known supernova remnants were studied and compared to previous results. The new results were consistent with with the previous observations. The emission from the Lupus Loop appears to have both a thermal and a non-thermal component, possibly indicating that the neutral shell of gas around it is being ionized by nearby early stars.

The galactic disc emission has been shown by the map to extend to high latitudes, beyond 40^{o} at zero longitude. This emission appears to be due to the synchrotron mechanism, and is thus non-thermal. The profile of the disc emission along the Galactic equator shows definite steps, which are consistent with the results of Phillipps et al. These steps are also due to a non-thermal mechanism.

The most striking feature of the data is its filamentary structure. No other large area radio continuum survey has had sufficient resolution to show up the filamentary nature of the galactic emission. The filaments are most probably local features because they occur at latitudes well away from the disc. It seems most likely that the filaments and loops are the result of some violent events in the disc which eject matter out of the plane. As yet it is not possible to deduce whether the emission mechanism is thermal or non-thermal because of the lack of data at another frequency. Only the very largest of these features appears to align with the local Galactic magnetic field. This could mean that the other features occur outside the range of this field, but are aligned with their own local field.

Flux densities for all non-confused extragalactic sources with flux densities greater than 0.5Jy were measured. Most of these were identified in the Parkes catalogue. Of those which were not identified one was extended, and the others were too close to the plane to be included in the Parkes survey. Some of the sources seem to have extended structures

associated with them. These could be radio jets, which have been observed for many galaxies, or just confusing sources.

The results have shown that the observation method is reliable, and that there is good reason for continuing the 2.3 GHz survey. As more parts of the survey are completed it will be possible to detect larger emission features and obtain a better overall view of the Galaxy.

REFERENCES:

Baart,E.E., de Jager,G., Mountfort,P.I.: 1980, Astron. Astrophys. **92**, 156
Berkhuizen,E.M.: 1973, Astron. Astrophys. **24**, 143
Berkhuizen,E.M., Haslam,C.G.T., Salter: 1971, Astron. Astrophys. **14**, 252
Bertiau,S.J.: 1958, Astrophys. J. **128**, 533
Blaau,A.: 1967, Annual Review of Astronomy and Astrophysics, Vol 2
Bracewell,R.N.: 1965, The Fourier Transform and its applications, McGraw-Hill
Brand,P.W.J.L., Zealey,W.J.: 1975, Astron. Astrophys. **38**, 363
Brenner,N.: 1976, The Fast Fourier Transform in **Methods of Experimental Physics 12C**, Academic Press
Brigham,E.O.: 1974, The Fast Fourier Transform, Prentice Hall
Bryan,R.K., Skilling,J.: 1980, M.N.R.A.S. **191**, 69

Cleary,M.N.: 1977, Local Galactic Structure, Ph.D. Thesis, Austalian National University
Clube,S.V.M.: 1967, M.N.R.A.S. **137**, 189
Colomb,F.R., Dubner,G.: 1982, Astron. Astrophys. **112**, 141
Cooper,B.F.C., Price,R.M., Cole,D.J.: 1965, Australian J. Phys. **18**, 589

Ekers,J.A.: 1969, Australian J. Phys. Suppl. **7**, 1
Elmegreen,B.G., Lada,C.J.: 1977, Astrophys. J. **214**, 725

Flanagan,C.S.: 1981, Reduction of Data by Removal of Galactic Disc Emission, Honours Project, Rhodes University

Gardner,F.F., Milne,D.K.: 1965, Astron. J. **70**, 754
Green,A.J.: 1974, Astron. Astrophys. Suppl. **18**, 267
Gull,S.F., Daniell,G.J.: 1978, Nature **272** ,686
Gutierrez-Moreno,A., Moreno,H.: 1967, Astrophys. J. Suppl. **15**, 459

Haslam,C.G.T., Kahn,F.D., Meaburn,J.: 1971, Astron. Astrophys. **12**, 388
Haslam,C.G.T., Klein,U., Salter,C.J., Stoffel,H., Wilson,W.E., Cleary,M.N., Cooke,D.J., Thomasson,P.: 1981, Astron. Astrophys. **100**, 209
Haslam,C.G.T., Salter,C.J., Stoffel,H., Wilson,W.E.: 1982, Astron. Astrophys. Suppl. **47**, 1
Heiles,C.: 1978, A New Class of Extraordinary HI Shell in **I.A.U. Symposium No. 84**
Heiles,C.: 1979, Astrophys. J. **299**, 533
Herbst,W., Assousa,G.E.: 1977, Astrophys. J. **217**, 473
Hill,E.R.: 1968, Australian. J. Phys. **21**, 735

Jonas,J.L.: 1980, **The Application of MEM to Image Processing** presented at the 25th annual conference of the S.A.I.P.

Kraus,J.D.: 1966, Radio Astronomy, McGraw-Hill
Kraus,J.D., Carver,K.R.: 1973, Electromagnetics, McGraw-Hill

Landecker,T.L., Wielebinski,R.: 1970, Australian J. Phys. Suppl. **16**, 1
Lane,A.P.: 1979, Publ. Astron. Soc. Pac. **91**, 405
Large,M.I., Mills,B.Y., Little,A.G., Crawford,D.F., Sutton,J.M.: 1981, M.N.R.A.S. **194**, 693

Mathewson,P.S.: 1968, Astrophys. J. Letters **153**, L47
Mezger,P.G., Henderson,A.P.: 1967, Astrophys. J. **147**, 471
Milne,D.K.: 1971, Australian J. Phys. **24**, 757
Mountfort,P.I.: 1981, Ph.D. Thesis ,Rhodes University (uncompleted)
McCray,R., Snow,T.P.: 1979, Annual Review of Astronomy and Astrophysics **17**
McKee,C.F., Ostriker,J.P.: 1977, Astrophys. J. **218**, 148

Nicolson,G.D.: 1965, Publ. Astron. Soc. Pac. **77**, 260
Nicolson,G.D.: 1970, IEEE T.M.T.T. **18**, 169

Papoulis,A.: 1962, The Fourier Integral and its Applications, McGraw- Hill
Petrie,R.M.: 1962, M.N.R.A.S. **123**, 501
Phillipps,S., Kearsy,S., Osborne,J.L., Haslam,C.G.T., Stoffel,H.: 1981a, Astron. Astrophys. **98**, 286
Phillipps,S., Kearsy,S., Osborne,J.L., Haslam,C.G.T., Stoffel,H.: 1981b, Astron. Astrophys. **103**, 405

Riegler,G.R., Agrawal,P.C., Gull,S.F.: 1980, Astrophys. J. **235**, L71
Rodgers,A.W., Campbell,C.T., Whiteoak,J.B., Bailey,H.H., Hunt,V.O.: 1960, An Atlas of H-alpha Emission in the Southern Milky Way, Mount Stromlo Observatory
Rubin,R.H.: 1968, Astrophys. J. **154**, 391
Rusch,W.V.T., Potter,P.D.: 1970, Analysis of Reflector Antennas, Academic Press

Salpeter,E.E.: 1978, Energy Balance in the Interstellar Medium in **I.A.U. Symposium no. 84**
Sersic,J.L.: 1961, Revta Univ. Nac. Cordoba **11**: No3
Shklovsky,I.S.: 1960, Cosmic Radio Waves, Oxford University Press
Sivan,J.P.: 1974, Astron. Astrophys. Suppl. **16**, 163
Spoelstra,T.A.Th.: 1973, Astron. Astrophys. **24**, 149

Terry,P.D.T.: 1978, Applied Mathematics Course Notes, Rhodes University
Tukey,J.W.: 1977, Exploratory Data Analysis, Addison Wesley

Wall,J.V.: 1979, Q. Jl. Astr. Soc. **20**, 138
Weaver,H.: 1978, Large Supernova Remenants as Common Features of the Disc in **I.A.U. Symposium No. 84**
Wells,D.C., Greisen,E.W., Harten,R.H.: 1981, Astron. Astrophys. Suppl. **44**, 363
Whiteoak,J.B., Gardener,F.F.: 1968, Astrophys. J. **154**, 807

Yates,K.W., Wielebinski,R., Landecker,T.L.: 1967, Australian J. Phys. **20**, 595

APPENDIX

Key to contour maps

Resolution of map data (HPBW): 0.40 deg.

Beam sensitivity: 11.38 Jy/K

Noise level:

Declination range	rms noise (mK)
-63 to -54	9.4
-55 to -44	10.4
-45 to -34	11.1
-35 to -24	11.7

Contour level table:

Contour label	T_a mK	Contour label	T_a mK
1	12	24	1000
2	25	25	1200
3	37	26	1400
4	50	27	1600
5	75	28	1800
6	100	29	2000
7	125	30	2500
8	150	31	3000
9	175	32	3500
10	200	33	4000
11	225	34	4500
12	250	35	5000
13	275	36	6000
14	300	37	7000
15	350	38	8000
16	400	39	9000
17	450	40	10000
18	500	41	12000
19	550	42	14000
20	600	43	20000
21	700	44	25000
22	800	45	30000
23	900		

1 K antenna temperature corresponds to 1.41 K full beam brightness temperature.

The grid lines on the maps represent Galactic longitude and latitude at 5^{o} spacing.

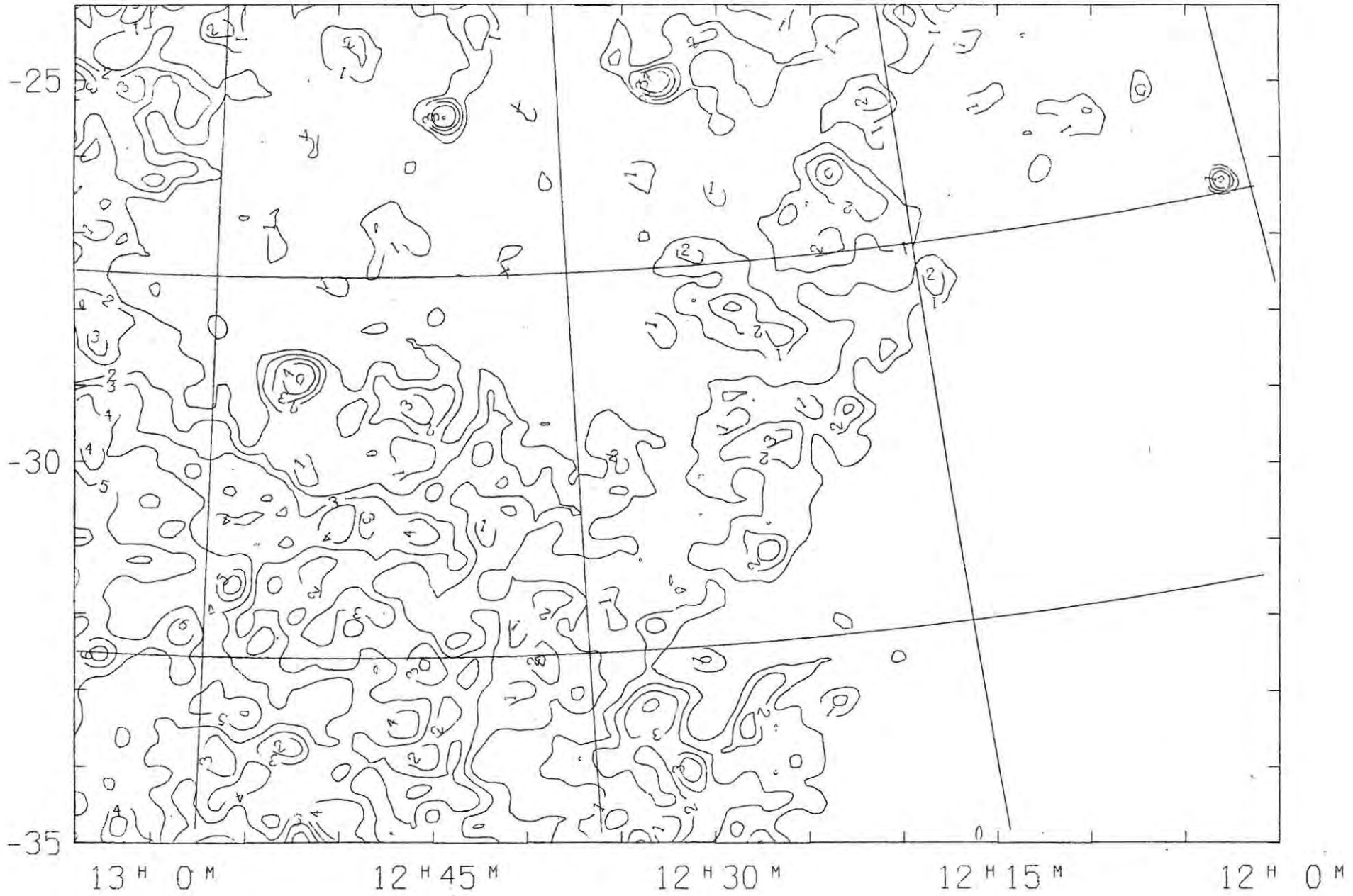
-25
-30
-35
13 H 0 M
12 H 45 M
12 H 30 M
12 H 15 M
12 H 0 M

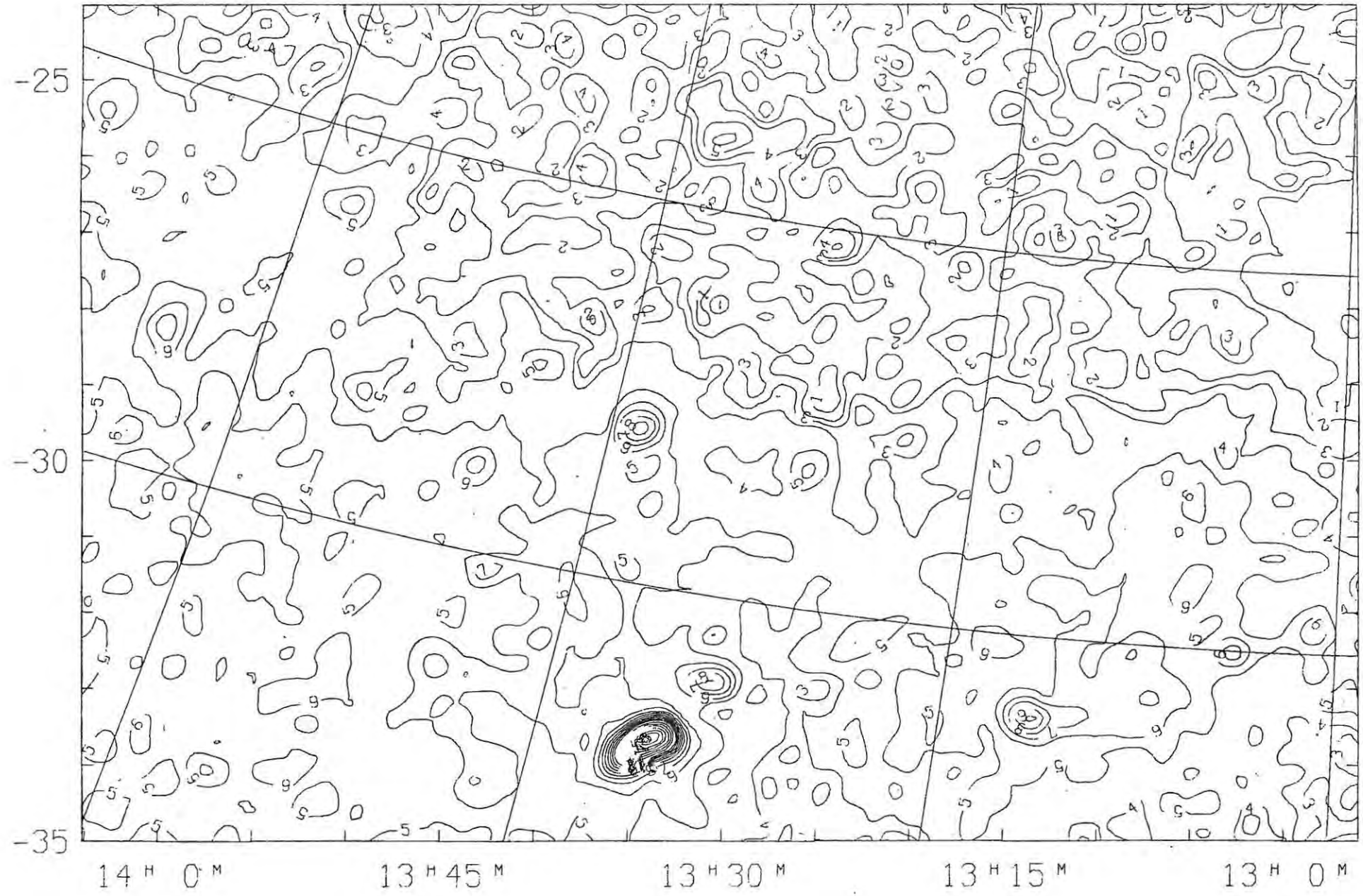
-25
-30
-35
14 H 0 M
13 H 45 M
13 H 30 M
13 H 15 M
13 H 0 M

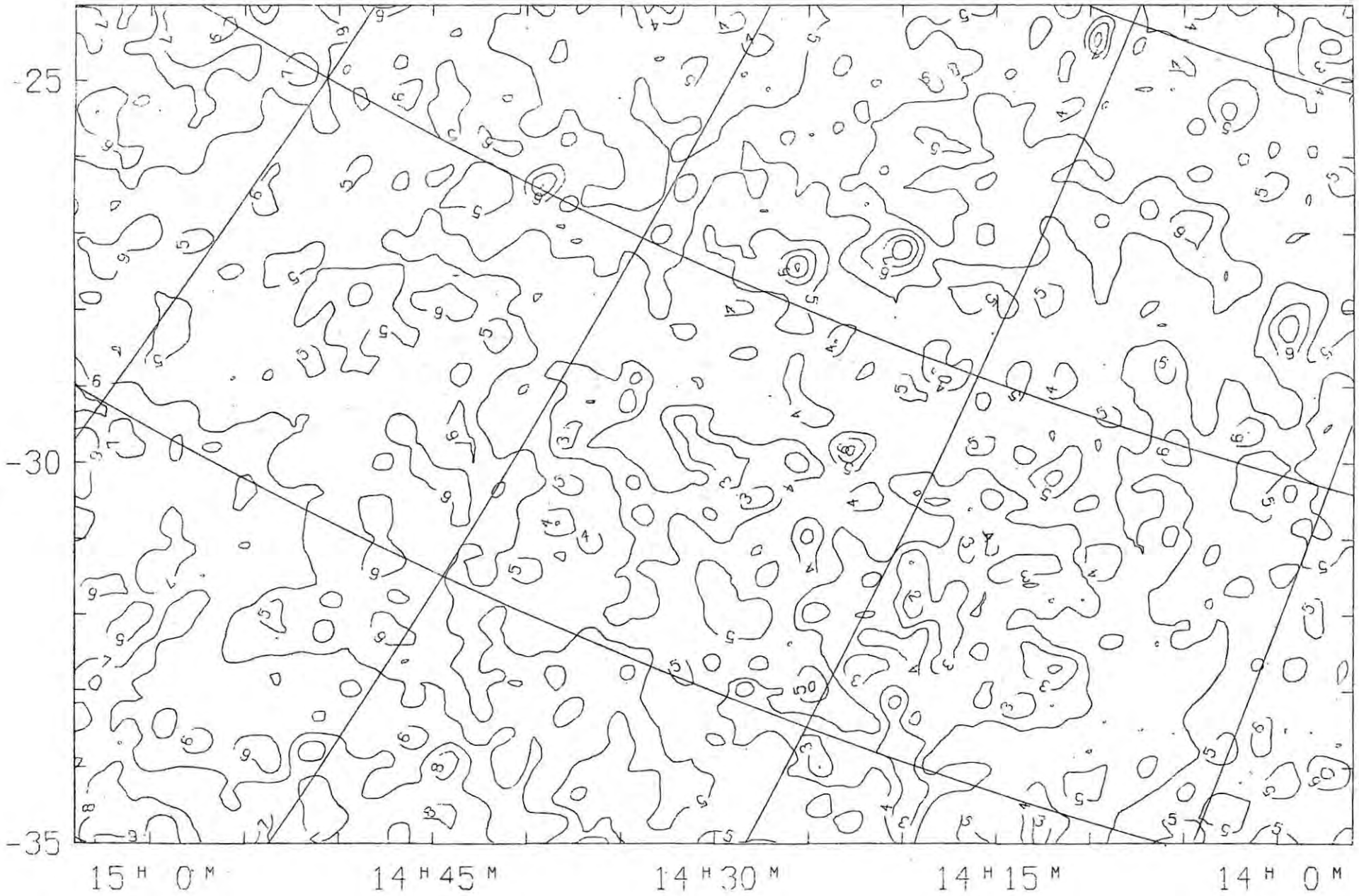
-25
-30
-35
15 H 0 M
14 H 45 M
14 H 30 M
14 H 15 M
14 H 0 M

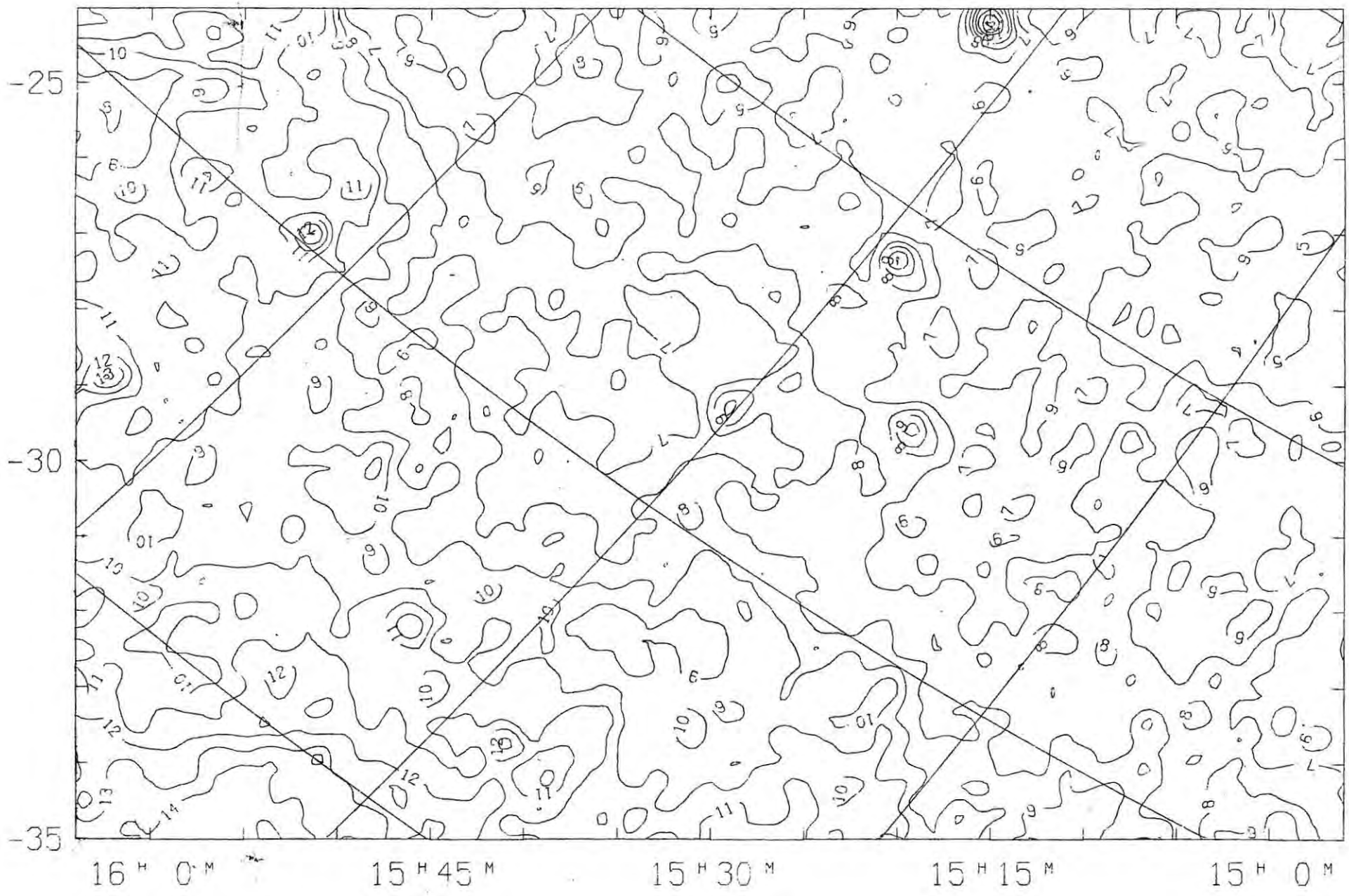
-25
-30
-35
16 H 0 M
15 H 45 M
15 H 30 M
15 H 15 M
15 H 0 M

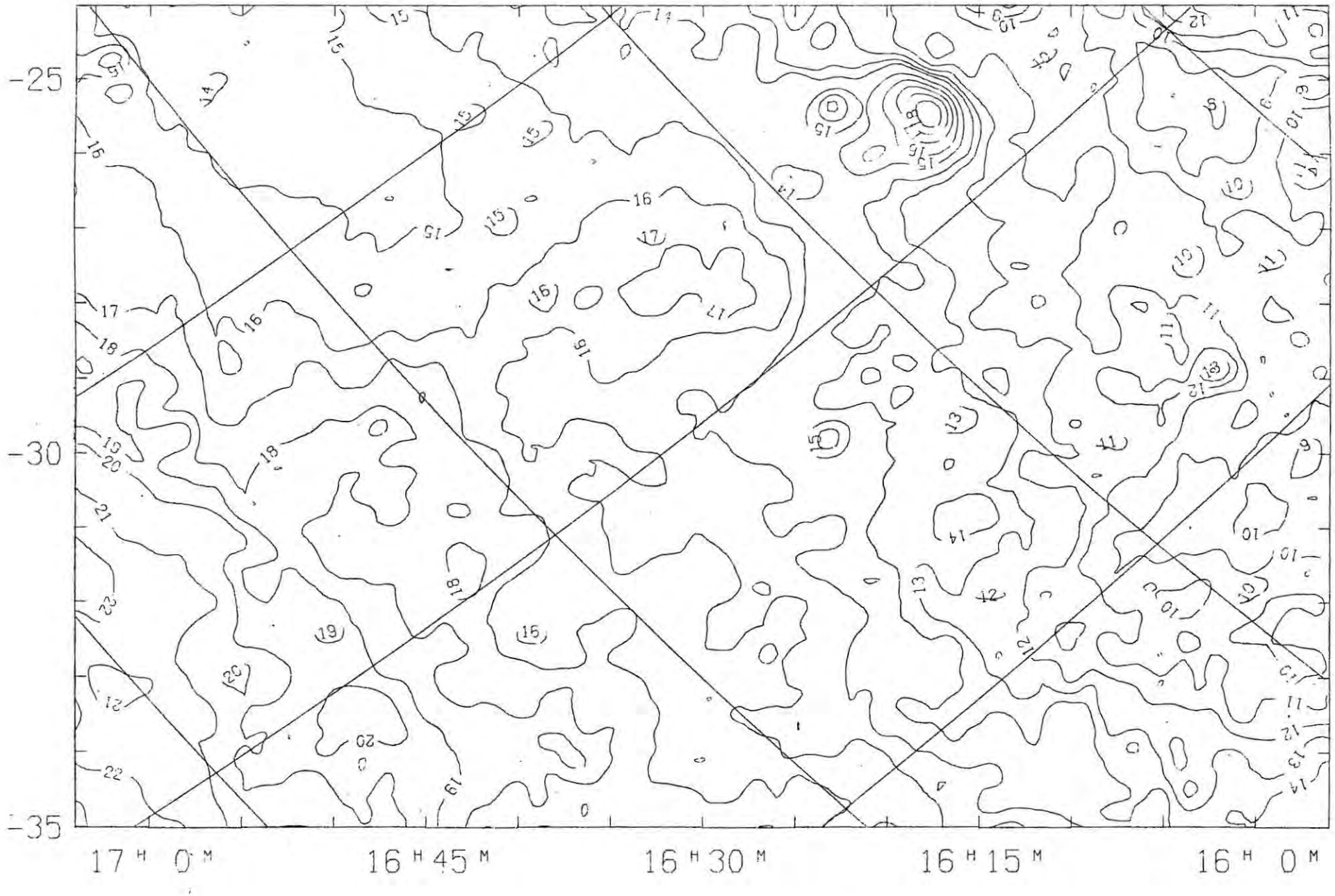
-25
-30
-35
17 H 0 M
16 H 45 M
16 H 30 M
16 H 15 M
16 H 0 M

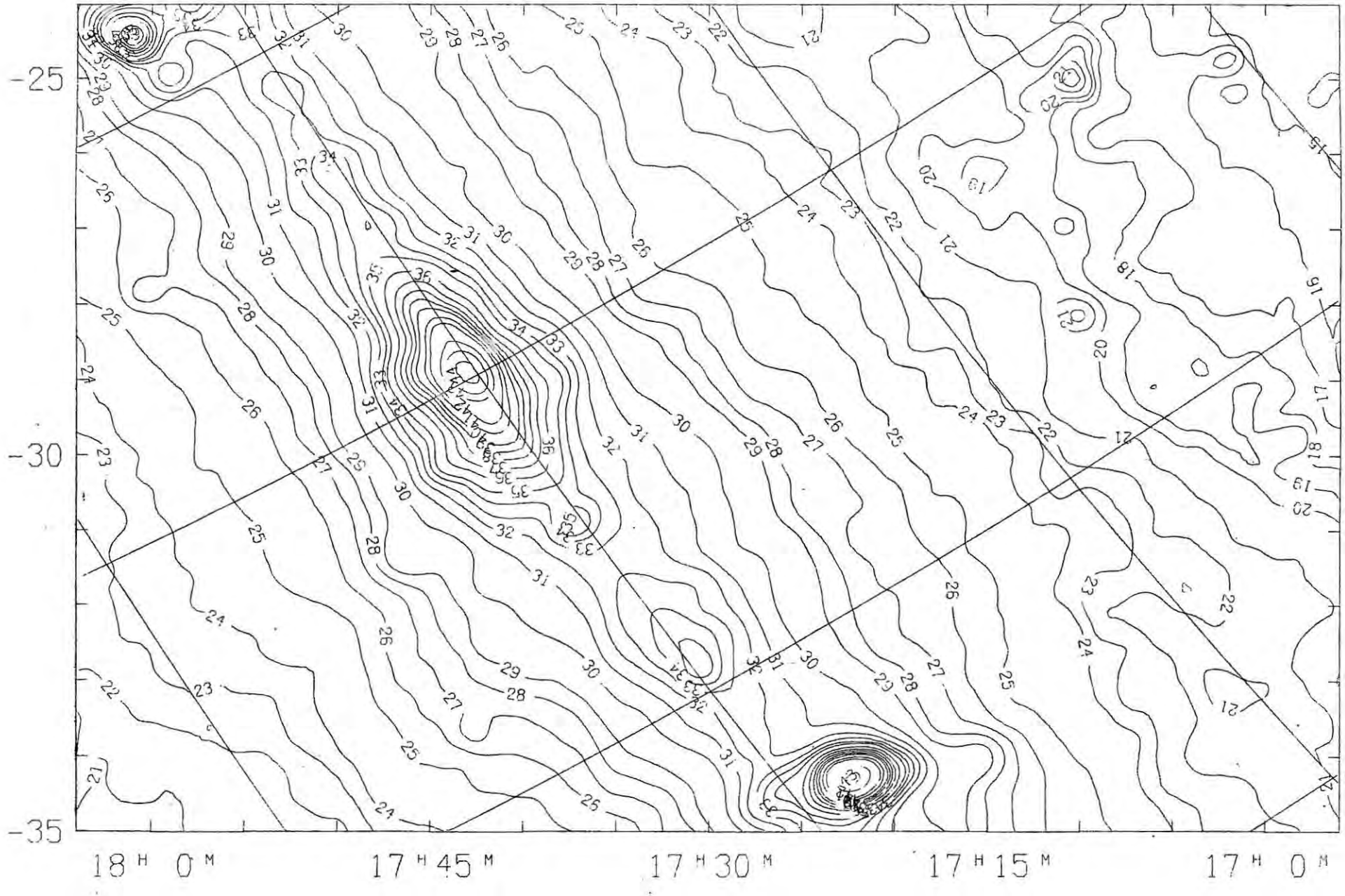
-25
-30
-35
18 H 0 M
17 H 45 M
17 H 30 M
17 H 15 M
17 H 0 M

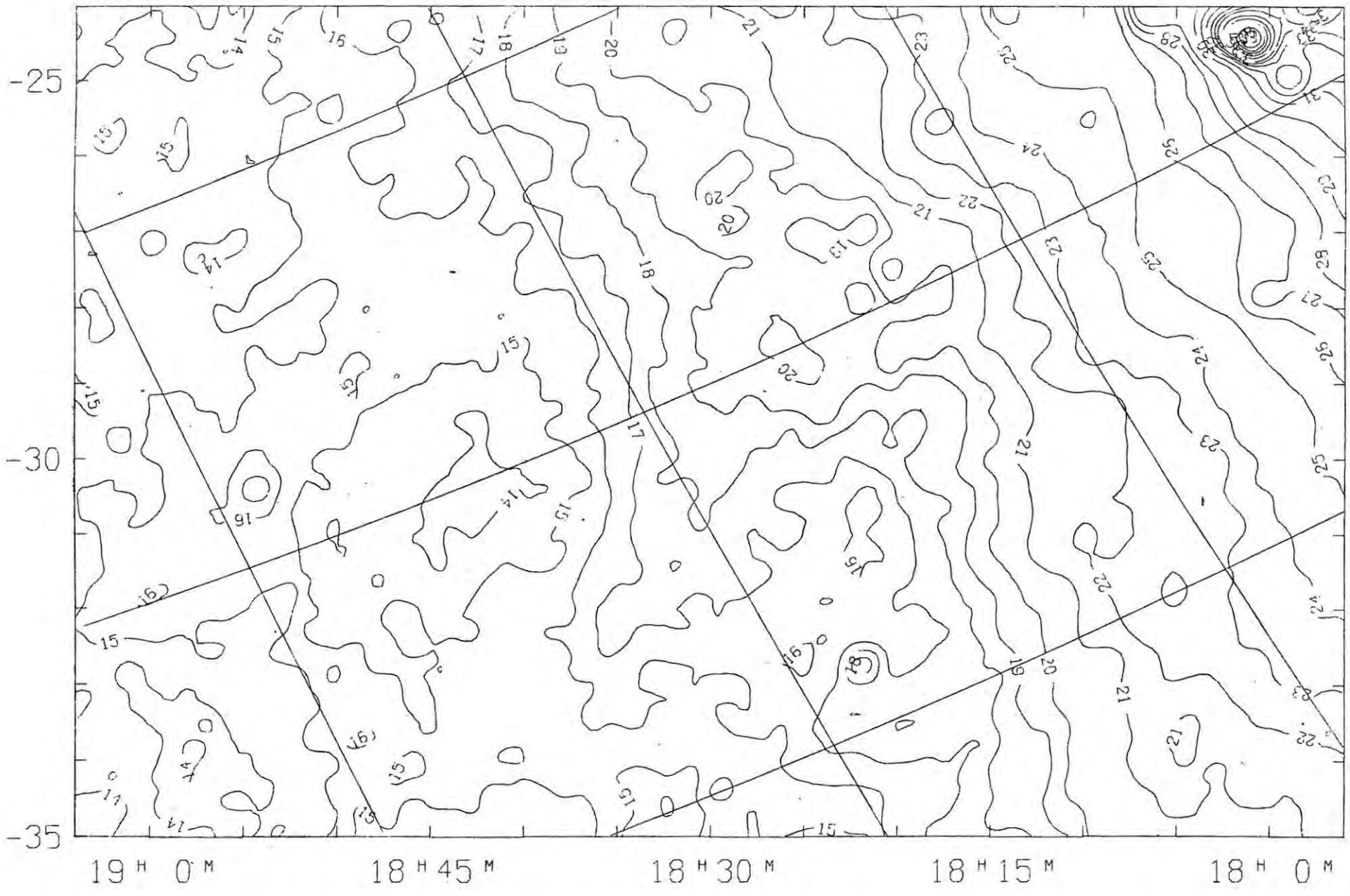
-25
-30
-35
19 H 0 M
18 H 45 M
18 H 30 M
18 H 15 M
18 H 0 M

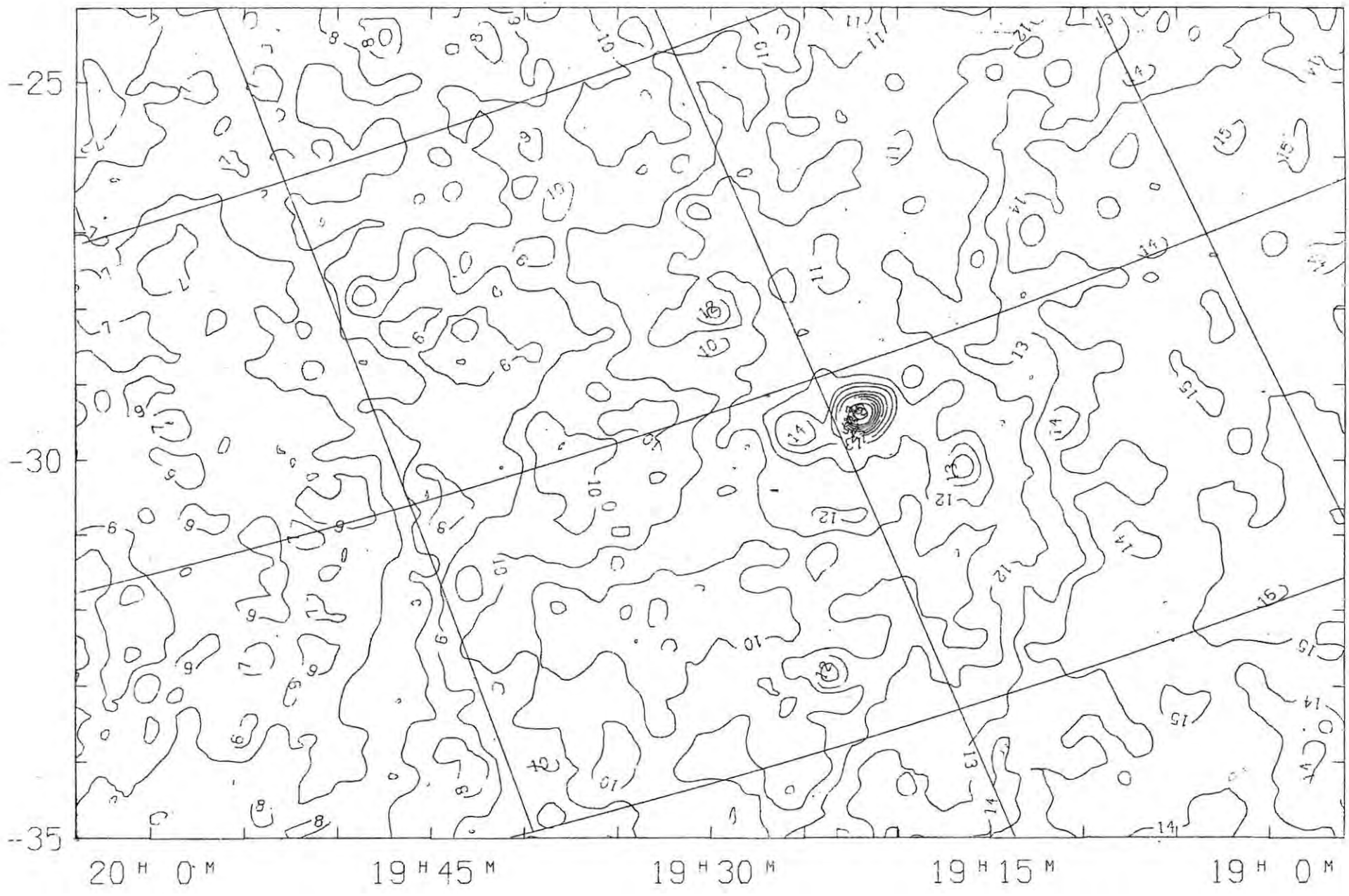
-25
-30
-35
20 H 0 M
19 H 45 M
19 H 30 M
19 H 15 M
19 H 0 M

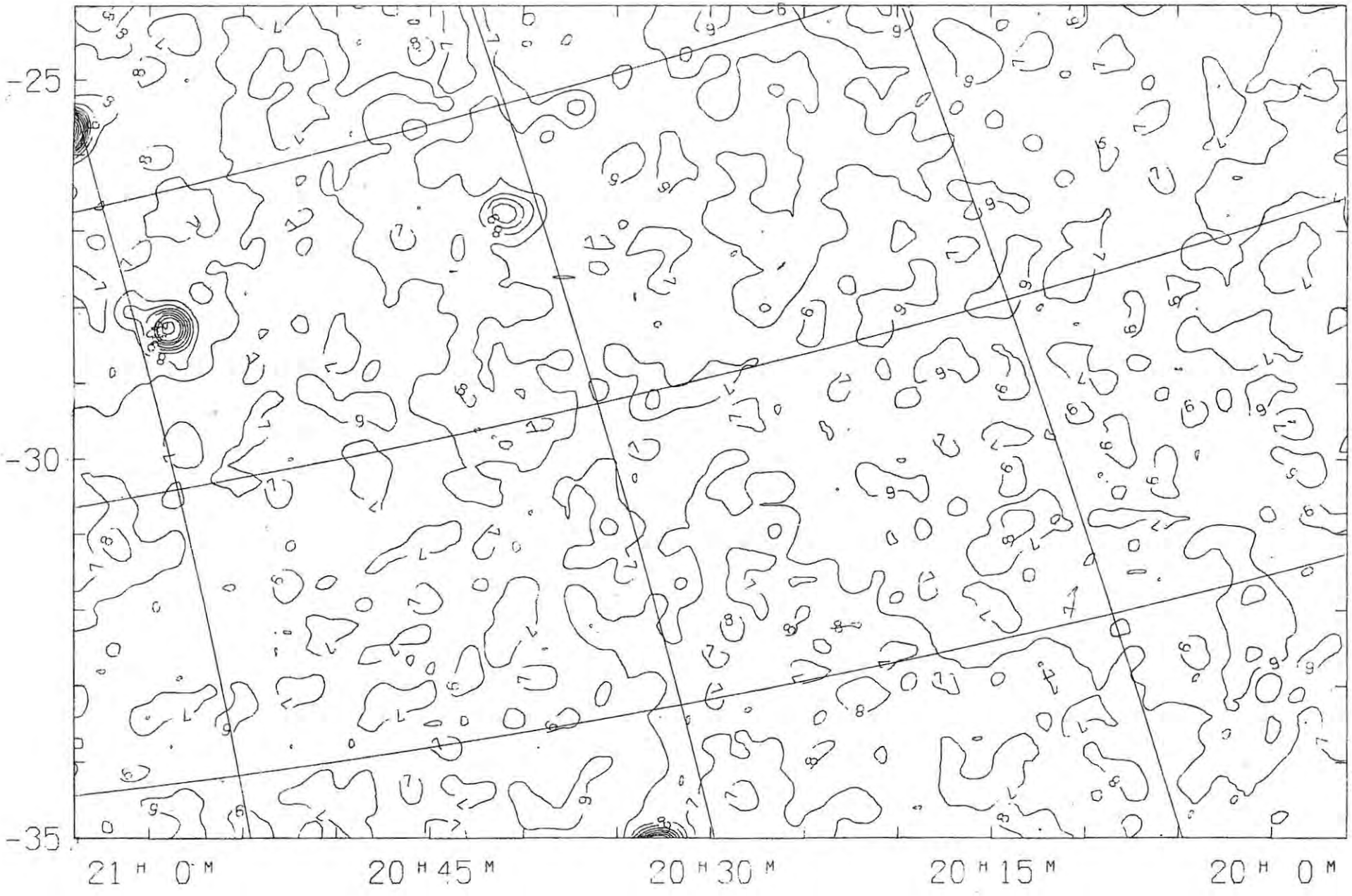
-25
-30
-35
21 H 0 M
20 H 45 M
20 H 30 M
20 H 15 M
20 H 0 M

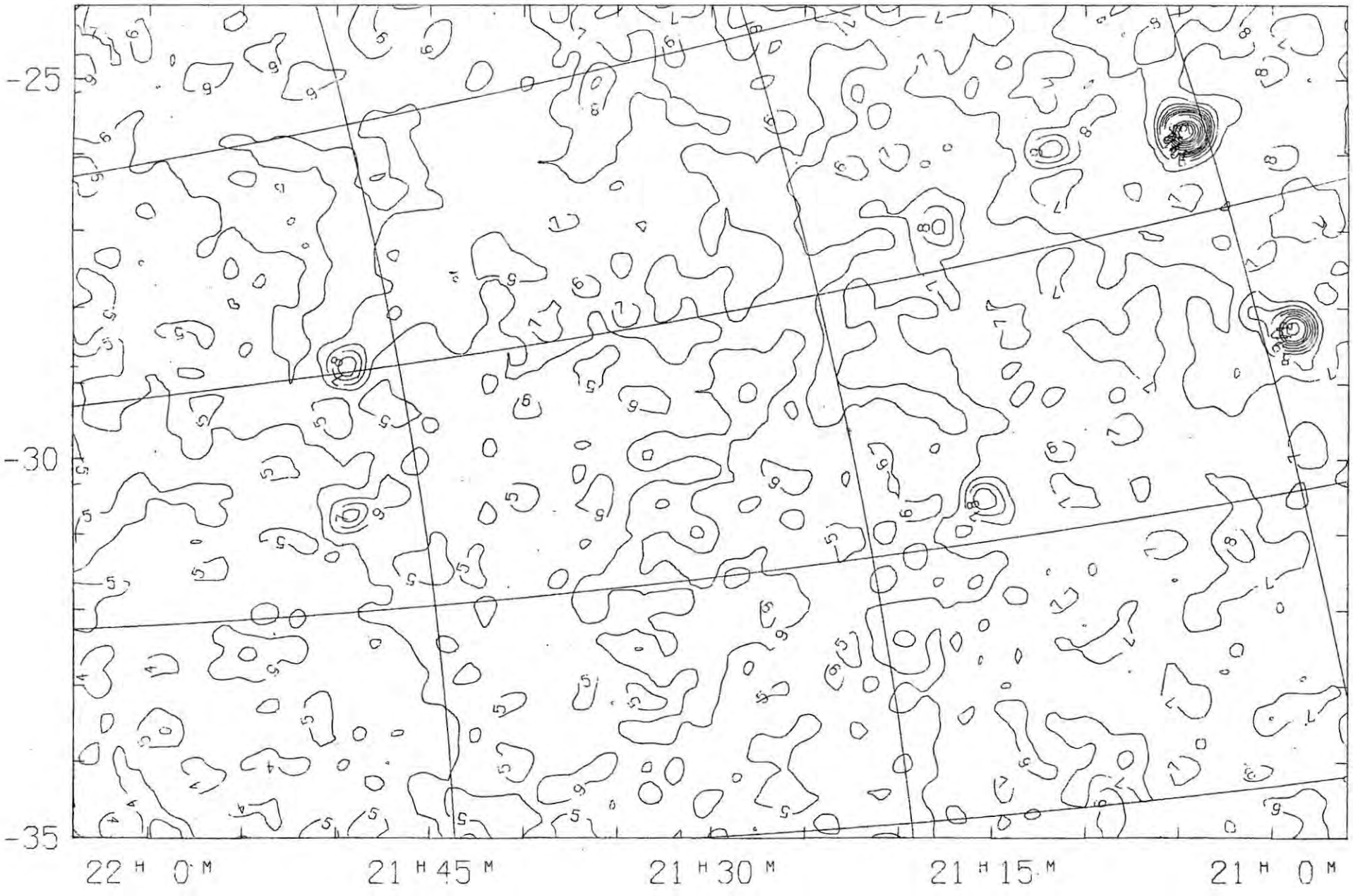
-25
-30
-35
22 H 0 M
21 H 45 M
21 H 30 M
21 H 15 M
21 H 0 M

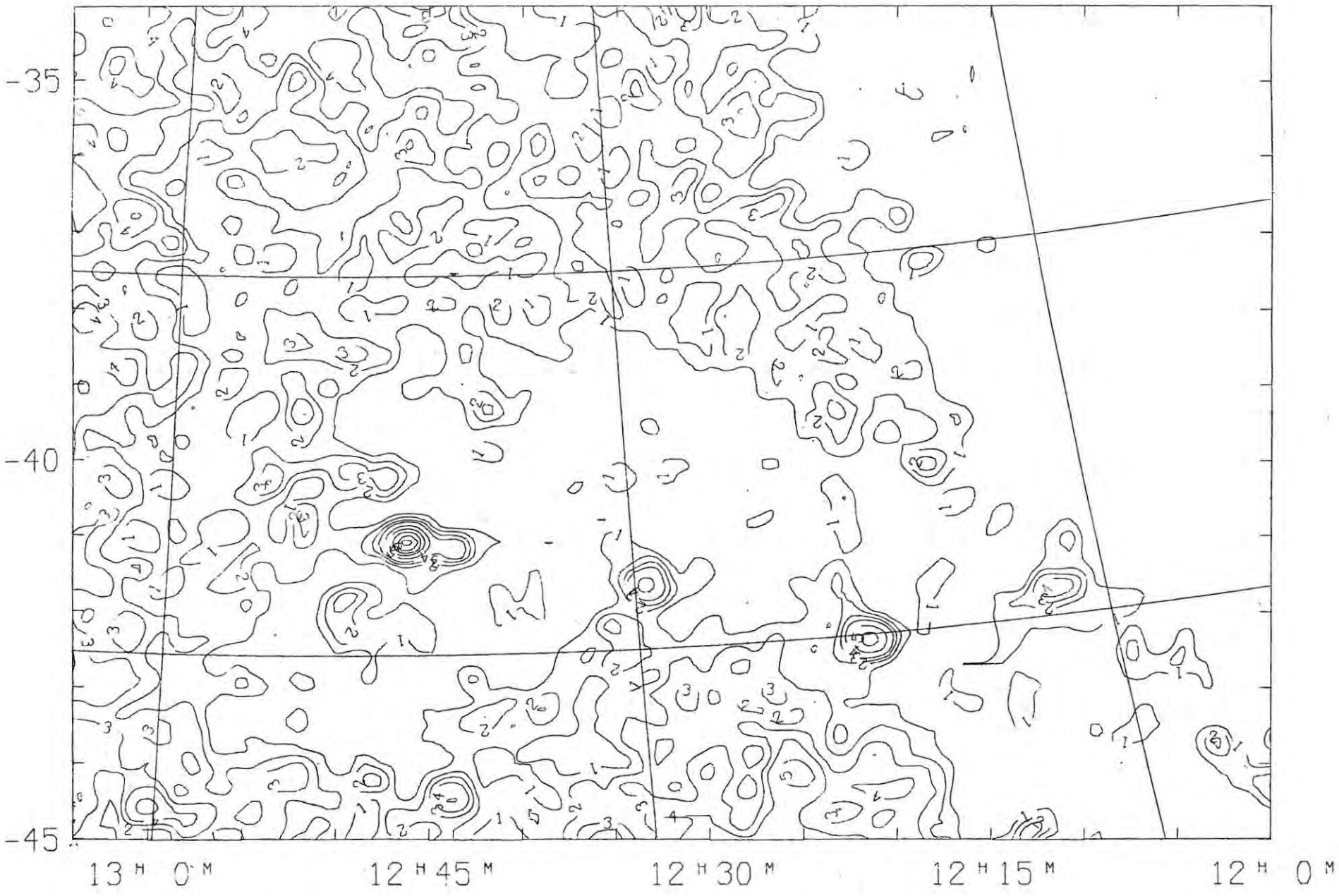
-35
-40
-45
13 H 0 M
12 H 45 M
12 H 30 M
12 H 15 M
12 H 0 M

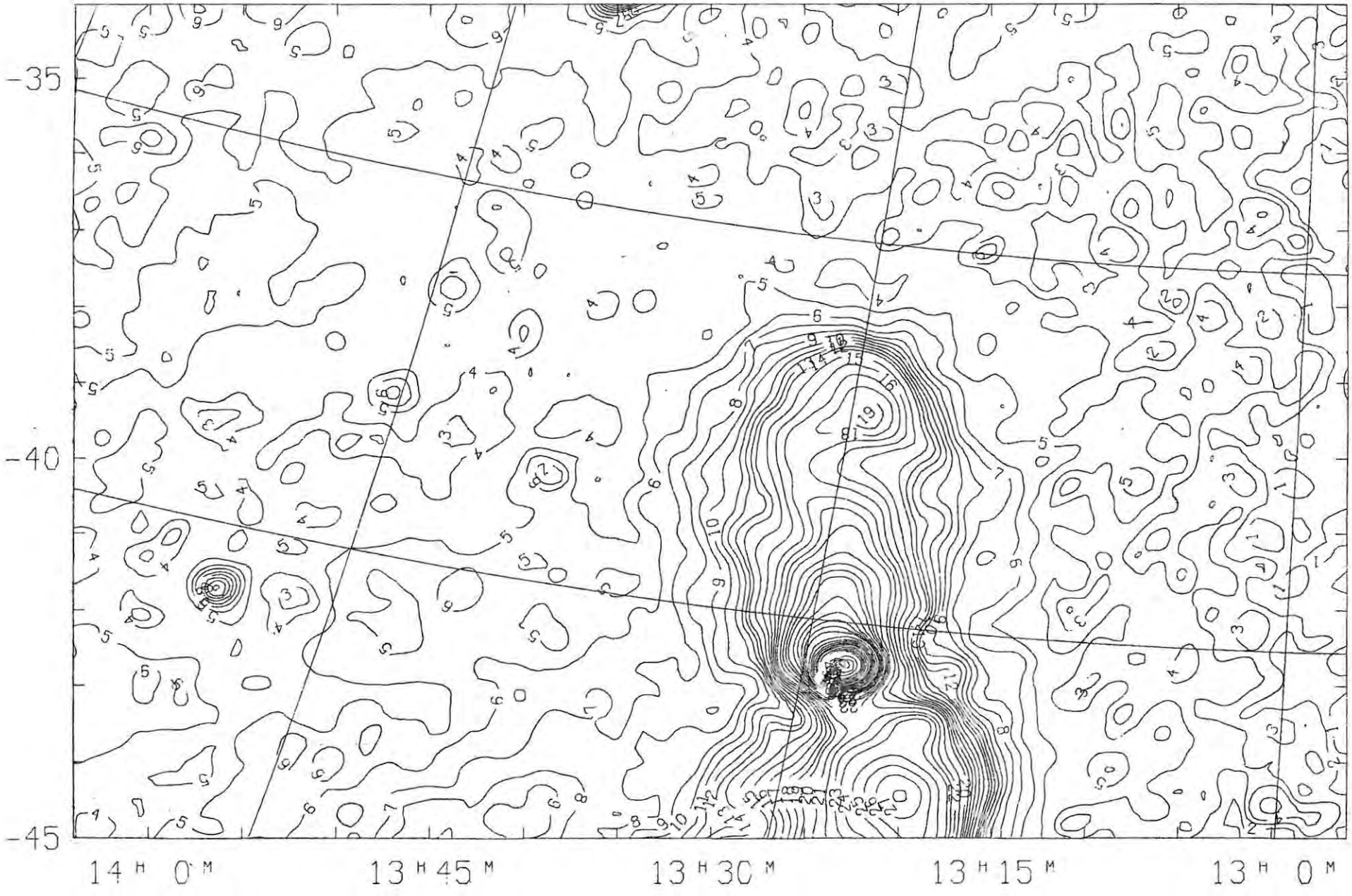
-35
-40
-45
14 H 0 M
13 H 45 M
13 H 30 M
13 H 15 M
13 H 0 M

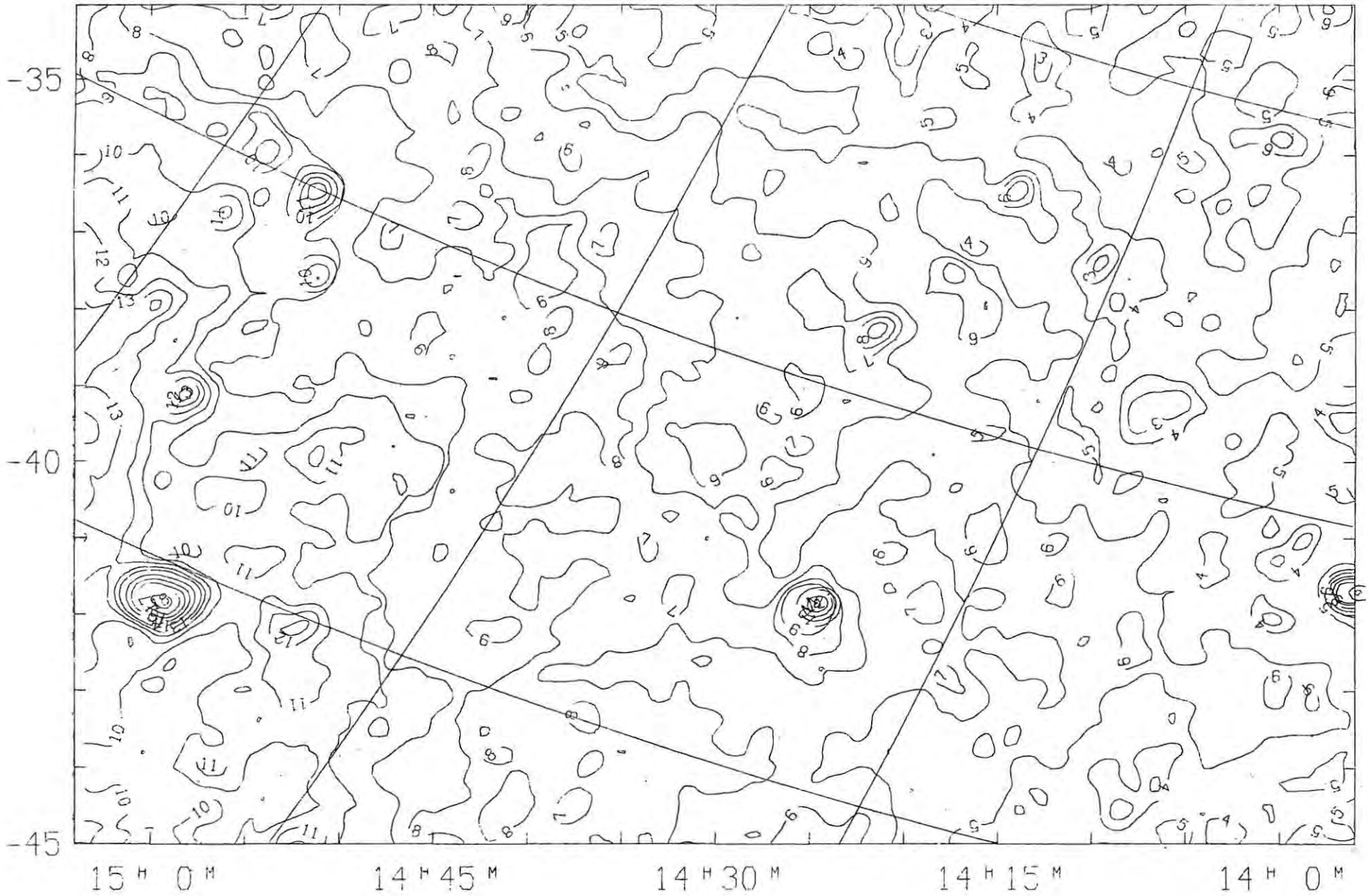
-35
-40
-45
15 H 0 M
14 H 45 M
14 H 30 M
14 H 15 M
14 H 0 M

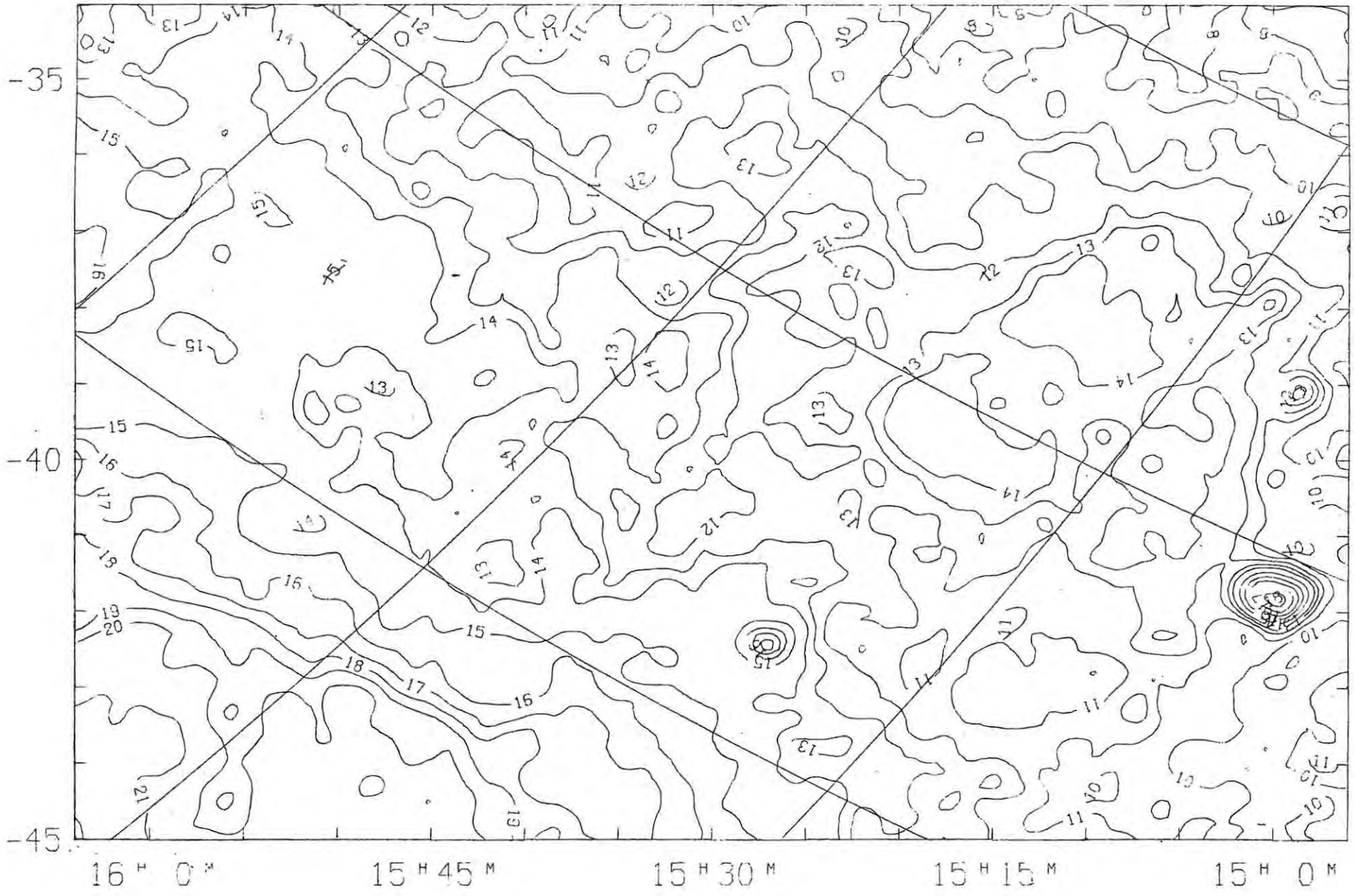
-35
-40
-45
16 H 0 M
15 H 45 M
15 H 30 M
15 H 15 M
15 H 0 M

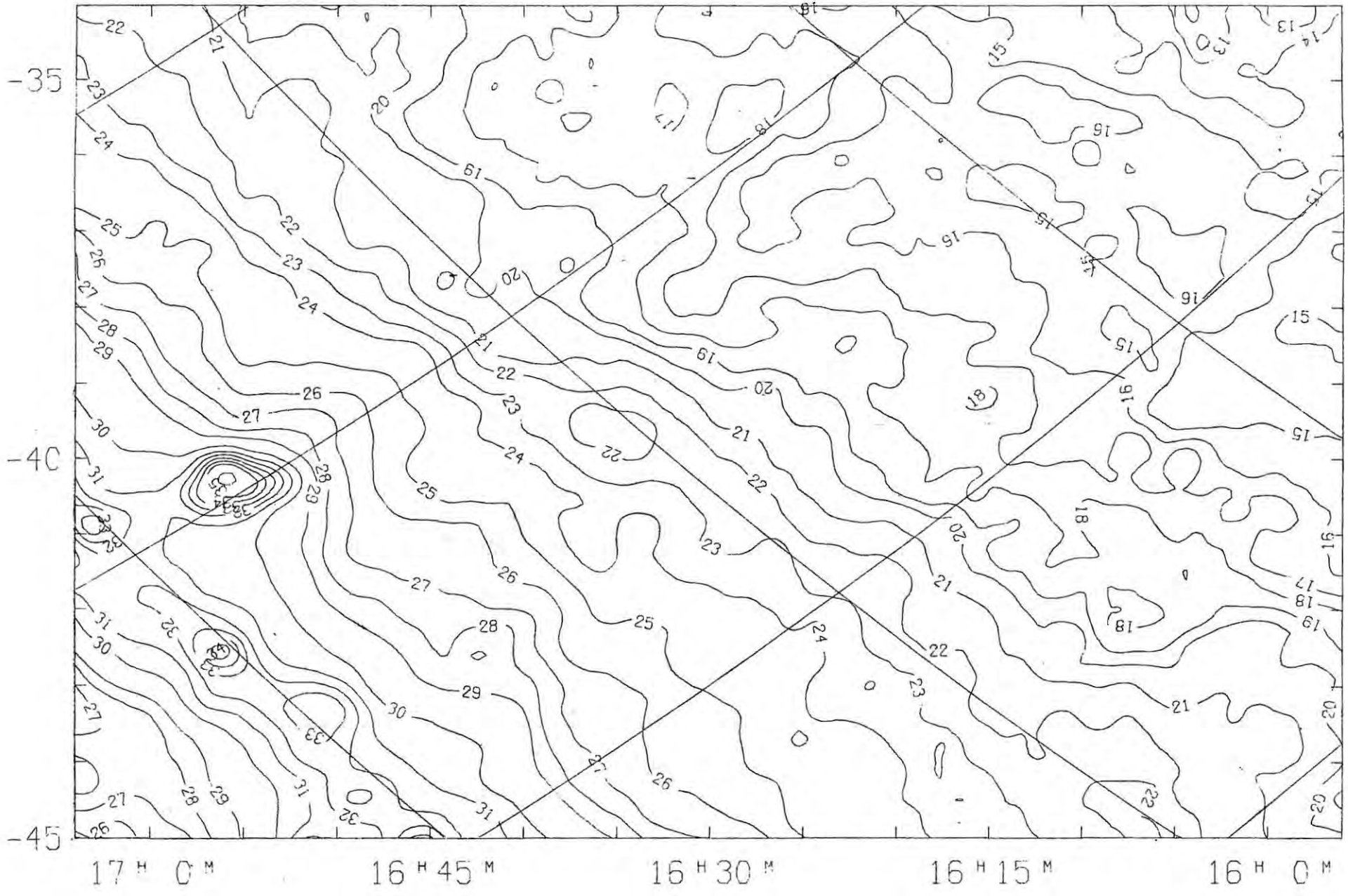
-35
-40
-45
17 H 0 M
16 H 45 M
16 H 30 M
16 H 15 M
16 H 0 M

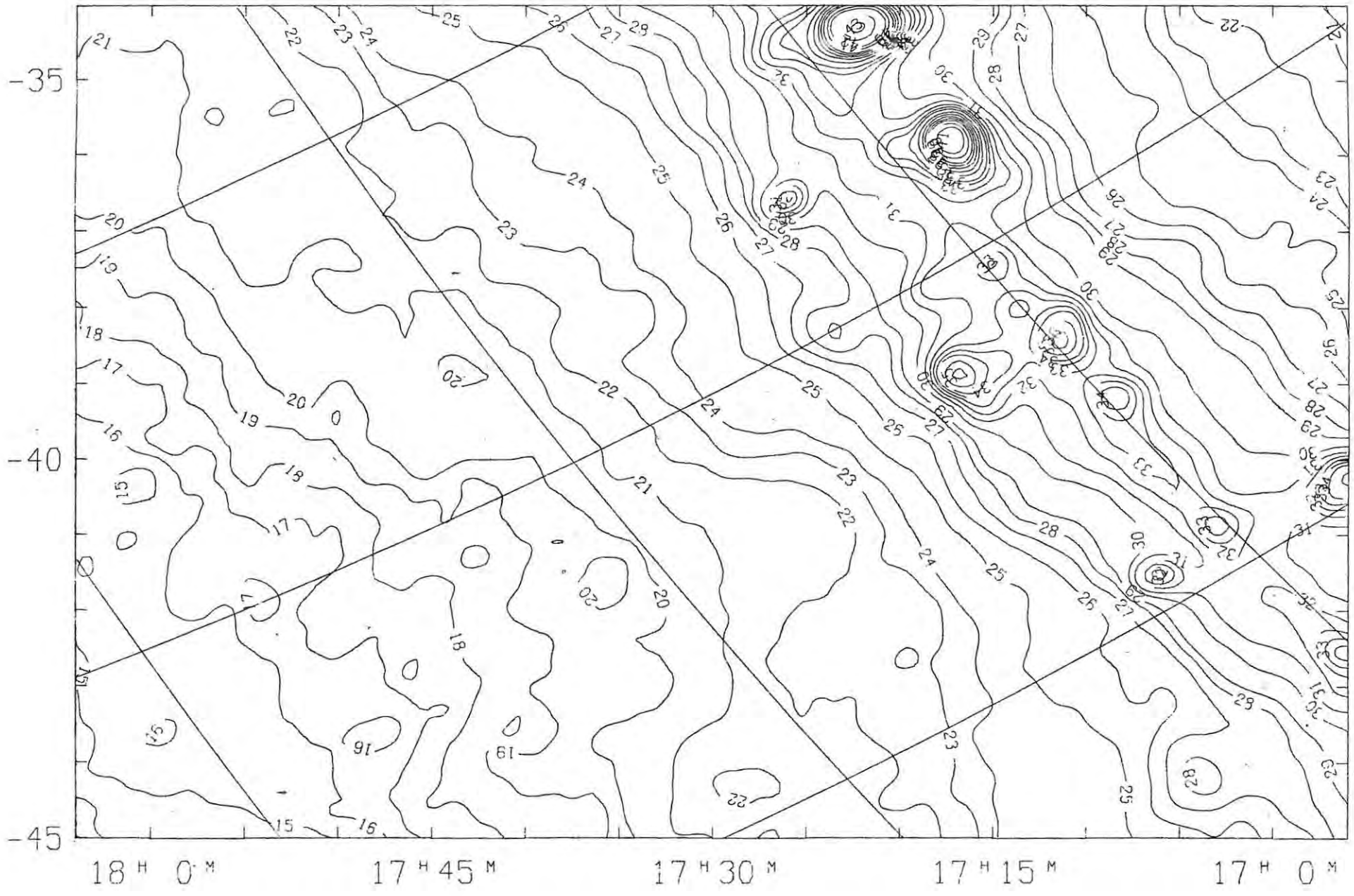
-35
-40
-45
18 H 0 M
17 H 45 M
17 H 30 M
17 H 15 M
17 H 0 M

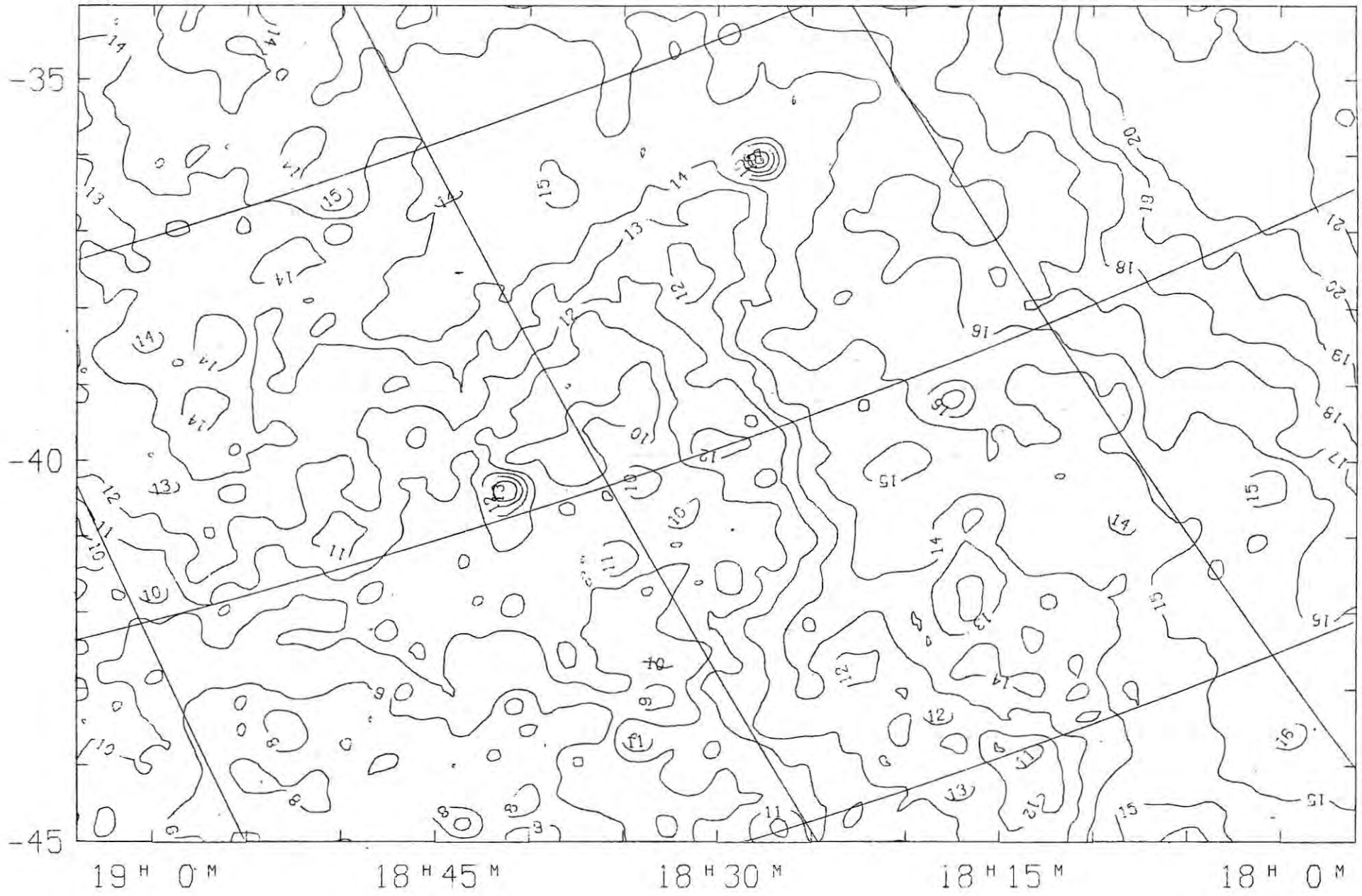
-35
-40
-45
19 H 0 M
18 H 45 M
18 H 30 M
18 H 15 M
18 H 0 M

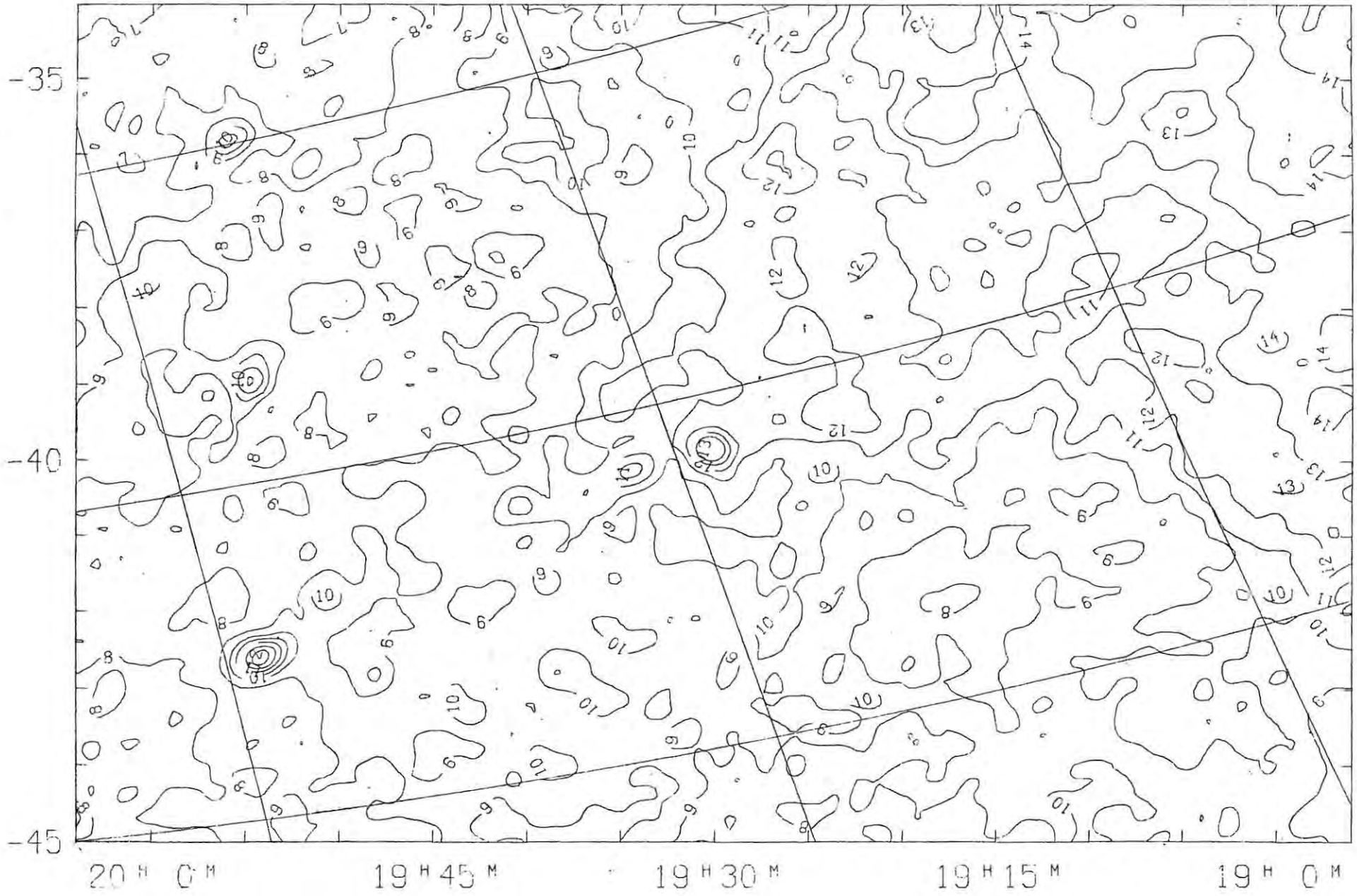
-35
-40
-45
20 H 0 M
19 H 45 M
19 H 30 M
19 H 15 M
19 H 0 M

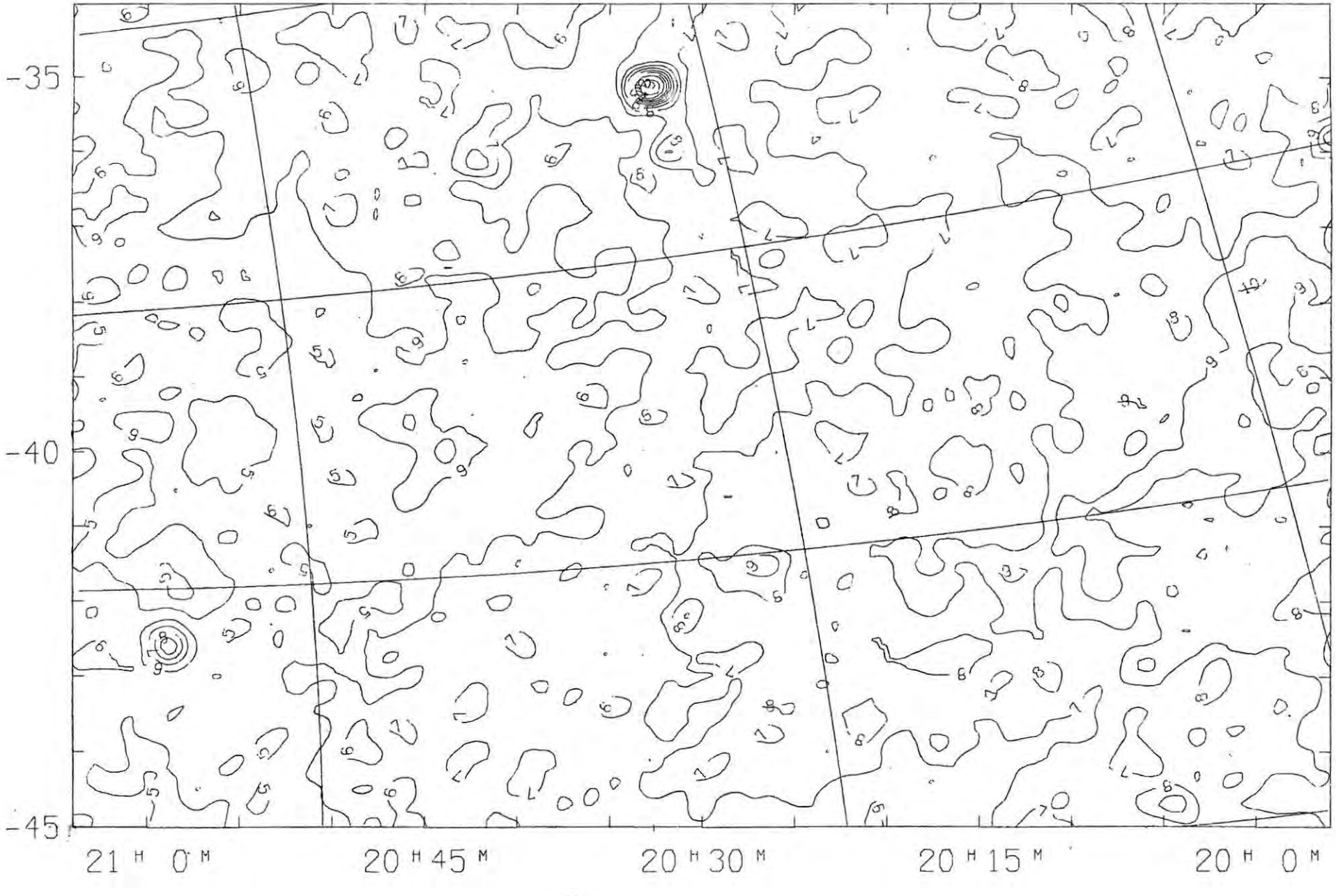
-35
-40
-45
21 H 0 M
20 H 45 M
20 H 30 M
20 H 15 M
20 H 0 M

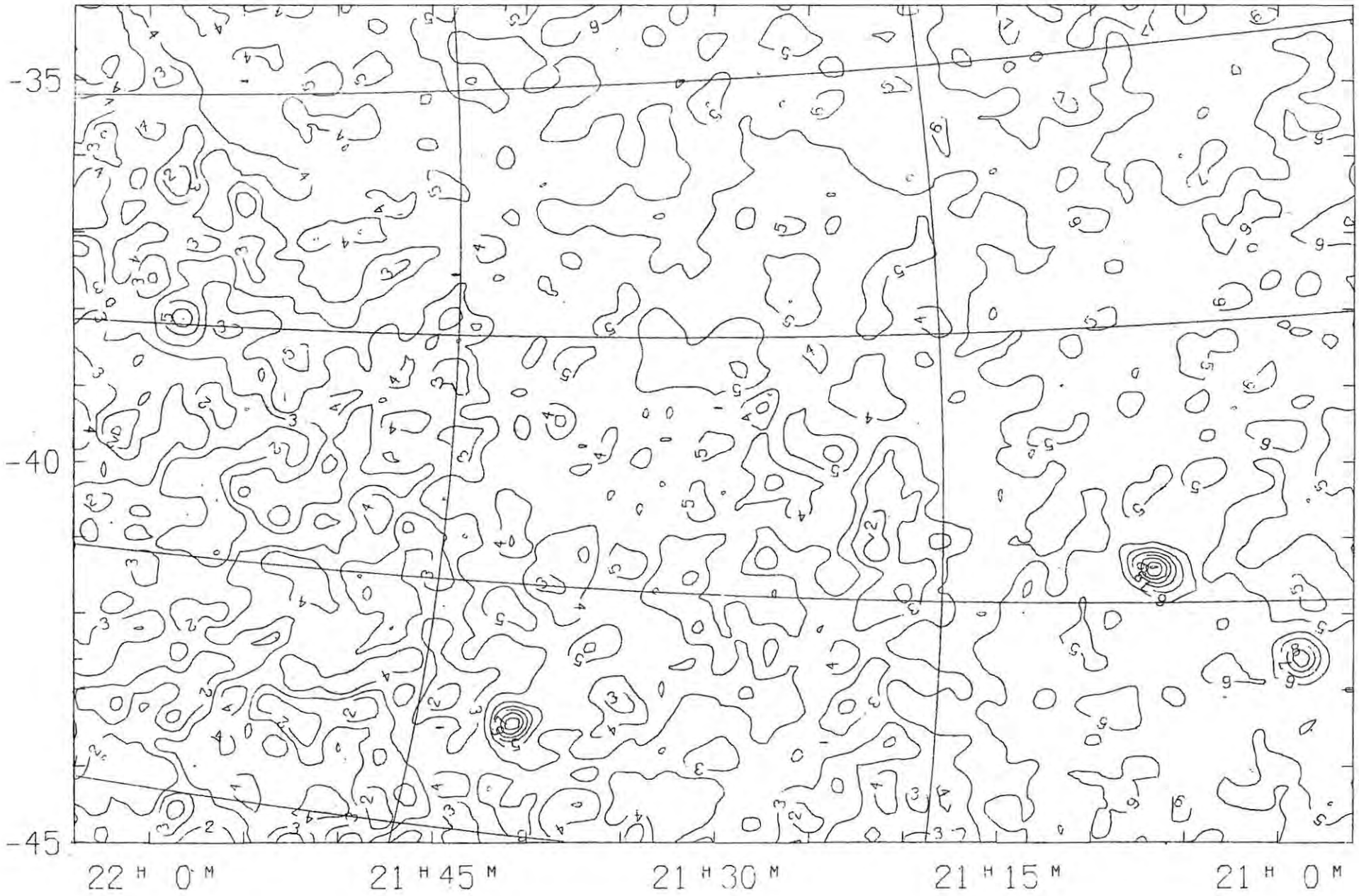
-35
-40
-45
22 H 0 M
21 H 45 M
21 H 30 M
21 H 15 M
21 H 0 M

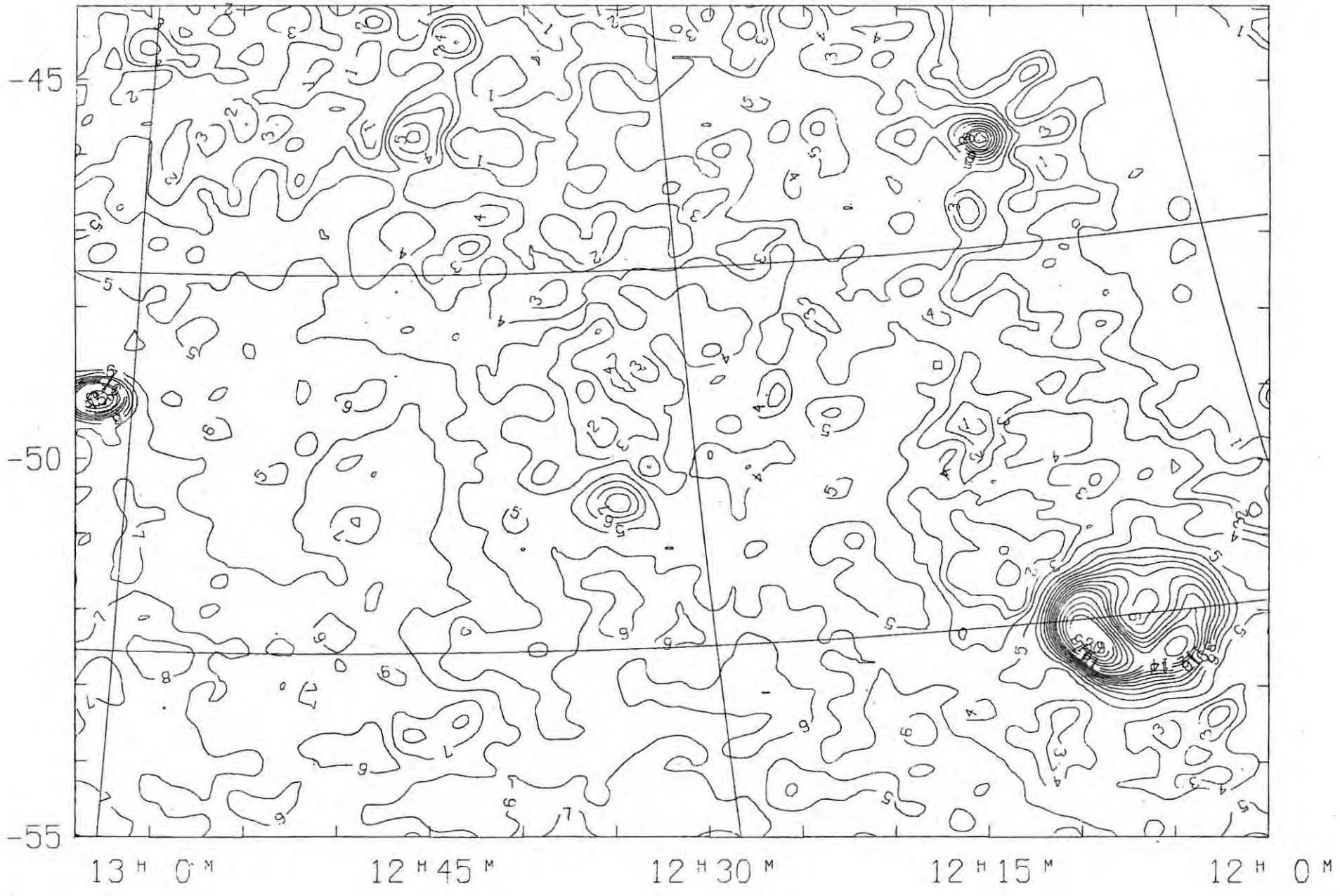
-45
-50
-55
13 H 0 M
12 H 45 M
12 H 30 M
12 H 15 M
12 H 0 M

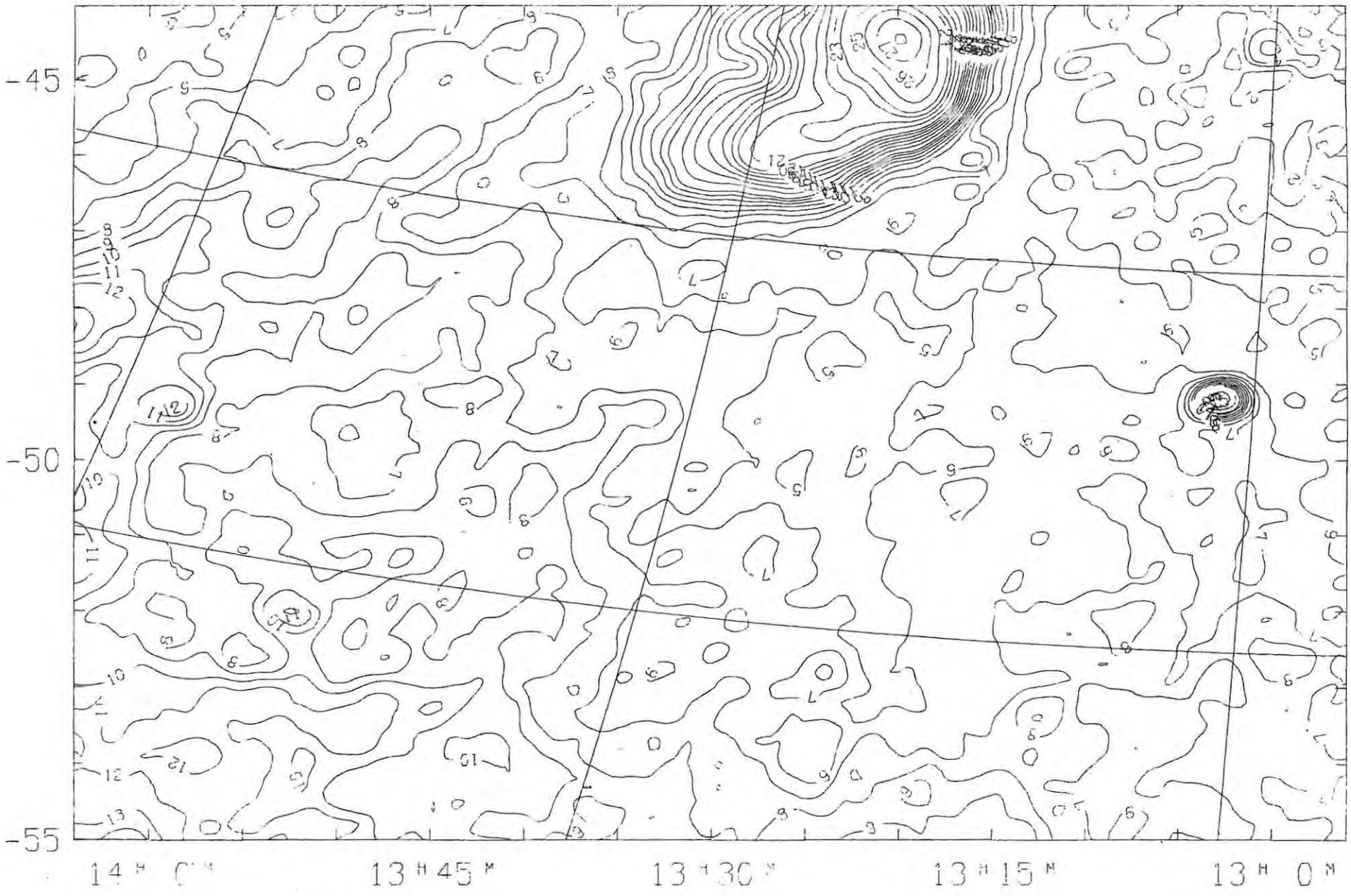
-45
-50
-55
14 H 0 M
13 H 45 M
13 H 30 M
13 H 15 M
13 H 0 M

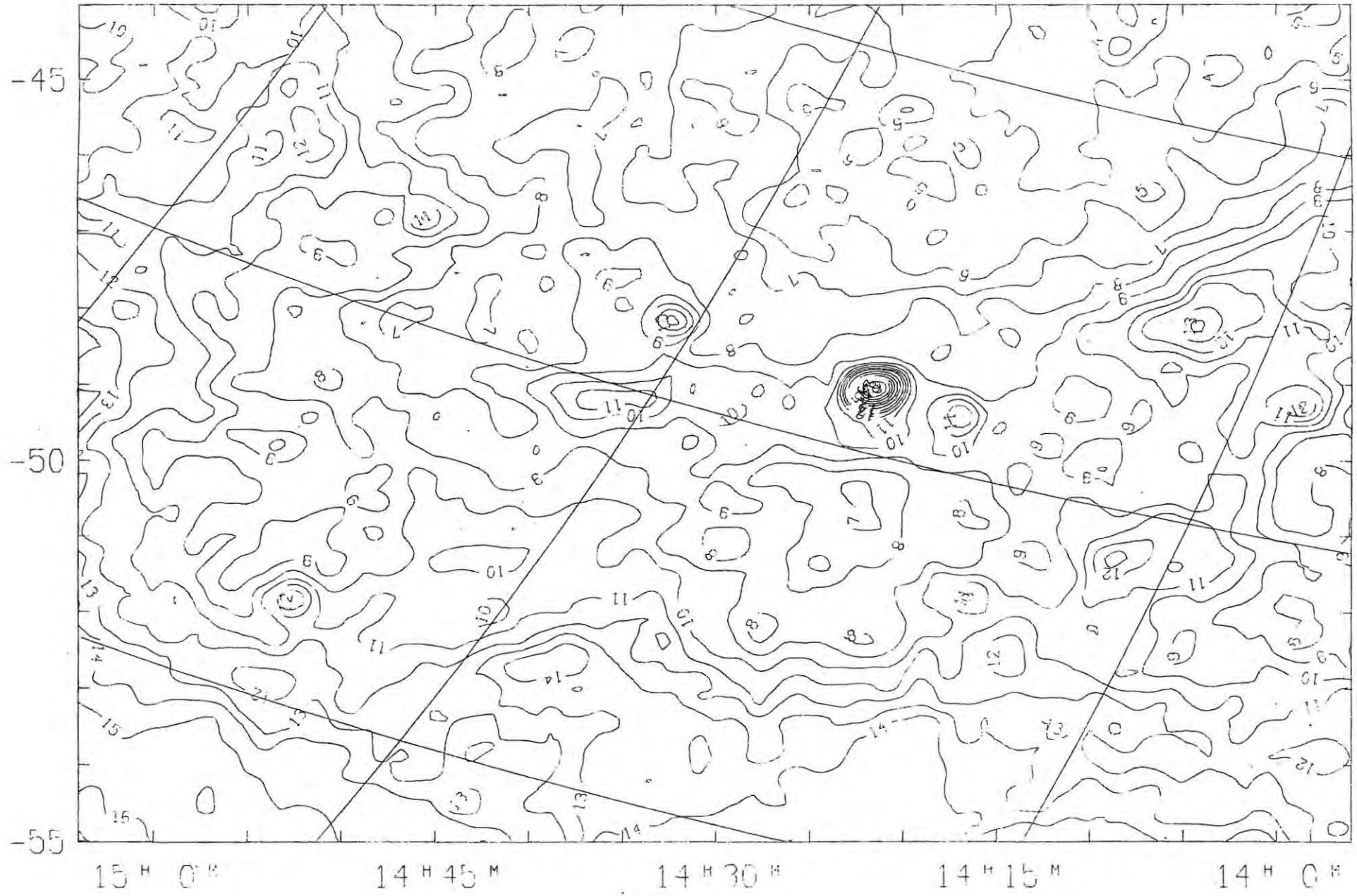
-45
-50
-55
15 H 0 M
14 H 45 M
14 H 30 M
14 H 15 M
14 H 0 M

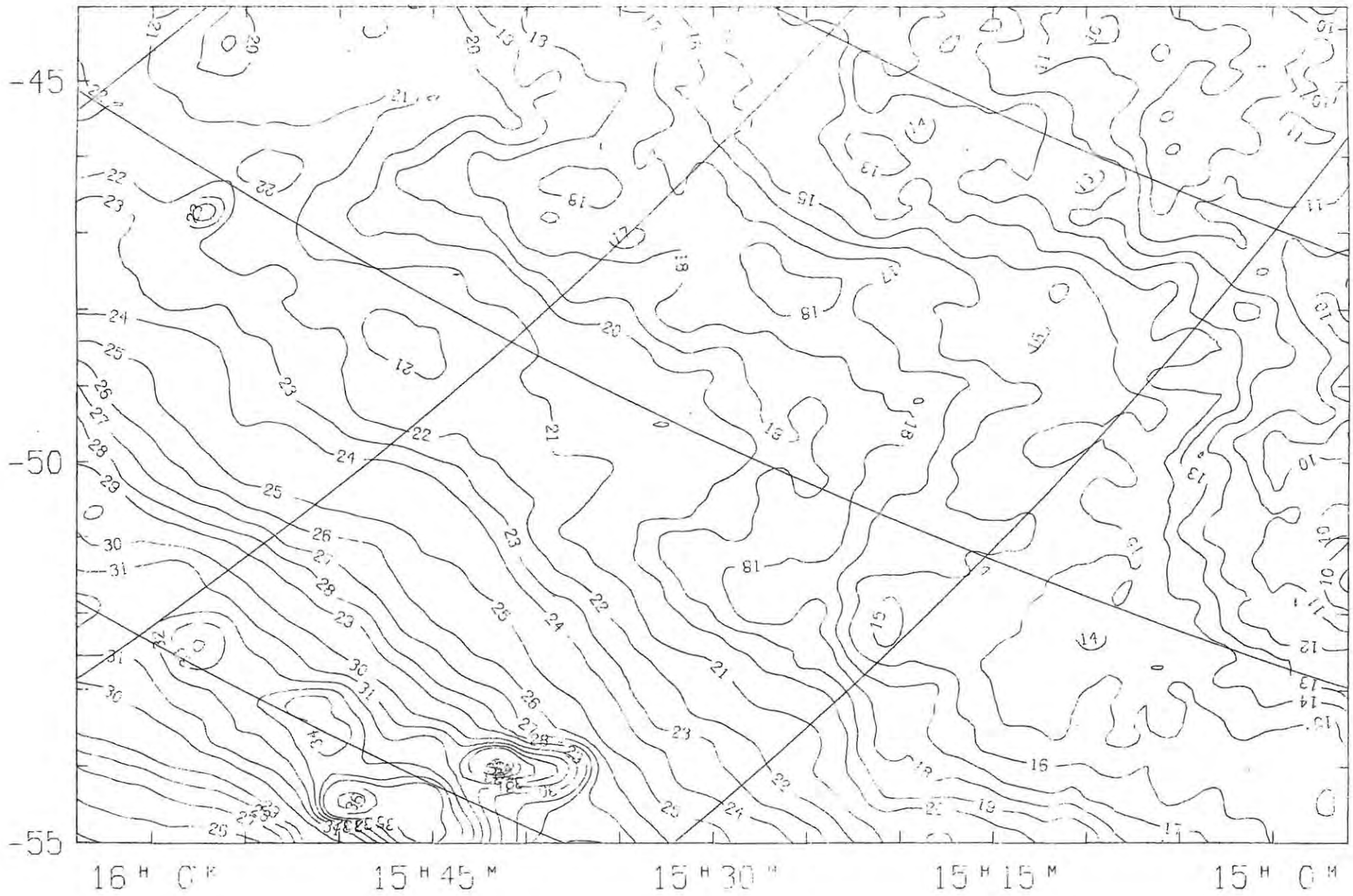
-45
-50
-55
16 H 0 M
15 H 45 M
15 H 30 M
15 H 15 M
15 H 0 M

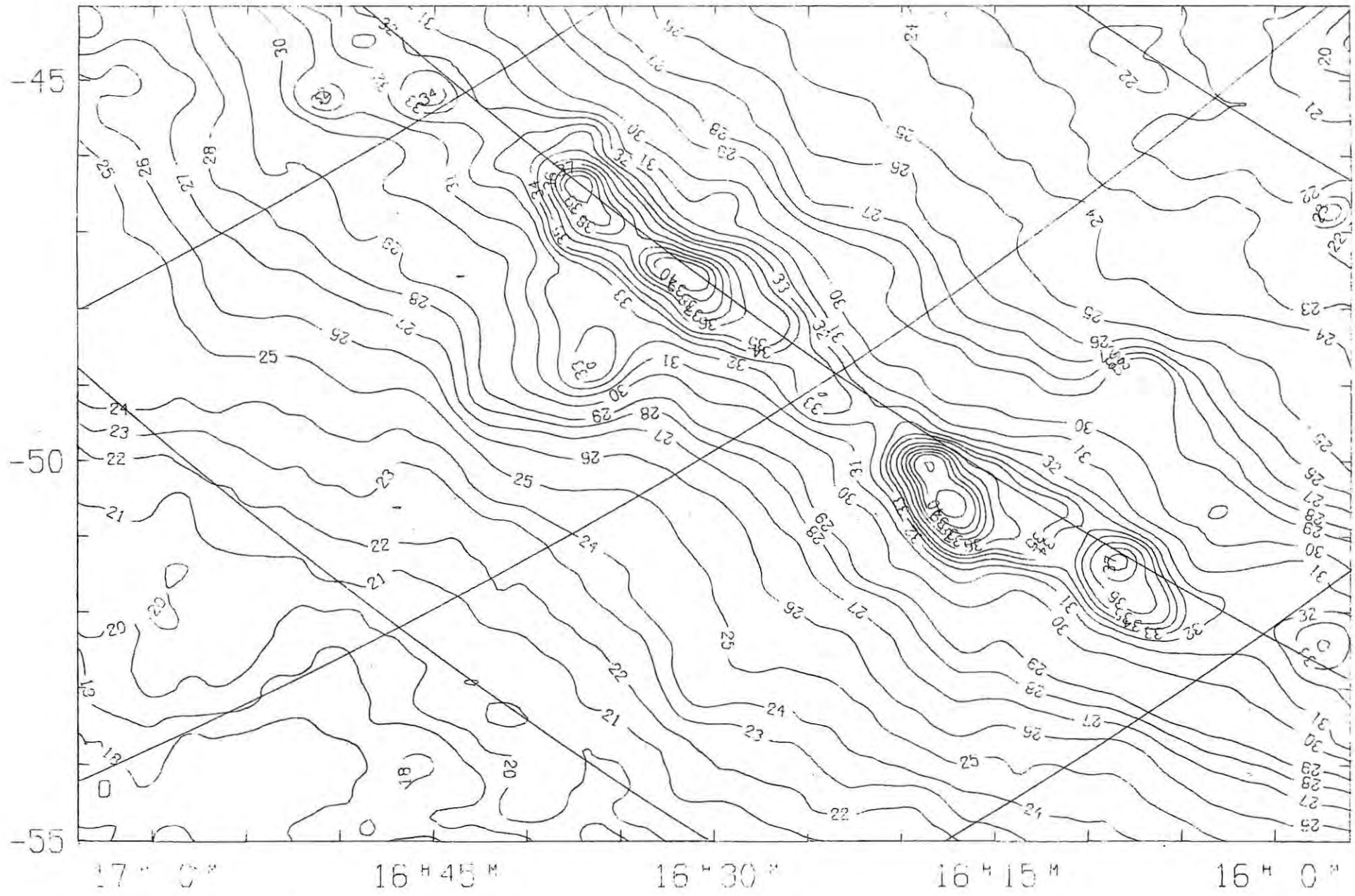
-45
-50
-55
17 H 0 M
16 H 45 M
16 H 30 M
16 H 15 M
16 H 0 M

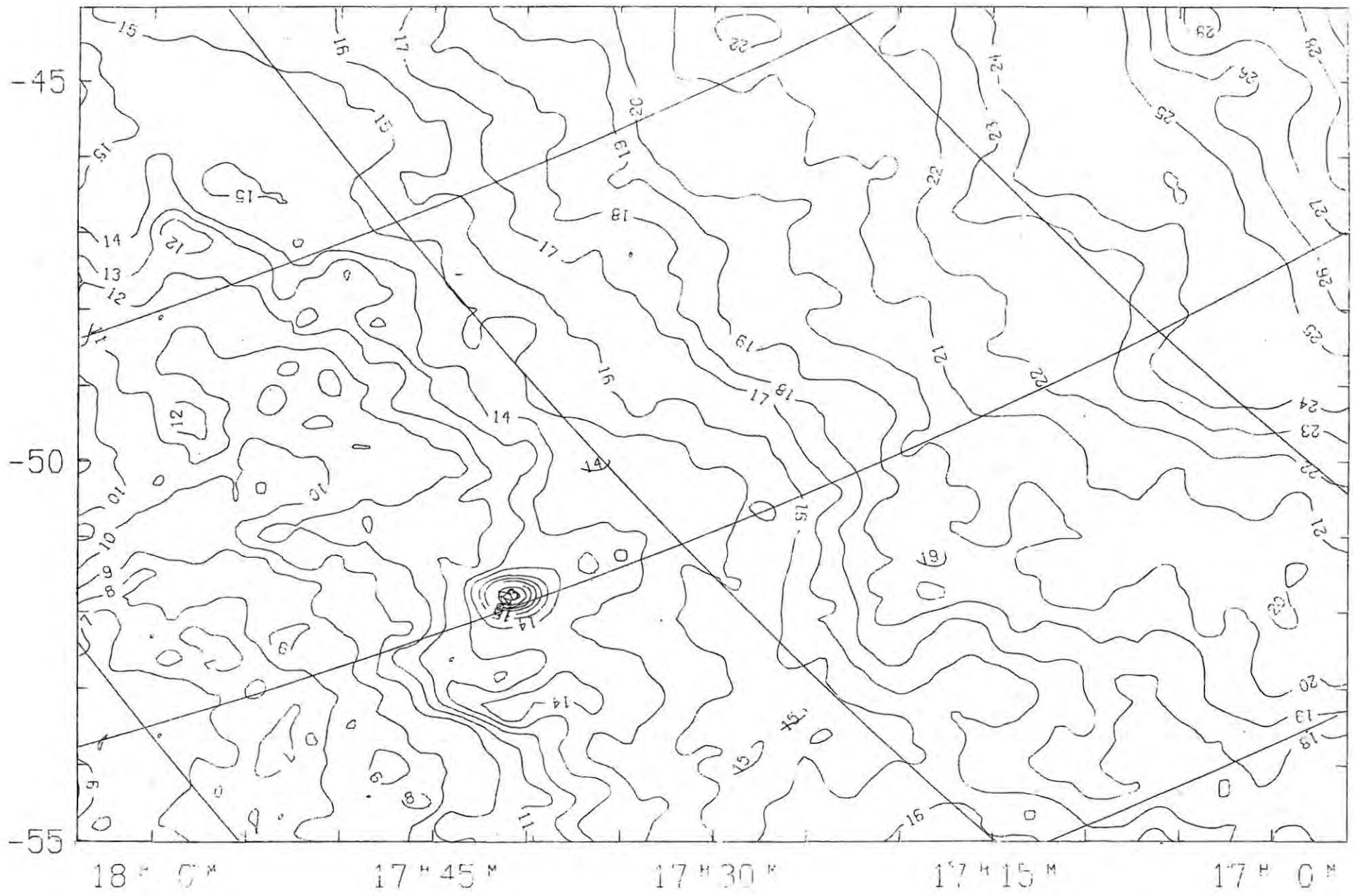
-45
-50
-55
18 H 0 M
17 H 45 M
17 H 30 M
17 H 15 M
17 H 0 M

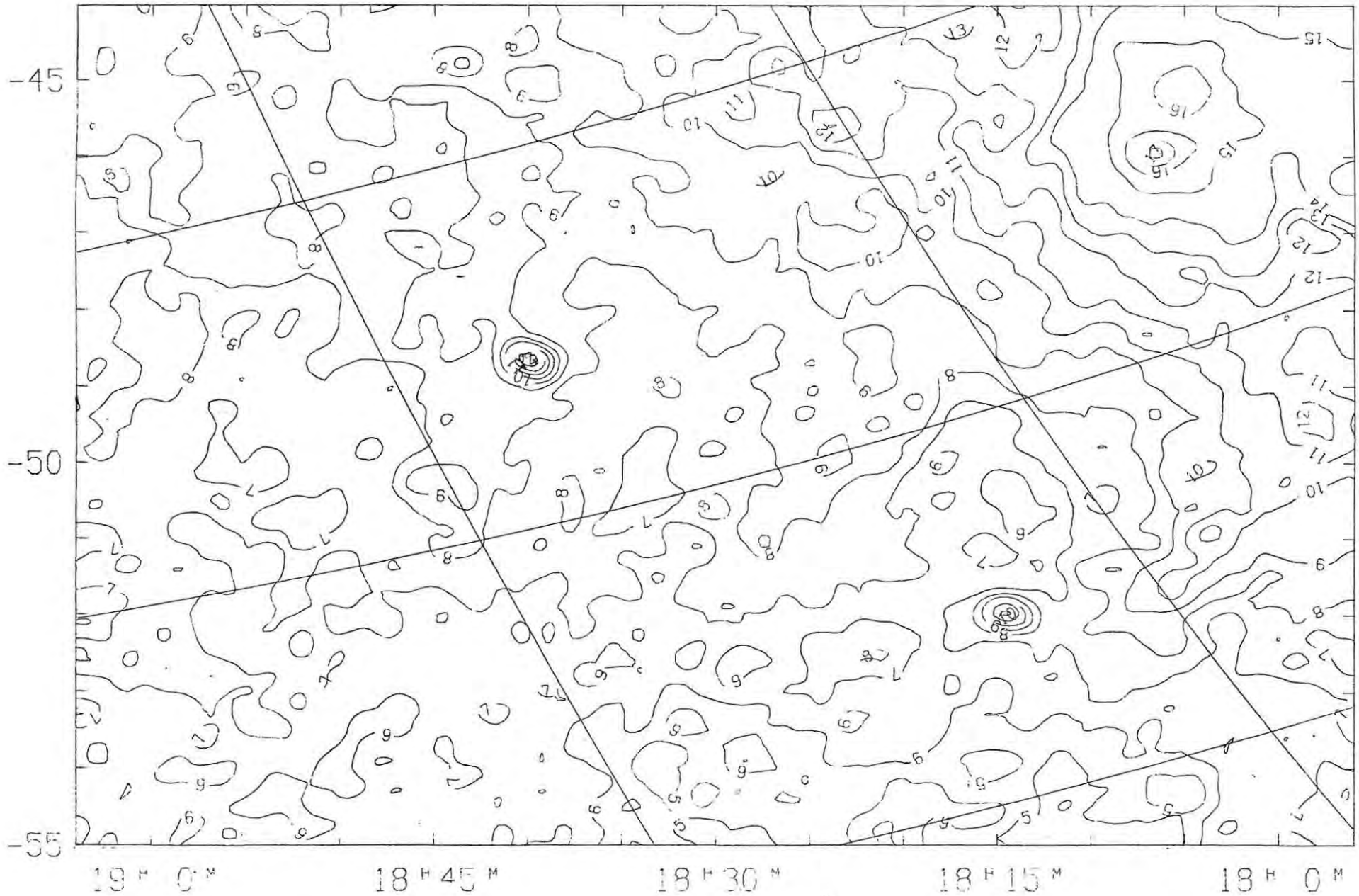
-45
-50
-55
19 H 0 M
18 H 45 M
18 H 30 M
18 H 15 M
18 H 0 M

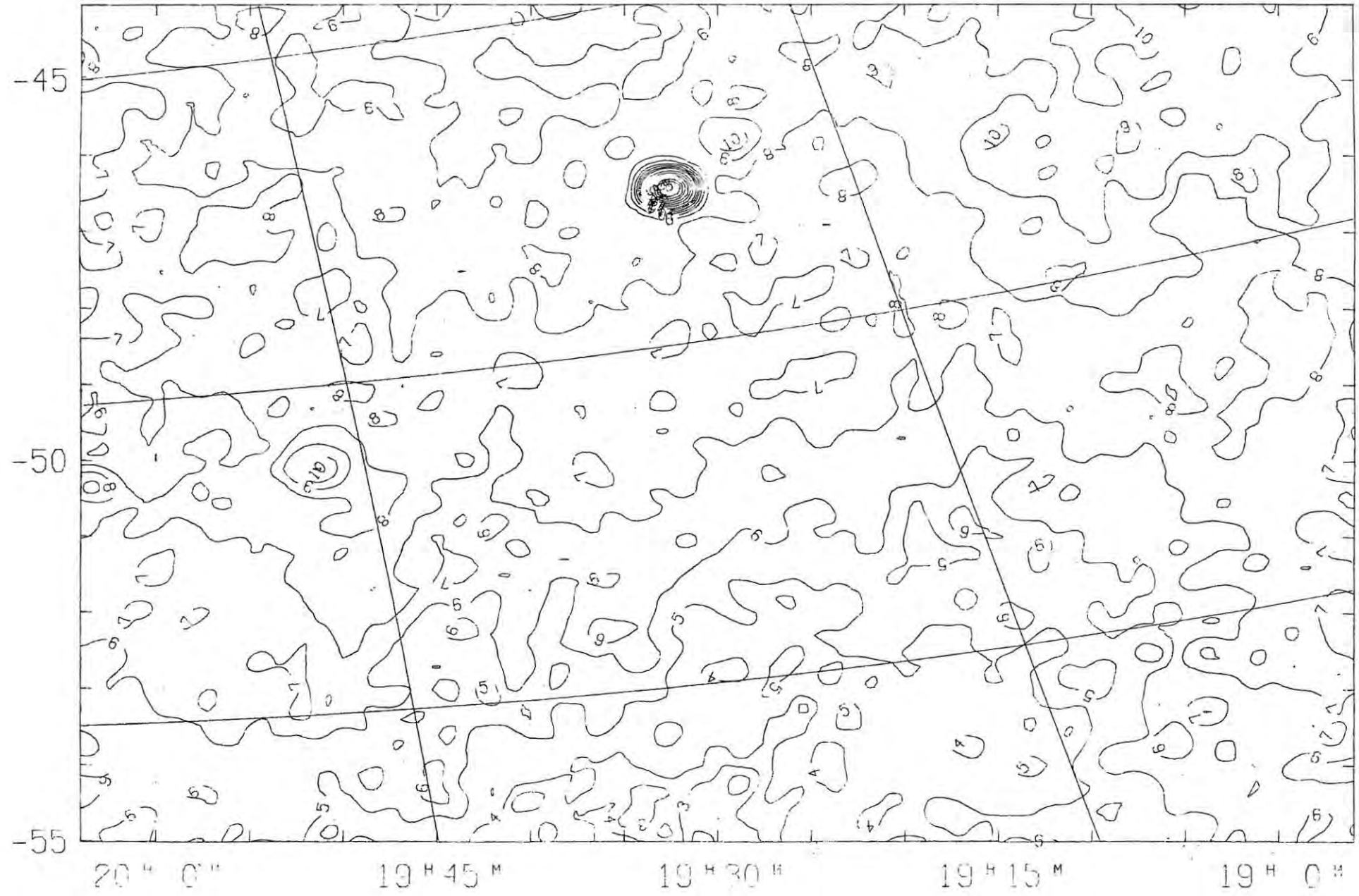
-45
-50
-55
20 H 0 M
19 H 45 M
19 H 30 M
19 H 15 M
19 H 0 M

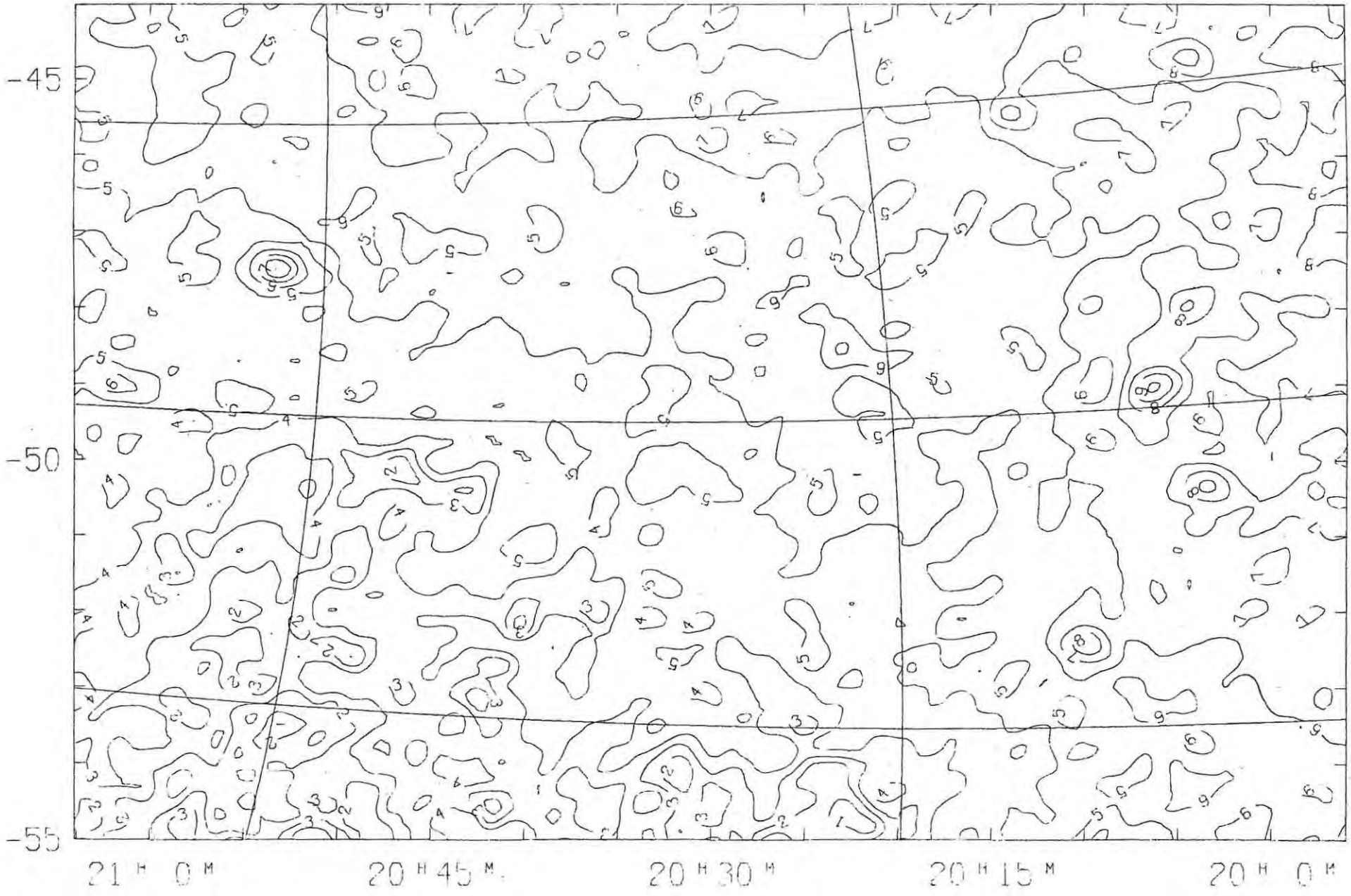
-45
-50
-55
21 H 0 M
20 H 45 M
20 H 30 M
20 H 15 M
20 H 0 M

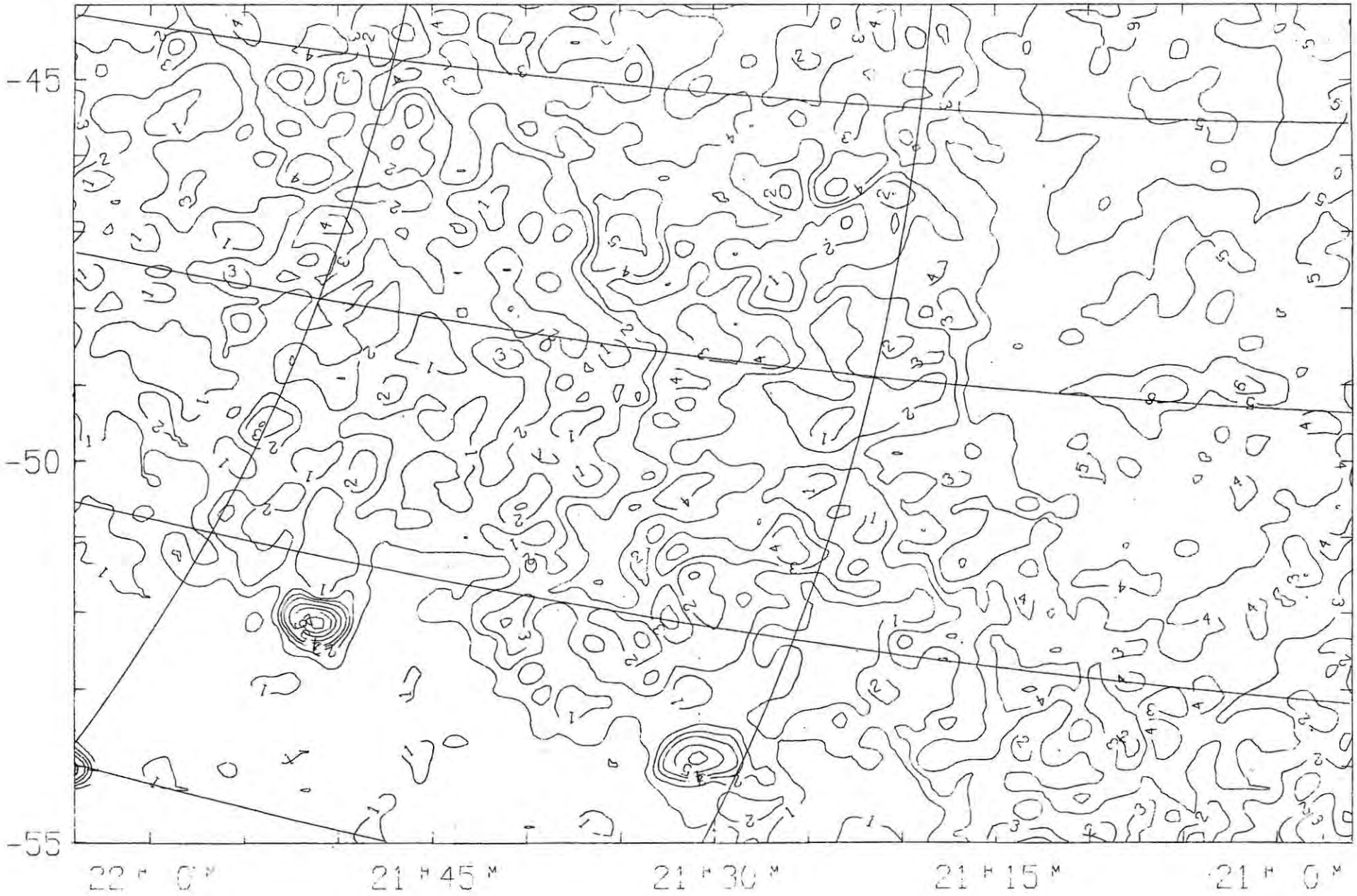
-45
-50
-55
22 H 0 M
21 H 45 M
21 H 30 M
21 H 15 M
21 H 0 M

13 H 00 M
12 H 45 M
12 H 30 M
12 H 15 M
12 H 00 M
-55
-60

14 H 0 M
13 H 45 M
13 H 30 M
13 H 15 M
13 H 0 M
-55-
-60-

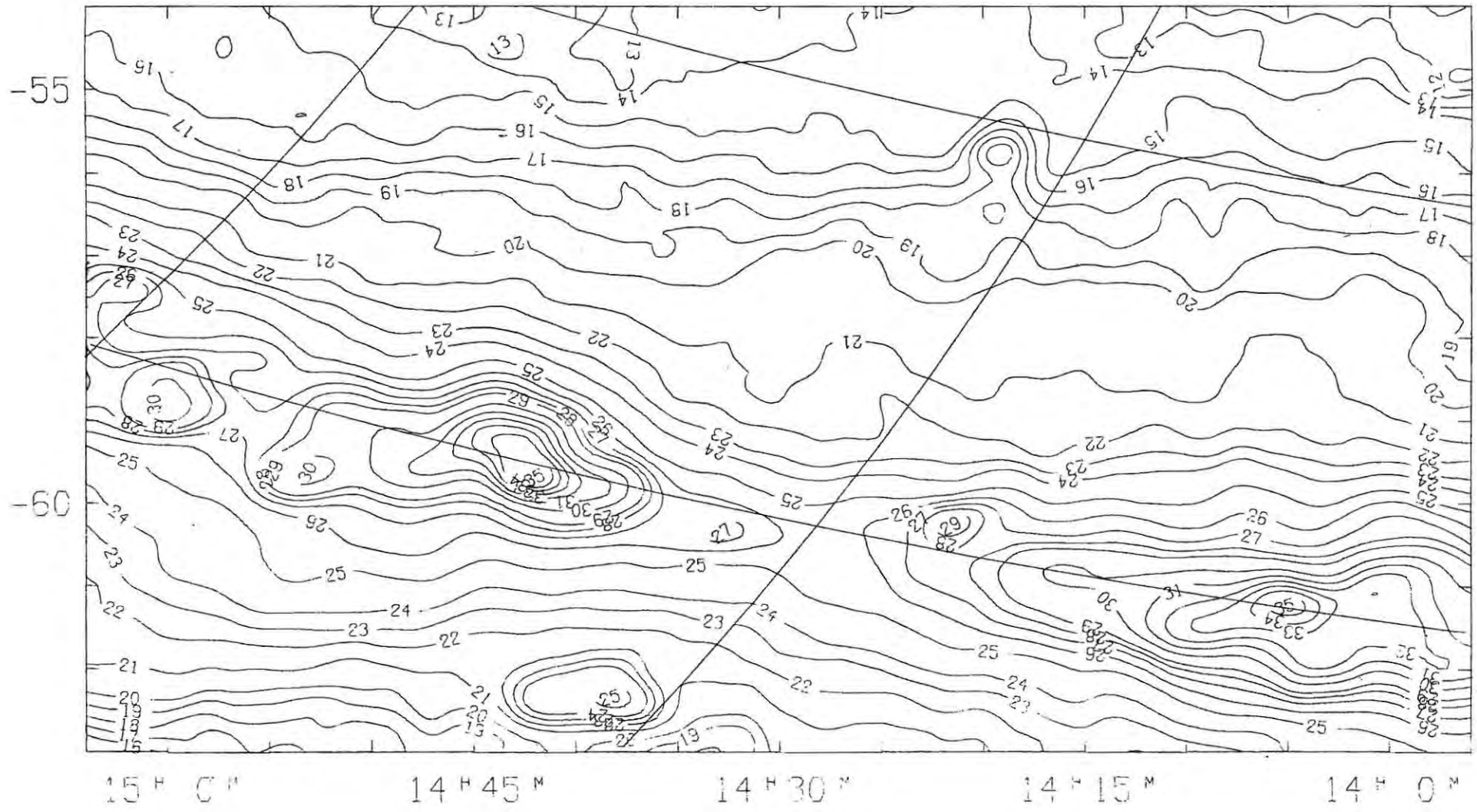
-55
-60
15 H 0 M
14 H 45 M
14 H 30 M
14 H 15 M
14 H 0 M

15 H 0 M
15 H 15 M
15 H 30 M
15 H 45 M
16 H 0 M
-55
-60

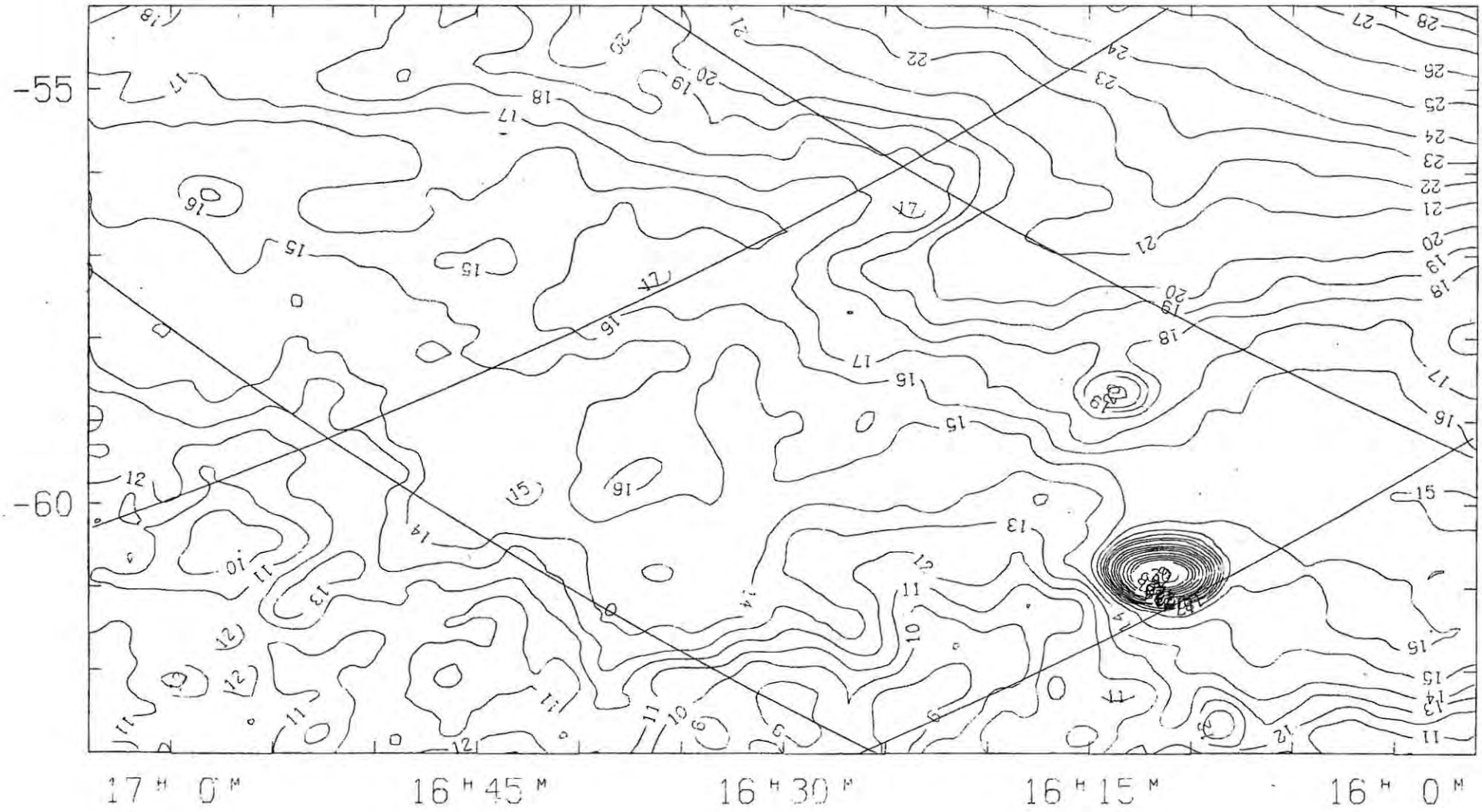
-55
-60
17 H 0 M
16 H 45 M
16 H 30 M
16 H 15 M
16 H 0 M

-55
-60
18H 0M
17H45M
17H30M
17H15M
17H 0M

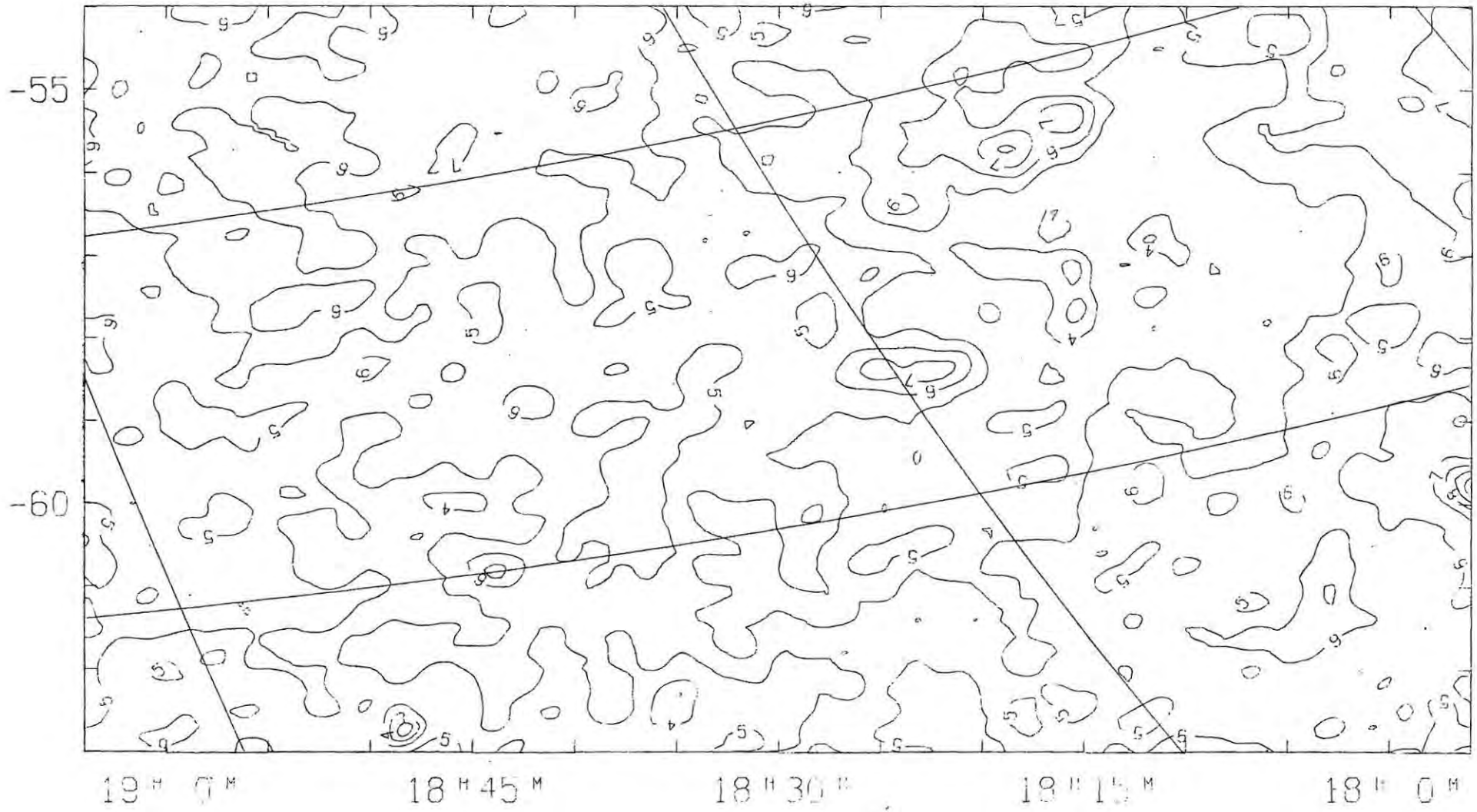
-55
-60
19 H 0 M
18 H 45 M
18 H 30 M
18 H 15 M
18 H 0 M

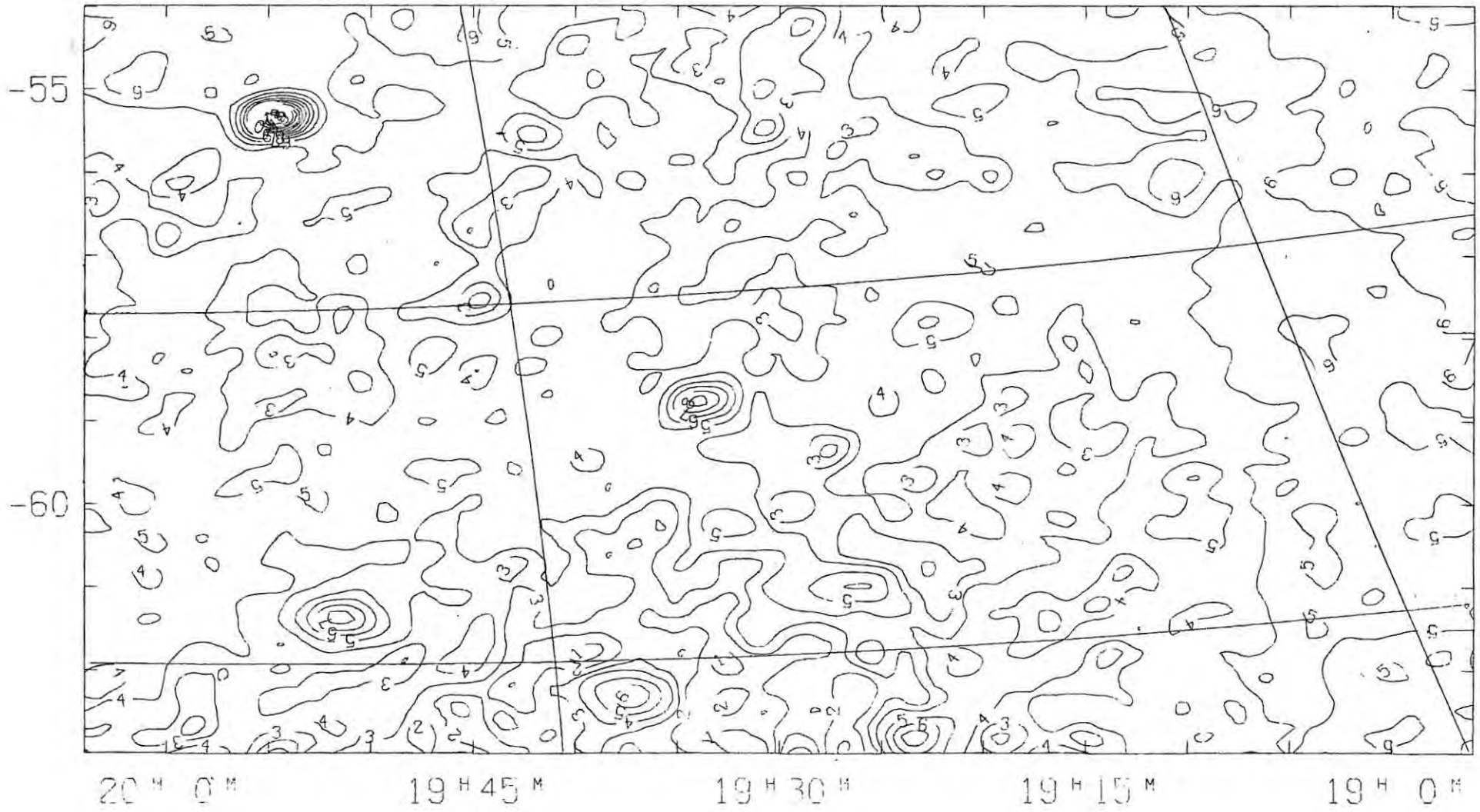
-55
-60
20 H 0 M
19 H 45 M
19 H 30 M
19 H 15 M
19 H 0 M

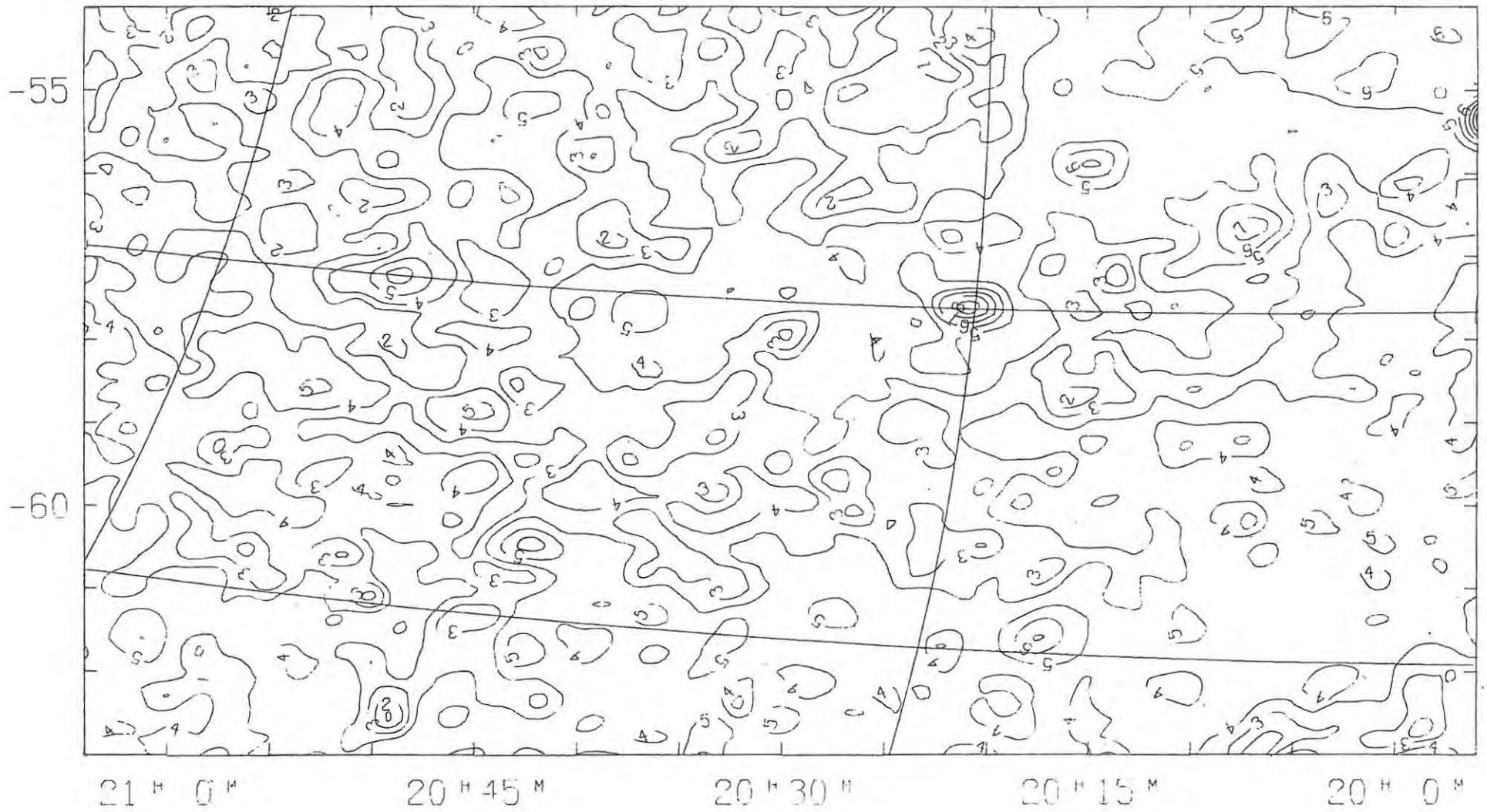
-55
-60
21 H 0 M
20 H 45 M
20 H 30 M
20 H 15 M
20 H 0 M